Keywords:
Oxalic acid
Heel removal
Chemical cleaning

Retention: Permanent

INVESTIGATING HYDROGEN GENERATION AND CORROSION IN THE TREATMENT TANK AND THE POTENTIAL FORMATION OF A FLOATING LAYER IN NEUTRALIZATION TANK DURING WASTE TANK HEEL CHEMICAL CLEANING

**D. T. Herman, B. J. Wiersma, F. F. Fondeur, J. C. Wittkop,
J. M. Pareizs, K. P. Crapse, M. S. Hay, M. R. Poirier, and S. D. Fink**

April 30, 2007

Chemical Science & Technology
Savannah River National Laboratory
Aiken, SC 29808

**Prepared for the U.S. Department of Energy Under
Contract Number DE-AC09-96SR18500**

SRNL
SAVANNAH RIVER NATIONAL LABORATORY

DISCLAIMER

This report was prepared as an account of work sponsored by an agency of the United States Government. Neither the United States Government nor any agency thereof, nor any of their employees, nor any of their contractors, subcontractors or their employees, makes any warranty, express or implied, or assumes any legal liability or responsibility for the accuracy, completeness, or any third party's use or the results of such use of any information, apparatus, product, or process disclosed, or represents that its use would not infringe privately owned rights. Reference herein to any specific commercial product, process, or service by trade name, trademark, manufacturer, or otherwise, does not necessarily constitute or imply its endorsement, recommendation, or favoring by the United States Government or any agency thereof or its contractors or subcontractors. The views and opinions of authors expressed herein do not necessarily state or reflect those of the United States Government or any agency thereof.

Printed in United States of America

This document was prepared in conjunction with work accomplished under Contract No. DE-AC09-96SR18500 with the U. S. Department of Energy.

TABLE OF CONTENTS

LIST OF FIGURES

LIST OF TABLES

ABSTRACT

The Savannah River Site (SRS) will remove sludge as part of waste tank closure operations. Typically the bulk sludge is removed by mixing it with "water" to create a slurry and transporting the slurry to a downstream tank for processing. Experience shows that a residual heel may remain that cannot be removed by this conventional technique. In the past, SRS used oxalic acid solutions to disperse or dissolve the sludge heel to complete the waste removal. To better understand the actual conditions of oxalic acid cleaning of carbon steel tanks, the authors developed and conducted an experimental program to determine its effectiveness in dissolving sludge, the hydrogen generation rate, the generation rate of other gases, the carbon steel corrosion rate, the impact of mixing on chemical cleaning, the impact of temperature, and the types of precipitates formed during the neutralization process.

The conclusions from the tests follow.

Corrosion

- Measured corrosion rates for the process demonstrations using simulated Tank 5F sludge depended primarily on temperature, agitation and orientation of the coupon.
- Testing used vertical coupons to simulate the primary tank wall. For tests with agitation of the solution, the maximum time-averaged corrosion rates measured 40 mpy, 30 mpy and 86 mpy for the 25, 50 and 75 °C tests, respectively. (Corrosion measurements by the methods used in this study have a typical uncertainty of 50%.) For tests without agitation, the maximum time-averaged corrosion rates decreased to 11 mpy, 0.76 mpy, and 36 mpy for the 25, 50 and 75 °C tests, respectively. The corrosion rate for the 50 °C non-agitated test appears inexplicably low. As a conservative estimate for this case a bounding value of 24 mpy was assumed by calculating the average of the corrosion rates at 25 °C and 75 °C.
- Testing used horizontal coupons to simulate the tank bottom and the maximum time-averaged corrosion rates on these coupons proved lower than for the tank walls (i.e., vertical coupons). For tests with agitation, the corrosion rates measured 0.5 mpy, 5 mpy and 15 mpy for the 25, 50 and 75 °C tests, respectively. For the tests without agitation, the corrosion rates were 0.87 mpy, 0.23 mpy, and 0.49 mpy for the 25, 50 and 75 °C test, respectively.
- The maximum time-averaged corrosion rates tests in the presence of radiation were 15 mpy, 60 mpy, and 12 mpy for the 25, 50 and 75 °C tests, respectively. Three differences between these corrosion rates and those measured in the process demonstrations are noteworthy. The sludge simulant for the 50 °C test differed from that used for the simulant demonstrations. Secondly, although the irradiated test container was aerated initially, we believe that the liquid became de-aerated with time, whereas ventilation settings in the process demonstrations (mimicking planned operating conditions) replenished the oxygen content of the liquid. Third, the tests with radiation continued for 15-20 days versus 10 days for the demonstrations. The longer time may have resulted in either higher or lower corrosion rates than observed during the process simulations.
- Visual examination of the coupons at the completion of the tests showed evidence of general corrosion and pitting on the immersed coupons. General corrosion, but no

appreciable pitting, occurred on the vapor space coupons without any evidence of acceleration due to oxalic acid in the vapor space.

- The following table shows the bounding corrosion rates during sludge dissolution recommended for application to structural analyses. The rates for the vertical coupons are considered as the most realistic and conservative.

	Corrosion Rate (mpy ±50%)	
Temperature (°C)	Mixed	Unmixed
25	40	11
50	30	24
75	86	36

- For the neutralization, or receipt, tank, initial corrosion rates following transfer of the spent acid reached as high as 90 mpy in the absence of agitation. Agitation of the contents of the receipt tank reduced the corrosion rates to less than 1 mpy.
- The corrosion product on the immersed coupons from the process demonstrations consisted primarily of humboldtine (α-$FeC_2O_4 \bullet 2H_2O$), sodium ferrous oxalate ($Na_2Fe(C_2O_4)_2$) and iron oxides such as goethite (α-FeO(OH)) and lepidocrocite (γ-FeO(OH)). The corrosion product on the vapor space coupon consisted primarily of goethite, lepidocrocite, and magnetite (Fe_3O_4). There was no evidence of oxalic acid attack on the vapor space coupon.
- Deposits on the coupons from the radiation tests consisted primarily of humboldtine. Sodium ferrous oxalate, the de-hydrated form of humboldtine, was not observed in these deposits. Thus, no substantial difference exists between the ferrous oxalate that formed in the dark environment of the radiation tests versus ferrous oxalate formed under the lighted environment of the process demonstrations. The lack of iron oxides on these coupons supports the contention of an oxygen-depleted liquid phase.

Hydrogen and Gas Generation

- Using actual and simulated sludge experiments mimicking planned processing conditions, the hydrogen concentration reached a maximum value of 0.017 vol %. During most of the experiments, the hydrogen concentrations remained close to or below the detection limit for the gas chromatographs (~5 ppm). The hydrogen concentrations observed in the process scaled demonstrations exceeded those measured in the experiments with actual tank samples.
- Based on the experimental results from the process demonstrations with simulated and actual waste, and scaling the hydrogen generation with metal surface area (8940 ft^2), the expected total hydrogen generation (for a single nominal 10-day cleaning cycle – experiments ranged from 9-14 days) in Tank 5F for the proposed cleaning process follows. The highest instantaneous generation rate from these experiments, projected to tank conditions, equates to 0.03 ft^3/min.

Temperature (°C)	Cumulative Hydrogen generation (ft^3 ±100%) Mixed	Unmixed
25	1.7	4.6
50	<1.6	8.9
75	<2.5	3.6

- In the process demonstrations and in the actual waste tests, the gas composition was dominated by carbon dioxide formed from the corrosion reactions. Tests also showed presence of nitrous oxide (as high as 3.3 vol %), about an order of magnitude less than the carbon dioxide. Analyses did not reveal the presence of any other flammable or combustible gases that pose process concerns.
- The projected total gas generation (for a single nominal 10-day cleaning cycle – experiments ranged form 9-14 days), based on the process demonstrations with simulated and actual waste, for the planned Tank 5F cleaning program is shown in the following table. We calculated these values based on oxalic acid usage and assumed 100,000 gallons in Tank 5F. The highest instantaneous total gas generation rate from these experiments, projected to tank conditions, equates to 655 ft^3/min.

Temperature (°C)	Cumulative Gas generation (ft^3 ±10%) Mixed	Unmixed
25	45,000	45,000
50	184,000	189,000
75	152,000	138,000

- At the conclusion of several of the process demonstrations, personnel increased the mixing speed in the dissolution tank to the equivalent of a Submersible Mixing Pump and monitored hydrogen evolution. No increase in hydrogen evolution occurred. Personnel also increased the speed of mixing in the actual waste tests upon completion of the dissolution period and decreased purge gas rate in an attempt to find evidence of trapped hydrogen. No increase in hydrogen concentration occurred.
- The irradiated tests generated markedly more hydrogen, but comparable total gas, at the higher temperatures (i.e., 50 °C and 75 °C) than observed in the other experiments. This behavior also occurred in the controls for those experiments, indicating radiation itself did not cause the elevated hydrogen. The irradiation test method included pulling vacuum on the sample containers and we believe this approach de-gassed the liquid removing oxygen. The absence of oxygen prevented formation of protective oxide solids observed in other experiments as confirmed by x-ray diffraction of coupons. Since the process demonstrations with simulant involved comparable mixing energies and ventilation conditions as the planned operations, the authors select these results as representative of planned operations.

Dissolution Efficiency, Mixing Behavior, and Process Findings

- The amount of sludge dissolved during a single acid cleaning cycle varied from a low of 60% based on iron measured in the supernate for the actual waste tests to a high of 99% based on uranium measured in the supernate during the simulant tests. These tests used sludge possibly more dispersed than is prototypical of the Tank 5F contents and hence the reported dissolution efficiencies may be biased high.
- The mass of residual solids in the dissolution vessel (e.g., Tank 5F) ranged between 31% and 51% of the starting sludge under the conditions tested. These solids are primarily oxalates and the amount formed tends to increase with temperature. Mixing did not strongly influence the amount of solids formed under the conditions studied.
- Solids in the dissolution vessel adhered to all the test surfaces: metal, glass and graphite. Not all of these solids could be suspended when the vessel was mixed with the energy equivalent to a Submersible Mixing Pump. Theses solids dispersed more easily in supernate than in either inhibited water or in a fresh oxalic acid solution.
- The mass of solids formed in the receipt tank (e.g., Tank 7F) ranged between 60% and 143% of the starting mass of sludge. These solids are a mix of sludge and oxalates. The amount of solids formed increased with increasing temperature.
- During transfer of the spent cleaning acid to an unmixed receipt tank (e.g., Tank 7F), the acid pooled to the upper surface of the liquid. Diffusion neutralized the layer in reasonably short time periods. Also, short periods of moderate energy mixing – approximating a small recirculation pump in Tank 7F – proved sufficient to blend the liquid layers.
- Researchers observed a floating precipitate layer in the receipt tank. This layer was easily dispersed and did not readily trap injected air. The layer settled and compacted reasonably quickly (i.e., almost all solids sank to the bottom by the end of the ~17 h transfer). Mixing energies equivalent to a Quad Volute pump fully suspended all the solids; mixing at energies equivalent to a standard slurry pump suspended the majority of the solids.
- Analysis of residual solids in the dissolution tank and of precipitated solids in the receipt tank showed evidence of minor amounts of separation of uranium from the poisons during the dissolution and re-precipitation process. The large majority of the precipitation uranium shows close proximity to neutron poisons.

Based on the completed work, SRNL recommends consideration of the following activities for process optimization. While regulatory commitments and budget restrictions may preclude consideration of this work for Tanks 5F and 6F, optimization should be considered for future chemical cleaning evolutions (e.g. Tank 4F).

- The data suggests high dissolution efficiency and the presence of excess acid at the end of the cleaning process. Consider additional beaker experiments with actual waste samples to examine the kinetics and efficiency of dissolution with lesser amounts of oxalic acid. Lesser acid use will reduce the amount of oxalate solids formed and simplify subsequent mechanical cleaning.

- Another optimization option is to reduce the concentration of the acid while maintaining the working volume (for mixing efficiency). Since the acid is near its solubility limit, this condition may have contributed to the large volume of solids formed.
- The scaled-demonstrations resulted in formation of oxalate compounds in the dissolution vessel (e.g., Tank 5F equivalent) that adhered to equipment and proved difficult to suspend. Screening experiments showed that use of supernate – rather than inhibited water or oxalic acid – proved reasonably effective in dispersing these solids. This finding supports the current process plan which includes a final mechanical cleaning evolution using supernate and vigorous agitation via a Submersible Mixing Pump. Greater process efficiency might result from alternating use of oxalic acid and mechanical sluicing as opposed to sequential acid cleaning cycles. Additional experimental studies may prove useful in selecting a preferred sequence for operations.
- Testing showed that the amount of oxygen, in combination with other factors, impacts the generation of hydrogen by shifting the reaction mechanism. While the demonstrations with simulated sludge mimicked the expected Tank 5F ventilation and mixing conditions, the scale of the experiment may not fully explore the mass transfer restrictions for oxygen. Additional exploratory studies to understand the role of oxygen may prove insightful.
- Analysis of the corrosion coupons from the actual waste demonstration could provide additional confirmation of the presence of protective oxide films during the planned cleaning process and confirmation of similar analyses from the demonstrations with simulated waste.

INTRODUCTION

The Savannah River Site (SRS) will remove sludge as part of waste tank closure operations. Typically the bulk sludge is removed by mixing it with "water" to create a slurry and transporting the slurry to a downstream tank for processing. Experience shows that a residual heel may remain that cannot be removed by this conventional technique. In the past, SRS used oxalic acid solutions to disperse or dissolve the sludge heel to complete the waste removal.[1,2,3] Since the waste tanks and cooling coils are constructed of carbon steel, a significant amount of corrosion may occur due to the acid. (Erosion is not expected to be a significant degradation mechanism even though pumps will be agitating the slurry.[4] Erosion of tank materials is dominated by the corrosion processes.) Although the total amount of corrosion may be insignificant for a short contact time, the corrosion reaction may generate a significant amount of hydrogen. One study indicates that with a 100 mpy (mils per year) corrosion rate,[4] the lower flammability limit (LFL) will be reached in less than seven days (assuming no forced ventilation available). If such conditions exist, the project will need to develop and deploy costly safety class equipment modifications and procedures for the ventilation system.

To better understand the actual conditions generated by oxalic acid cleaning of carbon steel tanks, the authors developed and conducted an experimental program. As a starting point for that program, they performed a literature review of the oxalic acid/carbon steel system.[5] The prior studies included coupon and electrochemical tests. The tests used a variety of environmental conditions (e.g., de-aerated with argon or in air, and with temperatures from 25 to 95 °C). The common denominator in most of the tests was use of oxalic acid alone (i.e, no components from the dissolved sludge) and use of polished coupons (i.e., no mill-scale or corrosion products present). Most of those prior corrosion studies measured coupon degradation over a specific test period (e.g., 3 days, 6 days, or 2 weeks). Thus, it is not possible to discern if the corrosion rate changes with time during the planned processing. Because of passivation reactions that occur during corrosion of carbon steel in oxalic acid, and the changing environment due to dissolution of the sludge and due to agitation, application of the earlier corrosion data for the entire evolution may overestimate the actual corrosion rate and hydrogen generation rate for this specific process. The review also suggested that cathodic reactions other than hydrogen evolution might occur during the corrosion process. Other potential cathodic reactions include oxygen reduction or the reduction of another anion, such as nitrate, in solution. If either the corrosion rate decreases with time or the other cathodic reactions predominate, the hydrogen generation rate will be less and significant upgrades in the ventilation system may not be necessary.

The Department of Energy (DOE) Hanford site performed sludge heel removal using oxalic acid in 2004**.** They (verbally) reported observing a floating layer during the neutralization step – i.e., the transfer of the spent acid into a caustic waste storage tank – that follows the oxalic acid sludge heel dissolution step. The presence of a floating layer may prevent the escape of gases that may form. Hence, prototypical experiments are needed to determine if a layer will form in the SRS process.

Closure Business Unit (CBU) personnel requested Savannah River National Laboratory (SRNL) to investigate the chemical cleaning process to determine its effectiveness in dissolving sludge, the hydrogen generation rate, the generation rate of other gases, the carbon steel corrosion rate, the impact of mixing on chemical cleaning, the impact of temperature, and the types of precipitates formed during neutralization of the spent acid.[6,7,8,9] SRNL conducted tests with simulated Tank 5F sludge, tests in which simulated Tank 5F sludge was irradiated, and tests with actual Tank 5F sludge.

TESTING

Feed Preparation

Oxalic Acid

Personnel prepared 8 wt % oxalic acid solutions in deionized water. Table 1 compares oxalate concentrations reported from the Ion Chromatography (IC) Anions method with the concentrations calculated from data obtained from the preparation sheets.

Table 1. Comparison of measured and targeted amounts of oxalic acid.

C_2O_4 measured (g)	C_2O_4 gravimetric (g)	% Difference (Analyzed vs. Recipe)
2143	2025	5.8
2018	2025	-0.4
783	810	-3.3

As shown, the maximum difference between the measured and target oxalate concentration is 5.8% which falls within the analytical uncertainty (of 10%). The remaining impurities had measured concentrations less than 100 ug/mL.

Supernate

To conduct the tests, personnel prepared supernate simulant, sludge simulant, and oxalic acid. Recipes and lot numbers from the chemicals used for these products can be found in the laboratory notebook.[10] The Deionized (DI) water came from a Barnstead Type D4700 NANOpure™ Analytical Deionization System. They prepared the supernate to match the currently available Tank 7F supernate data. (The supernate in Tank 7F will be used for mechanical cleaning, or sluicing, operations to remove sludge from Tank 5F prior to start of chemical cleaning.) Table 2 shows the supernate composition. They vacuum filtered the resulting mixture with a 0.45-µm nylon membrane Nalgene® filter, aged it for two days, and verified the absence of solids before using. They analyzed the supernate simulant for the major constituents (i.e., anions by IC, metals by Inductively Coupled Plasma – Emissions Spectroscopy (ICP-ES), free hydroxide by titration and carbonate by total inorganic carbon/total organic) prior to use.

Table 2. Simulated supernate recipe.

Component	Source	Molarity
NaOH	NaOH	1.0870
$NaNO_3$	$NaNO_3$	0.6300
$NaNO_2$	$NaNO_2$	0.6084
$NaAlO_2$	$Al(NO_3)_3.9H_2O$	0.203
Na_2SO_4	Na_2SO_4	0.098
Na_2CO_3	$Na_2CO_3.H_2O$	0.4396
NaCl	NaCl	0.0163
NaF	NaF	0.0209
Na_2HPO_4	$Na_2HPO_4.7H_2O$	0.0065
$Na_2C_2O_4$	$Na_2C_2O_4$	0.0052
Na_2SiO_3	$Na_2SiO_3.9H_2O$	0.00261
Na_2MoO_4	$Na_2MoO_4.2H_2O$	0.000131
KNO_3	KNO_3	0.01500
CsCl	CsCl	0.00014

The Tank 7F supernate simulant was prepared as three 10-L and three 15-L lots and subsequently combined into three 25-L batches. (The analyses of the three lots agreed within 3% for the four major components.) Tables 3-5 provide a comparison of measured and targeted compositions. Formate and bromide fell below detectable concentrations. Silicon, fluoride and oxalate each fell below target and outside analytical uncertainties. However, these are not prominent contributors to the current studies and we accepted these variances.

Table 3. Average elemental concentration for Tank 7F supernate simulant.

Component	Target Concentration (mg/L)	Gravimetric Concentration (mg/L)	ICP-ES (mg/L)	% Target vs ICP-ES
Al	5467	5467	4770	-13
K	586	586	529	-10
Mo	13	13	11	-9
P	202	202	179	-12
S	3144	3144	2920	-7
Si	73	73	47	-35
Na	88823	88822	75350	-15

Table 4. Average anion concentrations for Tank 7F supernate simulant.

Component	Target Conc. (ug/mL)	Gravimetric Concentration (ug/mL)	IC ANIONS (ug/mL)	% Diff Target vs IC Anions
Fl	397	397	238	-40
Cl	408	408	480	18
NO_2	27987	27987	28767	3
NO_3	39061	39061	36900	-6
PO_4	627	627	< 100	NA
SO_4	9418	9418	9373	0
C_2O_4	701	701	386	-45

Table 5. Average hydroxide and carbonate concentrations for Tank 7F supernate simulant.

Component	Target Concentration (Mol/L)	Gravimetric Concentration (Mol/L)	Reported Concentration (Mol/L)	% Diff Target vs ICP-ES
Free OH	1.02	1.09	1.06	4
CO_3	0.44	0.44	0.41	-8

Simulated Sludge

They prepared a depleted uranium PUREX sludge simulant with composition shown in Table 6. The sludge simulant was analyzed for the major metal constituents by Inductively Coupled Plasma - Emissions Spectroscopy (ICP-ES) prior to use.

Table 6. Simulated Tank 5F sludge target composition (based on equilibrium calculations and Waste Characterization System values).

Component	wt %	Component	wt %
$Al(OH)_3$	11.30	$Ni(OH)_2$	10.02
$BaSO_4$	0.52	$Pr(OH)_3$	0.15
$CaCO_3$	2.36	$SrCO_3$	0.06
CaF_2	0.14	$UO_2(OH)_2$	17.31
$Ca_3(PO_4)_2$		Ag_2CO_3	0.21
$Cr(OH)_3$		$Ba_3(PO_4)_2$	
$Fe(OH)_3$	44.50	$Ca(OH)_2$	1.37
HgO	0.15	$CePO_4{\cdot}2H_2O$	0.19
$KMnO_4$		$Pu(OH)_4$	0.02
$La(OH)_3$	0.15	$Sr_5(PO_4)_3OH$	0.12
$Mg(OH)_2$	0.37	$ZnCr_2O_4$	0.59
$Mn(OH)_2$	10.01	ZrO_2	0.49

The depleted uranium (DU) sludge simulant was analyzed by ICP-ES. Experiments used a radioactive sludge containing DU as well as a non-radioactive sludge of the same approximate

formulation that omitted the uranium. Table 7 compare measured concentrations to the elemental concentrations derived from the values previously listed in Table 6 As apparent in the tables, the simulant sludge prepared for the tests is a reasonable approximation to the target Tank 5F Sludge composition although the aluminum concentration has a notable deviation from the target, likely from loss of soluble aluminum during washing. The lower aluminum content (4-5 wt %) better reflects the analysis (1.44 wt %) for the as-received samples from the tank. Some trace elements (e.g., Ce and Cr) did not agree with target concentrations but these are not prominent species for the purposes of the current study. Numerous minor species also feel below analytical detection limit. However, since these do not play major roles in the chemistry, we elected to not perform additional analyses.

Table 7. Comparison of measured and targeted sludge elemental composition.

NonRadioactive Simulant Sludge

Element	Calc Conc (ug/g)	ICP-ES (ug/g)			% Diff Calc vs ICP-ES
Al	47265	22300	±	2230	-53
Ba	3699	2760	±	276	-25
Ca	16007	16200	±	1620	1
Cr	3178	2510	±	351	-21
Fe	281182	231000	±	23100	-18
Hg	1679	ND		NA	NA
K	NA	< 3290	±	NA	NA
La	1332	1460	±	146	10
Mg	1865	1580	±	158	-15
Mn	74750	56700	±	5670	-24
Ni	76696	75200	±	7520	-2
Pr	1331	ND		NA	NA
Sr	1067	< 1500	±	NA	NA
U	NA	NA		NA	NA
Ag	1986	1880	±	252	-5
Ce	1187	2600	±	788	-119
Pu	189	ND		NA	NA
Zn	1998	ND		NA	NA
Zr	4385	3310	±	334	-25
P	992	< 1300	±	NA	NA
F	681	ND		NA	NA
S	714	1690	±	327.86	137

DU Simulant Sludge

Element	Calc Conc (ug/g)	ICP-ES (ug/g)			% Diff Calc vs ICP-ES
Al	39098	21700	±	2170	-44
Ba	3060	3150	±	315	3
Ca	16007	18200	±	1820	14
Cr	2629	817	±	114	-69
Fe	232593	207000	±	20700	-11
Hg	1389	ND		NA	NA
K	NA	6620	±	662	NA
La	1102	1360	±	136	23
Mg	1542	1360	±	136	-12
Mn	61833	58900	±	5890	-5
Ni	63443	59000	±	5900	-7
Pr	1101	ND		NA	NA
Sr	1067	4410	±	441	NA
U	135523	132000	±	13200	-3
Ag	1643	789	±	79	-52
Ce	982	3530	±	353	259
Pu	156	ND		NA	NA
Zn	1653	ND		NA	NA
Zr	3627	34000	±	3400	837
P	992	ND		NA	NA
F	681	ND		NA	NA
S	714	254	±	104	-64

For schedule expediency, personnel substituted an available non-radioactive sludge based on Tank 8F chemistry for the 50 °C experiment that investigated the influence of radiation. Details of that material preparation are provided in another report.[11] Table 8 shows that recipe.

Table 8. Tank 8F simulated sludge used in 50 °C radiation tests

Cations	wt %, dry		Anions	wt %, dry
Aluminum, Al	9.59		Carbonate, CO_3^{2-}	5.13
Calcium, Ca	2.11		Nitrite, NO_2^-	5.87
Copper, Cu	0.13		Nitrate, NO_3^-	1.95
Iron, Fe	24.34		Total Hydroxide, OH^-	24.7
Potassium, K	0.005		Oxide, O^{2-}	11.4
Magnesium, Mg	0.12		Phosphate, PO_4^{3-}	0.13
Manganese, Mn	2.73		Sulfate, SO_4^{2-}	0.64
Sodium, Na	7.20			
Nickel, Ni	2.79			
Silicon, Si	0.76		**Specific Gravity**	1.1
Strontium, Sr	0.09			
Zinc, Zn	0.27		**Total Solids, wt %**	16.0

Tank 5F Sludge and Tank 7H Supernate
For the actual waste experiments, personnel used a sample of solids collected from Tank 5F and a sample of supernate from Tank 7F. Characterization of these samples is the subject of a separate report.[12]

Simulated Sludge Chemical Cleaning Demonstrations

Table 9 shows the conditions for the tests conducted. The values for the Dissolution Vessel temperature mimic the three options under consideration for Tank 5F operations by the project. The receipt tank for the residual acid (i.e., Tank 7F) will not be heated and hence the experiment controlled this temperature to near ambient. The inlet oxalic acid temperature was controlled to match the Dissolution Vessel temperature except in the highest temperature cases. In those experiments, the acid was maintained at 50 °C to minimize localized cooling when entering the vessel but to also avoid excessive evaporation over the 6 or 7 day duration[a] of the transfer.

Table 9. Test matrix for process demonstrations with simulated waste.

Test	Dissolution Vessel Temperature (°C)	Oxalic Acid Temperature (°C)	Receipt Vessel Temperature (°C)	Mixing
1	50	50	25	Yes
2	75	50	25	Yes
3	25	25	25	Yes
4	50	25	25	No
5	75	25	25	No
6	25	25	25	No

[a] Personnel altered the duration of transfer slightly to minimize overtime labor costs on weekends while maintaining a value within typical durations for planned project evolutions.

Personnel conducted the simulated sludge chemical cleaning demonstrations as follows. They placed 7656 mL of 8 wt % oxalic acid in a glass vessel. They placed polypropylene beads on top of the oxalic acid and covered the vessel to minimize evaporation. They placed 190 g of simulated sludge containing depleted uranium into a ~ 22 L glass vessel. They added 775.6 g of simulated salt solution. The ratio of acid to sludge and the ratio of supernate to sludge mimic the values expected in Tank 5F for the cleaning operations. The absolute amounts were selected based on the dimensions of the glass vessel and the corrosion coupon rack used.

They then purged the vessel with air containing a helium tracer. The flow rates of helium (0.117 cm^3/min) and of air (17 cm^3/min) were controlled by MKS mass flow controllers (model numbers 1179A23541 and 1179A01312CS1BV, respectively). The six demonstrations have an average vapor space turnover time of 853 min. The flow rates selected provided a comparable vapor space turnover rate for the current Tank 5F ventilation system. Design Authority personnel indicated minimum allowable ventilation flow rates for tanks are controlled between 45 scfm (minimum) and 72 scfm (minimum) for safety requirements, depending on tank contents. These values provide a turnover time of 1920 min and 1198 min, respectively, for the tank vapor space. The nominal flow rate for Tank 5F is 150 scfm with a maximum capacity of 300 to 400 cfm anticipated at 75 °C. The nominal flowrate provides a turnover time of 575 min for the tank vapor space. Thus, the volumetric turnover in the experiments was slightly lower than the nominal value and within the safety requirements for the tank (see Table 15). A slower turnover rate will increase the peak hydrogen concentration. Hence, the experiments are slightly conservative for peak hydrogen concentration relative to nominal operating conditions.

They heated the oxalic acid and sludge to the target temperatures. Once the oxalic acid and sludge reached the target temperatures, they transferred the oxalic acid to the sludge tank at ~ 0.7 mL/min. (The oxalic acid was maintained at either 25 °C – in the case of the tests dissolution at 25 °C – or at 50 °C to emulate pre-heating of the acid before addition to Tank 5F.) This rate was selected so the acid transfer occurred over approximately 7 days, similar to planned duration of oxalic acid transfer for Tank 5F processing.

Initially, the sludge tank mixer remained inactive to mimic the lack of mixing in Tank 5F during the first acid additions until a sufficient liquid level is established to prime the pumps. In tests with mixing, the mixer was turned on after the liquid reached the agitator impeller. This point typically occurred after ~2 days, similar to the timing that may occur in full-scale operation. The mixing conditions – i.e., impeller dimensions and rotational speed – were selected from Table 10 to provide comparable mixing energy as expected in Tank 5F operations with a circulating pump.

Once the oxalic acid addition finished, the contact with sludge continued for ~50 hours. After the 50 hour contact, researchers pumped the vessel contents to a receipt tank that contained 5 Liters of simulated salt solution. Personnel transferred 1.5 L from the Dissolution Vessel to the Receipt Vessel with the exception of Test 1 and Test 5 in which 3 L was transferred. The reduction in transfer volume for the remaining tests allowed personnel to perform post-dissolution mixing in the Dissolution Vessel to look for any evidence of trapped hydrogen on the solid residues and to assess ability to suspend those residues.

The transfer occurred over ~17.5 hours. This transfer rate approximated the upper range of the transfer rates possible for Tank 5F to Tank 7F transfers with existing equipment. The higher rate is believed more likely to cause massive precipitation and hence the greatest potential to form a floating layer in the receipt tank that might impede gas release. Transfer occurred through a submerged tube into the receipt tank – analogous to the Tank 7F downcomer – with no agitation in the tank. These conditions mimic planned operations in Tank 7F and use of the maximum flowrate provides a greater potential for solids formation. Personnel measured the pH for the receipt tank contents during the transfer.

Table 10. Equivalent mixing energies for experiments and for Tanks 5F and 7F.

Agitation in Tank 5F 105,000 gallons sludge and oxalic acid	**Equivalent Rotation Speed in Dissolution Vessel 7 L slurry 4 inch pitched-blade impellor**
Telescoping Transfer Pump: 300 gpm with 2 inch discharge nozzle 0.11 hp per 1000 gal	64 rpm
Standard Slurry Pump: 600 gpm with 1.5 inch discharge nozzle 0.27 hp per 1000 gal	182 rpm
Quad Volute Slurry Pump: 2600 gpm with 3.63 inch discharge nozzle 0.64 hp per 1000 gal	243 rpm
Submersible Mixing Pump: 3800 gpm with 4.4 inch discharge nozzle 0.92 hp per 1000 gal	274 rpm

The temperature of the acid-sludge slurry was monitored during the tests. The pH was measured daily with a pH probe or paper. (Early tests used an in situ probe for continuous monitoring but the slow variance in values observed led to a decision to omit the probe in later tests as a simplification of the equipment and a cost savings.) The pre and post dissolution sludge as well as the spent OA solution were analyzed for metals by ICP-ES and ICP-MS (Inductively-Coupled Plasma - Emission or Mass Spectroscopy). The test sampled a portion of the off-gas stream using an online Agilent Model M300A Micro-GC gas chromatograph (GC) with a Molsieve 5A column for measurement of helium, hydrogen, oxygen, and nitrogen. Personnel added a PoraPlot Q column for measurement of carbon dioxide and nitrous oxide after Test 3. Argon was the carrier gas for the GC. Researchers used a gas standard of known composition to calibrate the peak areas prior to each test and to check the calibrations following each test.

Personnel photographed or videotaped selected portions of the experiments.

Sampling

Filtrate Samples

Liquid filtrate samples for Test 1 were obtained from the Dissolution Vessel at 2 h, 25 h, and 50 h during the soaking period following end of addition of the oxalic acid (OA). Samples for Test 2 included the same soak period samples plus additional samples taken at various times during the addition of OA to the Dissolution Vessel. For Tests 3-6, a daily sampling frequency for 10 days was implemented for starting at the end of the first day of OA addition.

Filtrate samples were obtained by the use of a 30 mL syringe connected to a stainless steel downcomer via Viton® tubing. Samples were pulled from the liquid located directly above the settled solids for unmixed conditions. For mixed conditions, the agitator motor was stopped and the sample pulled from the approximate midpoint of the liquid level. Once taken, the samples were tested for pH, filtered through 0.45 micron syringe filters and prepared for elemental analysis by ICP-ES as well as determination of uranium by ICP-MS. The pH of the samples ranged from 14 before acid addition to less than 1 (in the Dissolution Vessel) at the end of the experiment. Plots of the analytical results for the filtrate samples are contained in the APPENDIX.

Solids Samples

Solids samples were obtained to aid in determining the amount of sludge that dissolved, the chemical composition of solids formed in the receipt vessel, and the nature of solids that precipitated or formed (from corrosion) in the Dissolution Vessel. After emptying the Dissolution and Receipt Vessels, the remaining contents of these vessels were filtered in 0.45 micron filter cups under vacuum, removed from the filters, and allowed to air dry. Once the filter cake was dried (by vacuum filtration at ambient temperature), the solids were weighed and sampled for analysis. Figure 1 shows typical samples from each vessel.

Figure 1. Samples of solid residues from 25 °C, unstirred experiment.

The solid samples were digested by the aqua regia method prior to analysis by ICP-ES and ICP-MS. Additionally, samples were submitted for X-ray Diffraction (XRD), Scanning Electron Microscope (SEM), and Energy Dispersion X-ray analysis (EDX) to help determine the

chemical compounds and crystalline nature. Each of the tests started with 190 g of dry DU sludge. Table 11 shows final dried weights for solids from the Dissolution and Receipt Vessels at the end of each test.

Recall that Tests 1 and 5 included transfer of 3 L of acid solution to the Receipt Vessel whereas the other tests only transferred 1.5 L. Hence, the larger amount of solids in Receipt Vessel results in part due to the greater amount of digested sludge available for precipitation. In contrast, the amount of solids in the Dissolution Vessel is a combination of undigested sludge and precipitates –primarily oxalates – from the corrosion of the coupons. Higher temperature favors sludge digestion – which would decrease residue mass – but also accelerates corrosion thereby increasing residue mass. The data shows such a trend. Note that in the absence of mixing, the total residue weight in Dissolution Vessel increases. Review of the data in conjunction with corrosion measurements and chemical analyses (in later sections of the report) shows the trend of increasing residue mass chiefly reflects the increase in corrosion rather than a decrease in sludge digestion from lack of mixing.

Table 11. Final dried solids weights for process demonstrations.

			Percentage of Initial Sludge	
	Mixed (g)	**Unmixed (g)**	**Mixed**	**Unmixed**
Dissolution Vessel Solids				
25 °C	61.7	65.8	32.5%	34.6%
50 °C	59.4	77.1	31.3%	40.6%
75 °C	97.4	74.4	51.3%	39.2%
Receipt Tank Solids				
25 °C	113.4	139.7	59.7%	73.5%
50 °C	272.5	159.4	143.4%	83.9%
75 °C	220.5	237.6	116.1%	125.1%
Total Solids Formed				
25 °C	175.1	205.5	92.2%	108.2%
50 °C	331.9	236.5	174.7%	124.5%
75 °C	317.9	312	167.3%	164.2%

Corrosion Coupon Preparation

The corrosion coupons used for these tests were procured from Metals Samples Co., Munford, AL, and conform to the ASTM A537 Class I carbon steel (A537) specification. Table 12 shows the composition of this particular heat of steel. Type I waste tanks, such as Tank 5F, are fabricated from ASTM A285 Grade B carbon steel (A285). However, the A537 carbon steel is an adequate substitute because previous testing demonstrated that both steels have similar corrosion behavior and rates when exposed to oxalic acid solutions.[13]

Table 12. Material test report for Heat J973 manufactured by Bethlehem Steel.

Material is ASTM A537 Class I carbon steel. The compositions shown are in wt %.

Al	C	Cr	Cu	Mn	Mo	Ni	P	S	Si	Fe
0.066	0.18	0.16	0.157	1.31	0.055	0.18	0.018	0.01	0.279	balance

The dimensions of each coupon were measured with digital calipers to the nearest 0.025 mm (or 0.001 inches). Typical dimensions for coupons used for the sludge dissolution and neutralization tests are 5 cm x 2 cm x 0.33 cm. The exception is the largest coupon (15 cm x 2 cm x 0.33 cm) that simulated the tank bottom during the sludge dissolution tests. Typical dimensions for coupons used for the hydrogen generation tests in presence of radiation are 2.23 cm x 1.27 cm x 0.33 cm. The coupons were weighed on an analytical balance to the nearest 0.0001 grams. Nominal initial weights for coupons for the sludge dissolution and neutralization tests ranged from 32 grams to 190 grams for the small and large coupons, respectively. The nominal initial weight for the coupons utilized for the (irradiated) hydrogen generation tests was 6 to 7 grams.

The initial surface condition of the coupons was a 600 grit polished finish (see Figure 2). The polished coupons provide a uniform, reproducible surface finish ideal for studying reactions between the steel and the environment. Previous laboratory studies on the corrosion of carbon steel in oxalic acid have primarily utilized polished coupons. However, the metal surface conditions inside the tank are very different. Steel plates from the foundry, similar to those used to build the waste tanks, typically have an adherent iron oxide film on the surface referred to as mill scale. The presence of this film would be expected to produce a different corrosion response than the polished surface, at least initially.

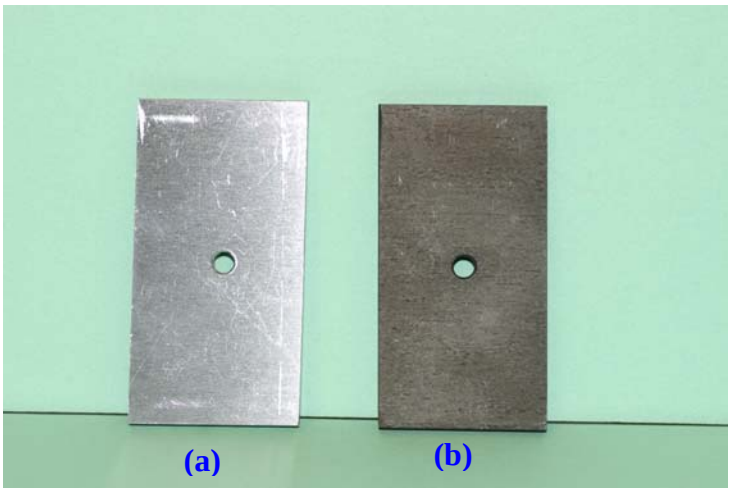

Figure 2. Typical coupons for process demonstrations.

Shown are: a) polished coupon and b) mill scale coupon.

To simulate the mill scale in these tests, coupons were placed in a Thermolyne™ benchtop muffle furnace set at 700 °C for 20 minutes. The result was a uniform oxide identified by x-ray diffraction as primarily magnetite (see Figure 2). Also, the tank steel has been exposed to caustic supernate for many years. To simulate this exposure, we immersed each coupon in simulated supernate for a minimum of 24 hours and then dried. This step left the coupon

encrusted with a salt layer similar to the condition of the tank walls. Polished and mill scale coupons were employed for the sludge dissolution and neutralization tests, while only mill scale coupons were used for the hydrogen generation tests.

In-situ Monitoring of Corrosion Coupons

Equipment and Assembly

To perform the corrosion measurements within each test vessel, an electrochemical cell was designed. The cell consisted of four primary features: a) a working electrode, b) a counter electrode, c) a reference electrode, and d) a potentiostat. Each feature is briefly described below.

The working, or corroding, electrode is the carbon steel coupon being tested. The coupons were prepared for testing by attaching a 22 AWG wire to one end of a coupon with silver epoxy. The coupon was then mounted in a chemically resistant acrylic compound to protect the exposed end of wire and the silver epoxy during the test and to provide an easily held sample (see Figure 2). (To verify the chemical inert nature of the acrylic, personnel exposed samples to oxalic acid at 75 °C for a period of 7 days and noted negligible swelling, weight gain, or attack.)

Multiple working electrodes were placed in each test vessel. Glass sample holders were designed to hold the coupons at specific locations and orientations. A single glass sample holder held the large coupon or "plate" (see Figure 3b). This coupon was located at the bottom of the vessel such that the face was oriented parallel to the bottom of the vessel and the bottom side elevated by the glass holder to allow liquid contact on all edges. The small coupons were positioned in a "tree-like" holder with the face oriented approximately perpendicular to the bottom of the vessel (see Figure 3a and Figure 4). Four to five small coupons were located at different heights in each vessel. For purposes of this report, the coupon holder positions are numbered 1 through 5 beginning with the lowest coupon. The wires from the coupons were extended through the top of the vessel via a glass tube, where they were then attached to the potentiostat.

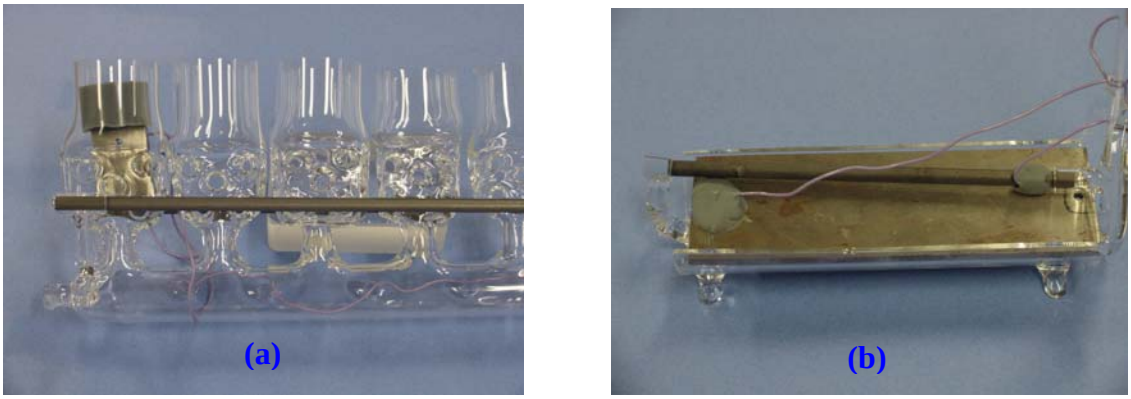

Figure 3. a) Small coupon in tree-like glass holder and b) plate coupon in glass holder. The cylindrical rod is the carbon graphite counter electrode.

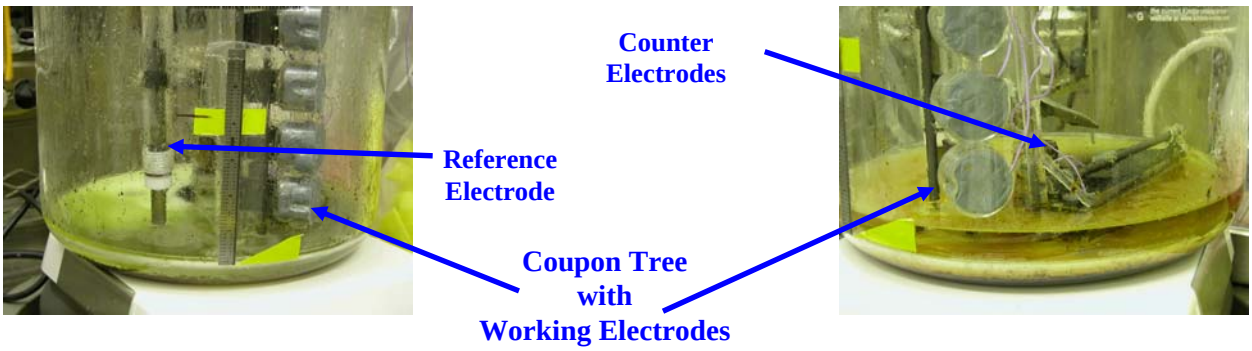

Figure 4. Photograph showing the relative location of the electrodes in the vessel.

The counter electrode provides a path for an impressed current to flow through the solution from the working electrode. Materials that are conductive, yet chemically inert, are suitable for counter electrodes. In these tests carbon graphite rods served as the counter electrodes. Again, researchers attached a 22 AWG wire to one end of the rod with silver epoxy and covered with the acrylic mounting material. The rods were positioned to allow for a uniform current density to flow from the working electrodes (see Figure 3 and Figure 4). Two rods were oriented vertically in the vessel such that the row of small coupons held by the tree-like holder was flanked on each side by a counter electrode. A single rod was oriented horizontally above the large coupon at the bottom of the vessel. The wires from the counter electrodes extended through the top of the vessel via the glass tube for connection to the potentiostat.

The reference electrode measures the electrochemical potential of a metal surface in a given environment. When a stable reference electrode is employed any changes in the potential can be related to changes in the metal surface of the working electrode. These tests used an ORION™ saturated silver/silver chloride (SSC) electrode. This electrode has shown excellent stability and reproducibility in previous high temperature testing with similar chemical systems. The reference electrode was held by a separate glass tube holder and fully immersed in the solution near the tree-like holder, away from the large sample (see Figure 3). Typically it is desired to reduce the effect of the solution resistance on the measured potential by locating the reference electrode as close as possible to the working electrode. However, in this case the solution was very conductive and the extended distance did not significantly impact the measured potential.

The potentiostat consists of a power supply that supplies the impressed current on the electrochemical cell and circuitry that measures and controls the potential to selected values. The tests used two potentiostats: 1) a PAR™ Model 273A Potentiostat/Galvanostat, and 2) a Gamry™ PCI4/750 Potentiostat/Galvanostat/Zero Resistance Ammeter. The Gamry™ ECM8 Electrochemical Multiplexer was also employed with the Gamry™ potentiostat so that multiple working electrodes could be monitored simultaneously. The data acquisition software used for the PAR™ potentiostat was CorrWare™ for Windows, while the Gamry™ instrument used company developed software.

Test Techniques

The two electrochemical techniques performed during the sludge dissolution and neutralization tests were Corrosion Potential (E_{corr}) monitoring and Linear Polarization Resistance (LPR).[14,15] Personnel monitored the corrosion potential of each working electrode to observe changes in the oxidizing or reducing conditions at specific locations in the vessel. Observing these changes assists in the determining the corrosion mechanism and whether or not hydrogen generation is thermodynamically possible.

The LPR technique provides a quick, non-destructive, in situ estimate of the uniform or general corrosion rate. The technique is based on the observation that when the potential at the metal surface is polarized anodically or cathodically within 20 mV of E_{corr}, the measured current density at the metal surface increases linearly with potential. The slope of this line is defined as the polarization resistance (R_p). Stern and Geary[16] modified the fundamental equation for electrochemical reaction kinetics, and demonstrated that the relationship between the corrosion current density (i_{corr}) and R_p at E_{corr} is:

$$i_{corr} = \frac{b_a b_c}{2.3(b_a + b_c)R_p} \qquad \text{equation 1}$$

where b_a and b_c are the anodic and cathodic Tafel slopes, respectively. The Tafel slope is determined experimentally. When an electrode is polarized from E_{corr}, it frequently will yield a current/potential relationship over a region that can be approximated by

$$\eta = \pm B \log (i/i_o) \qquad \text{equation 2}$$

where η is the difference between the measured potential and E_{corr}, i is the current density, and B and i_o are constants. When B is positive it is b_a, the anodic Tafel slope, while negative B values are the cathodic Tafel slopes, b_c. If the Tafel slopes are unknown, frequently the assumed value for b_a and b_c is 120 mV/decade.[17] Unless the actual slopes are quite different than 120 mV, the error in the value of i_{corr} is not significant. Both software packages for the potentiostats utilized the 120 mV assumption to calculate i_{corr}. This assumption was confirmed in another series of supporting tests for this program.[18] The corrosion current is related to the corrosion rate (CR) by the following equation:

$$CR = 0.13 * \frac{i_{corr} E_w}{\rho} \qquad \text{equation 3}$$

where E_w is the equivalent weight of iron (27.9 g/equivalent), and ρ is the density of iron (7.86 g/cm^3). The corrosion rate is reported in mils (0.001 inches) per year.

The potential scan rate is a critical variable for the LPR technique.[19] A test performed at too high of a scan rate causes a high capacitive current that results in hysteresis in the plot of the potential and the current. As a result the polarization resistance may be under-estimated and the corrosion rate, which is inversely proportional to the polarization resistance, may be over-estimated. On the other hand faster scan rates are desirable since the time at which the specimen is polarized from its equilibrium potential is minimized. A scan rate of 0.1 mV/s was selected

initially for these tests. Figure 5 shows a typical example of an LPR curve taken during tests in the sludge vessel. The small amount of hysteresis shown during these tests substantiated the selection of this scan rate.

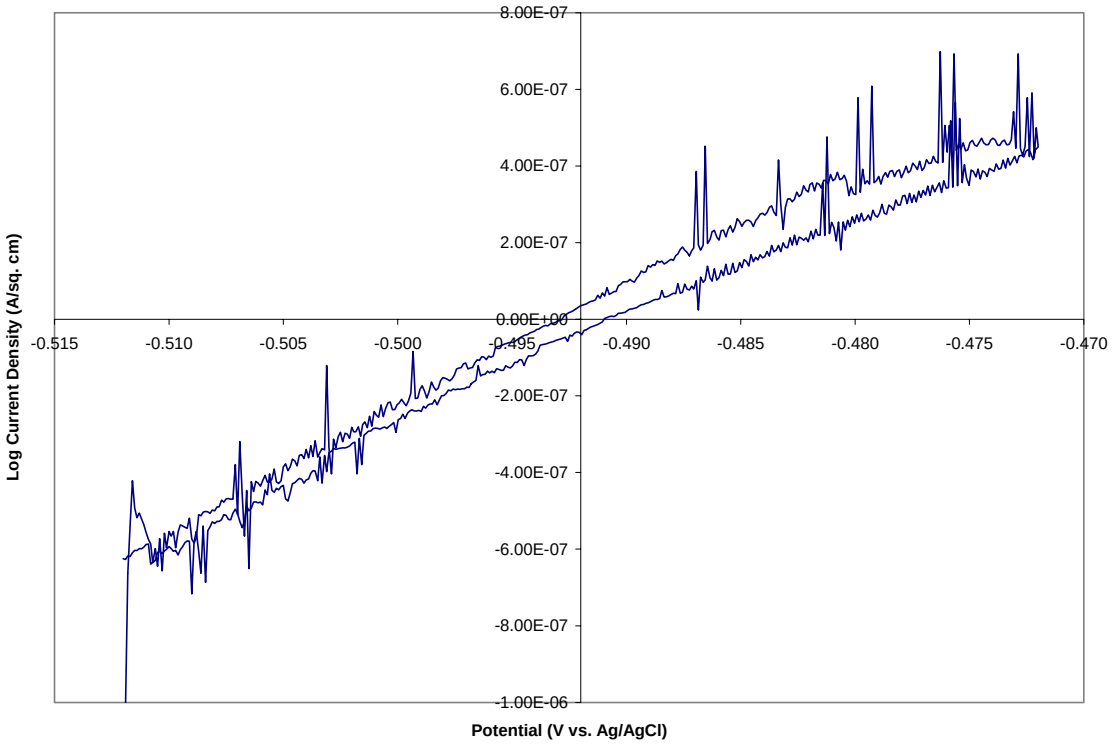

Figure 5. Example of Linear Polarization Resistance curve measured during tests.

Combined Impact of Corrosion and Radiation on Hydrogen Generation Rate

These experiments measured the hydrogen generation rate due to corrosion of the carbon steel in an oxalic acid chemical cleaning solution mimicking Tank 5F conditions. Previous testing focused on polished and pre-corroded specimen coupons in a de-aerated oxalic acid environment.[20] Researchers added sludge and supernate to the oxalic acid and mill scale samples (pre-treated with supernate). The experiments occurred in a radiation environment to simulate the effects of radiation on the hydrogen generation rate. Table 13 shows the test variables and matrix. The experimental design included replicates at each condition with and without radiation.

Table 13. Test matrix for hydrogen generation tests in radiation field.

Test	Temperature (°C)	Sludge	Gamma Radiation	Test Duration (hours)
1	50	Simulated Tank 8F (no U)	Yes	405
2	50	Simulated Tank 8F (no U)	No	405
3	75	Simulated Tank 5F (no U)	Yes	330
4	75	Simulated Tank 5F (no U)	No	330
5	25	Simulated Tank 5F (no U)	Yes	476
6	25	Simulated Tank 5F (no U)	No	476

Equipment and Assembly

The coupon and test solution were situated inside a 45-mL stainless steel container (PARR™ Series 4700 Screw Cap Bomb) as shown in Figure 6. Each test occurred in a glass insert within the container to prevent the possibility of galvanic corrosion between the coupon and the container. The containers were placed inside an aluminum block heated by band heaters (see Figure 6). Type K thermocouples monitored container temperature and provided feedback to a temperature controller. The pressure in each container was measured with a Rosemount™ Model 1151DP pressure transducer. The transducers were calibrated with a range of 0 to 150 inches of water (0 to 5.4 psig). Approximately 8 to 10 feet of 1/8" stainless steel tubing connected the container to the sampling manifold.

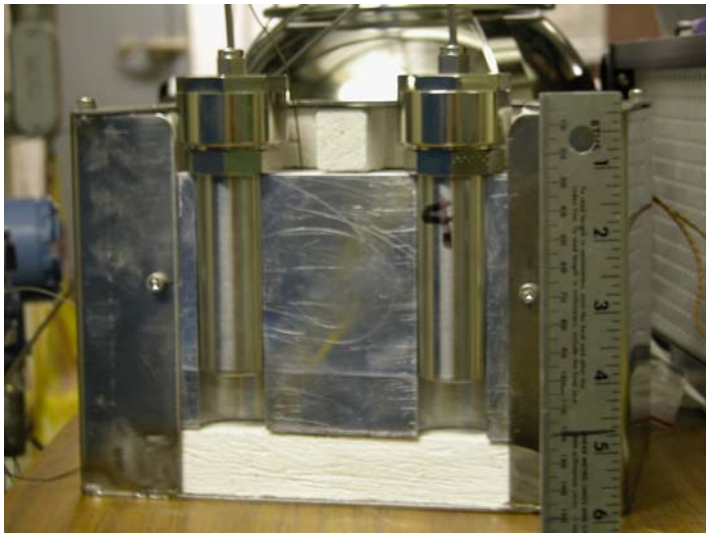

Figure 6. Stainless steel containers for radiation tests situated in aluminum heater block.

A photograph of the actual manifold is shown in Figure 7, while a schematic drawing of the system is shown in Figure 8. The sample manifold consisted of 1/8" and 1/16" stainless steel tubing. Sampling of the containers via the manifold was automated with a control system developed utilizing LabVIEW™ 7.1 (National Instruments). The control system actuated the solenoid valves (ASCO™ Series 8380) on the manifold.

Gas samples from each container were obtained in the following manner (see Figure 8 for valve identification). The pressure in the chambers was recorded by the software, so that the quantity of gas being produced was determined as a function of time. At a user selected frequency (typically 4 hours), or whenever the pressure in the chambers reached the maximum that can be measured by the instrumentation, a gas sample from one of the containers was collected by opening the automated solenoid valves (e.g., S1a and S1b) thus allowing the gas from a container to enter the main body of the manifold. The manifold was then pressurized with argon gas to a pressure of 5 psig by opening valve AR. Shortly after the manifold was pressurized, the valves between the manifold to the gas chromatograph (e.g., GCa and GCb) were opened. Simultaneously with the opening of these valves, the LabVIEW™ controller delivered a signal to the gas chromatograph that a sample was ready. Once the sample had been sent, these valves were closed isolating the manifold. The remaining gases in the manifold were purged from the system by an air operated vacuum eductor. After the sample line was purged, the gases in the sample container were purged and air from the atmosphere was re-introduced into the container via valves Aa and Ab. This cycle was then repeated for the remaining containers.

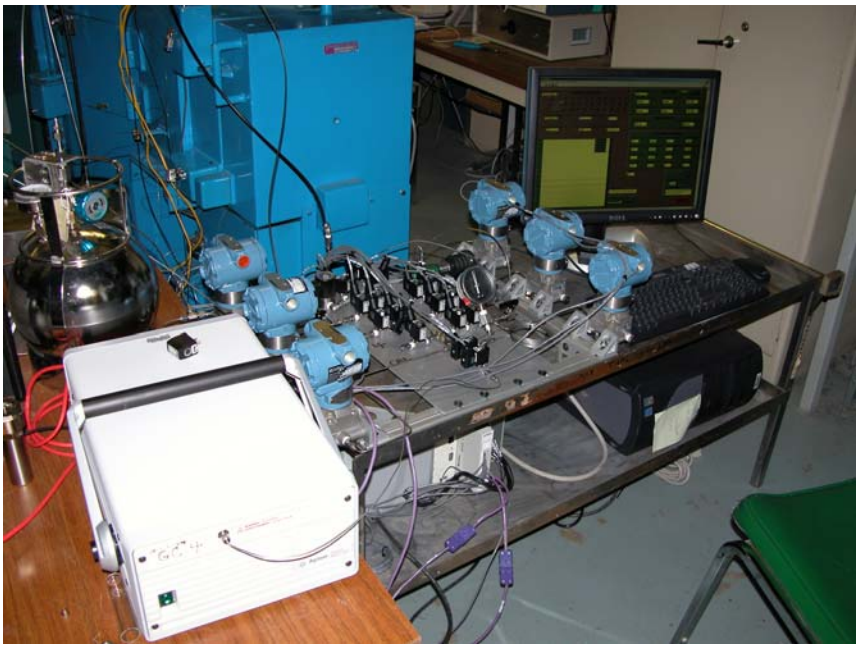

Figure 7. Photograph of the gas collection manifold.

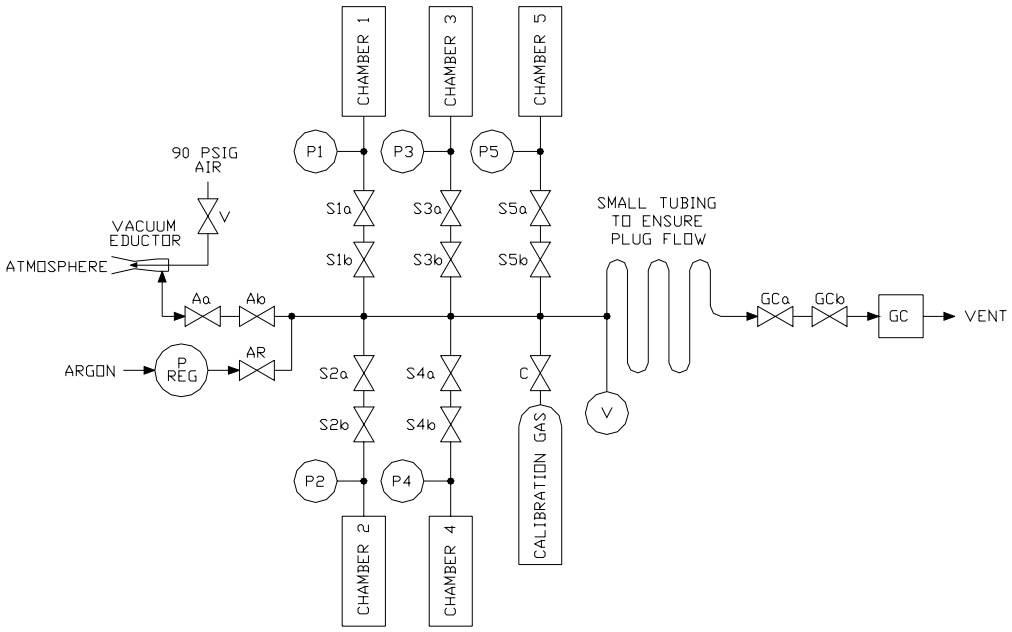

Figure 8. Schematic drawing of gas collection manifold.

Experiments occurred simultaneously in four test containers at a given test temperature. One of the aluminum blocks held two of the containers inside a radiation field. The radiation cell for these tests was a J.L. Sheperd Model 484™ (see Figure 9). The dose rate was set to 25,000 rad/hour to mimic the calculated dose rate from the remaining sludge in Tank 5F.[21]

Figure 9. J. L. Sheperd Model 484™ Radiation Source.

Testing used two gas chromatographs (GC) for gas sample analysis. The primary GC for these tests was an Agilent 3000A Micro GC™ equipped with two columns to measure nitrogen, oxygen, hydrogen and carbon dioxide, with a MTI Model M200 Micro GC™ used as a back-up system. The latter model was capable of measuring only nitrogen, oxygen, and hydrogen. Personnel used a third GC to analyze several samples obtained manually. This GC was also an MTI Model M200, with the additional capability of analyzing for carbon dioxide and other components. The Agilent GC used the Cerity™ software, also developed by Agilent, to analyze the data, while the MTI Model M200 GCs used an older version of the EZChrom™ software developed by Agilent.

Post-test analyses and characterization

At the completion of the test, researchers removed the coupons from the test container for visual examination. During this examination, the form of corrosion on each coupon was identified (e.g., general) and differences in the corrosion products were noted. Photographs were taken to document the results. ASTM standard practices were followed to determine the general corrosion rate.[22] The corrosion products were removed from the sample by a two step process. First, loose corrosion products were removed using a wire brush. The coupons were then immersed in Clarke's solution (i.e., an inhibited HCl acid solution) to remove the final corrosion products. After removal of the corrosion products, the coupons were then weighed to determine the weight loss during the test. The corrosion rate (CR, in units of mpy) is related to the weight loss by the following equation:

$$CR = \frac{3.45 \times 10^6}{A \times T \times \rho} w \qquad \text{equation 4}$$

where w is the weight loss in grams, A is the area of the coupon in cm^2, T is the exposure time in hours, and ρ is the density of the coupon in g/cm^3.

Solids collected at the bottom of the glass insert during the test. These solids were visually similar to those deposited on the metal sample. A few grams of these solids were collected and submitted for x-ray diffraction analysis for identification. The remaining liquid in the test container was also submitted for post-test characterization. A final pH of the solution was determined, typically with litmus paper. Ion chromatography (IC) was performed to identify the concentrations of anions, while ICP-ES was performed to identify the concentrations of the elements in the solution. These final analyses were conducted only on solutions that had been exposed to the gamma source.

Actual Waste Tests

Portions of the sludge from Tank 5 F were contacted with oxalic acid to simulate tank cleaning operations. The actual waste tests – see Table 14 – occurred at 50 ºC and 75 ºC via remote handling in the SRNL Shielded Cells (SC). A separate report provides full chemical characterization and other information on the sludge sample.[12]

To allow for visual observation, reactors were constructed of glass (Figure 10). A carbon steel coupon was placed in contact with the solution for the duration of each test. Hydrogen, and other gases, released during the oxalic acid contact were measured by an on-line gas chromatograph for comparison to the results from the simulant tests.

Each test used a reactor fitted with a thermocouple, glass holder with carbon steel coupon, and stir bar prior to placement in the SRNL shielded cells. Additionally, the reactor was fitted with a reflux condenser in the shielded cells. Water at ambient temperature (25 ºC) circulated through the cooling coils of the reflux condenser. All of the fittings connected to the reactor and reflux condenser were either Teflon® or ground glass fitted with a Teflon® sleeve.

To check for gas leaks prior to each test, researchers purged the test reactor with air (50 cm^3/min) containing helium (0.25 or 0.125 cm^3/min) as a tracer. By measuring the exiting concentration and compared to the measured inlet mass flows, one could determine if He leaked from the equipment (since the lighter gas would diffuse faster through any minor leaks or air influx would register as a dilution of He concentration). The purge gas was introduced directly into the reactor and exited passing through the top of the reflux condenser. Prior to GC analysis, the purge gas passed through a cold finger inserted into an aluminum block cooled to below 4 ºC using a Model IC10 Electronic Ice Cube (Torrey Pines Scientific) to remove additional moisture. A portion of the off-gas stream was sampled using an Agilent Model M200 Micro-GC with a Molsieve 5A column for measurement of helium, hydrogen, oxygen, and nitrogen and a PoraPlot Q column for measurement of carbon dioxide and nitrous oxide. Argon was the carrier gas for the GC. Researchers used a gas standard of known composition to calibrate the peak areas prior to each test and to check the calibrations following each test.

Given that low flow rates for the addition of the oxalic acid were prohibitive with the available equipment, oxalic acid addition occurred in batch fashion. (Batch addition is expected to maximize generation of hydrogen by allowing maximum corrosion.) The two tests used an 8 wt % oxalic acid (OA) to sludge/supernate volume ratio of 20:1. For each test a 7 mL portion of sludge/supernate mixture (composed of a 1:1 volume ratio of Tank 5F sludge sample FTF-05-06-55 and Tank 7F supernate sample FTF-07-06-19) was added to the test reactor through the purge inlet (without purging). A portion of 8 wt % OA was used to rinse the residual sludge/supernate mixture from the container into the reactor before addition of the remainder of the 145 mL of OA solution to the test reactor.

The reactor was then heated using a heating mantle. The solution temperature was monitored throughout testing. Visual inspection of the reactor was periodically recorded using a video camera. The oxalic acid dissolution tests were monitored for hydrogen generation via gas chromatography. Adjustments to the purge gas flow were made during the experiments as necessary, primarily to increase sensitivity for hydrogen detection.

At the completion of the tests the reactor was cooled and the oxalic acid solution filtered through a 0.45 micron filter prior to analysis of the filtrate and residues. A portion of the oxalic acid solution (30 mL) from each test was neutralized via submerged addition to a Tank 7F simulant (50 mL). Solids formation and liquid layer behavior were observed and recorded by video camera during both rapid (via syringe over several minutes; 50 ºC test) and slower addition (via

peristaltic pump requiring more than one hour; 75 ºC test) of the acid solution to the caustic Tank 7F simulant.

In the 50 °C test, personnel added the oxalic acid filtrate to the simulated supernate over the course of a few minutes. This high rate of addition immediately caused the entire solution to become cloudy with precipitated solids throughout the reactor. During this rapid addition, only one liquid layer, with pH 14, resulted after the addition of the solution. In an attempt to make conditions more closely mimic planned operations, the 75 °C neutralization test used a specially modified peristaltic pump to add the oxalic acid filtrate at a slow rate that minimized mixing in the reactor. Two distinct liquid layers occurred during this addition as well as the formation of solids, similar to the behavior observed in the process demonstrations with simulated waste. Some solids remained suspended in the liquid layers and collected near the interface of the two liquid layers as well as on the submersed stainless steel tubing used for adding the OA solution. The pH of the top layer measured 3 roughly corresponding to the starting OA filtrate. The pH of the lower layer measured 14 corresponding to the supernate solution. Five minutes after slowly swirling the reactor, the top layer remained pH 3. After continued gentle mixing to combine the liquid layers (i.e., complete the acid-base neutralization), solids remained suspended in the liquid. After standing 25 minutes, a liquid sample from near the top measured pH 8 and suspended solids persisted. After 50 minutes, suspended solids continued to persist, and the pH remained 8. Technicians used a stir-bar for further agitation with the resultant well-mixed solution measuring pH 14. Personnel recorded both the slow (50 °C test) and rapid (75 °C test) actual Tank 5F waste OA filtrate neutralizations by video tape.

Table 14. Matrix for actual waste tests.

Test	Dissolution Temperature (°C)	Oxalic Acid Temperature (°C)	Neutralization Temperature (°C)	Mixing
1	50	Ambient	Ambient	Yes
2	75	Ambient	Ambient	Yes

Relative Scale of Tests to Process

Table 15 shows a comparison of the headspace turnover time, sludge volume to carbon steel surface area ratio, oxalic acid volume to carbon steel surface area ratio, and oxalic acid volume to sludge volume ratio for the tests and for planned operations in Tank 5F. Tank 5F contains mounds of “moist” solids. During start of an acid cleaning cycle, the tank will also contain a supernate heel. The amount of heel (i.e. supernate) present may vary slightly between cycles. For these process demonstrations with simulated sludge, researchers selected a supernate-to-sludge volume ratio of ~4 based on discussions with Design Authority personnel.

Figure 10. Equipment for actual Tank 5F waste chemical cleaning test.

In the process demonstrations, researchers added oxalic acid to provide a 20:1 volume ratio with the sludge solids plus an incremental amount to neutralize the supernate (i.e., approximately one volume of acid to one volume of supernate). In the other two sets of experiments, researchers added oxalic acid at a 20:1 volume ratio based on the combined volume of sludge and supernate. This variance in approaches resulted in the addition of more acid per gram of sludge in the actual waste and radiation tests as shown in Table 15.

Table 15. Geometrical and process conditions in chemical cleaning tests and in Tank 5F.

Test	Head space volume per purge rate (min)	Sludge* (gal) per ft^2 metal surface area	Oxalic acid (gal) per ft^2 metal surface area	Oxalic acid volume per sludge plus supernate volume	Oxalic acid volume per sludge volume
Irradiation Test	N/A	0.005 – 0.006	0.5 - 0.6	15 - 26	90, 100[@]
Actual Waste Test	22.5 – 34.7	0.1	4.2	20.7	42 (dry) 21 (wet)
Simulant Demonstrations (50 °C, mixing)	473	0.25 (dry) 0.50 (wet)	8.8	10.1	35 (dry) 17.5[#] (wet)
Simulant Demonstrations (others)	908	0.25 (dry) 0.50 (wet)	8.8	10.1	35 (dry) 17.5[#] (wet)
Tank 5F Nominal	853 (1728 for safety limit of 45 scfm)	0.56 (dry) 1.34 (wet)	11.8	8.8	20

* Sludge values are calculated on a "dry" bases accounting only for the sludge mounds (in Tank 5F) or the dry sludge added (in experiments) and on a wet based accounting for the added supernate.

[#] These values assume the starting sludge holds 50 wt % water.

[@] For 50 °C experiment.

RESULTS

Simulated Sludge Chemical Cleaning Demonstrations

Figure 11 below shows the experimental setup for the tank heel chemical cleaning testing using simulated sludge with depleted uranium. The first three tests occurred under identical conditions with the exception of the Dissolution Vessel temperatures which were set at 50 °C, 75 °C and 25 °C for Tests 1, 2 and 3, respectively. These first three tests included mixing when the vessel liquid height reached the agitator. The second set of tests, Tests 4, 5 and 6, operated at the same temperatures (50 °C, 75 °C and 25 °C, respectively) but with no mixing of the Dissolution Vessel.

Figure 12 illustrates the progression of the test over time. Each of the tests followed a similar pattern with differences in the timing primarily due to different temperatures. There was very little visual difference between the mixing and non-mixing tests other than the formation of large crystals being preferred slightly in the unmixed tests. Visual inspection of the lower temperature experiments (i.e., Tests 3 and 6) seemed to promote larger crystal growth. It should be noted that mixing did not start for any of the tests until at least 45 hours after the start of acid addition. At this time, sufficient acid had been added to reduce the pH to <2 and the vessel contents had turned green in color.

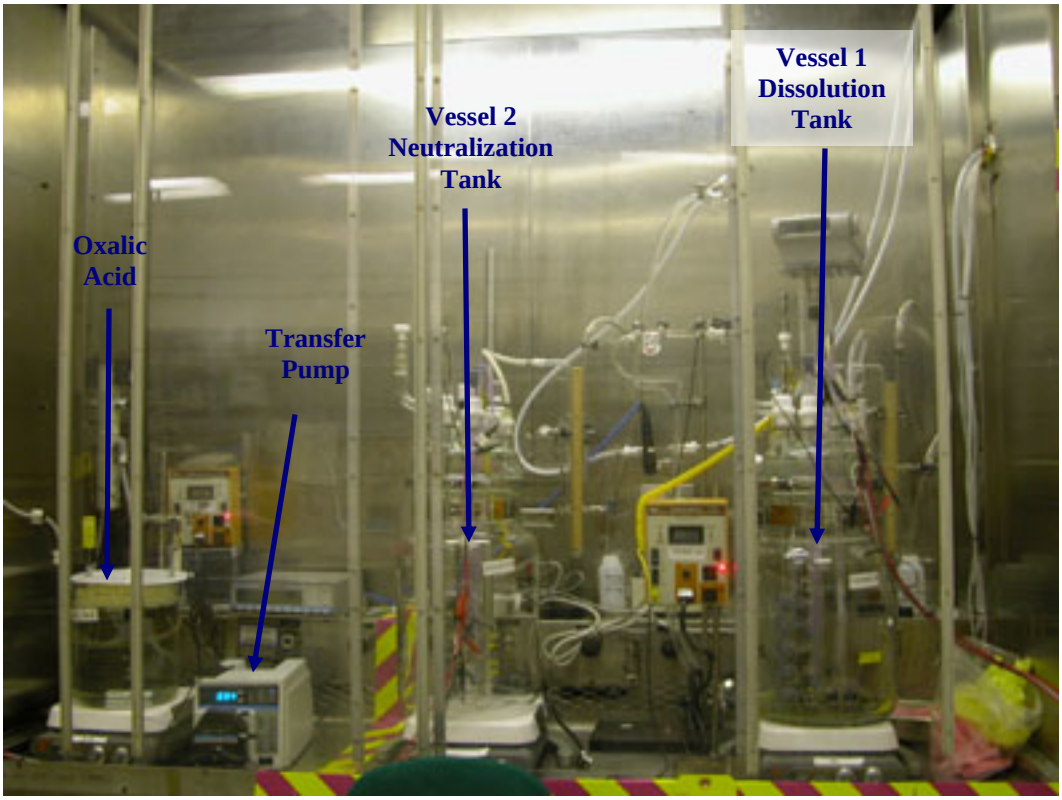

Figure 11. Equipment for chemical cleaning (experimental) demonstrations.

The oxalic acid addition led to the formation of white colored solids directly under the acid addition point. As more acid was added, the solids took on a bright yellow color. It should be noted that the liquid level had not reach any of the metal coupons when the yellow colored material first formed. As acid addition continued, the formation of solids spread throughout the vessel. A white colored layer soon was visible across the top of the un-dissolved sludge. The solids then took on a brown or rust color. The brown coloring typically resided on top of the white solids formed. As more acid was added and the pH continued to drop the solution became an emerald green color characteristic of iron oxalate (or trisoxalatoiron(III) complex, $Fe(C_2O_4)_3^{3-}$). As acid addition continued the solution became darker moving to an olive green color. Acid addition stopped after approximately 7656 mL of oxalic acid had been added for each test. The vessels were then allowed to stand for 50 hours to allow the acid to continue dissolving the sludge. In Tests 1-3, mixing persisted during the 50 hour period while the vessel remained unstirred for Tests 4-6.

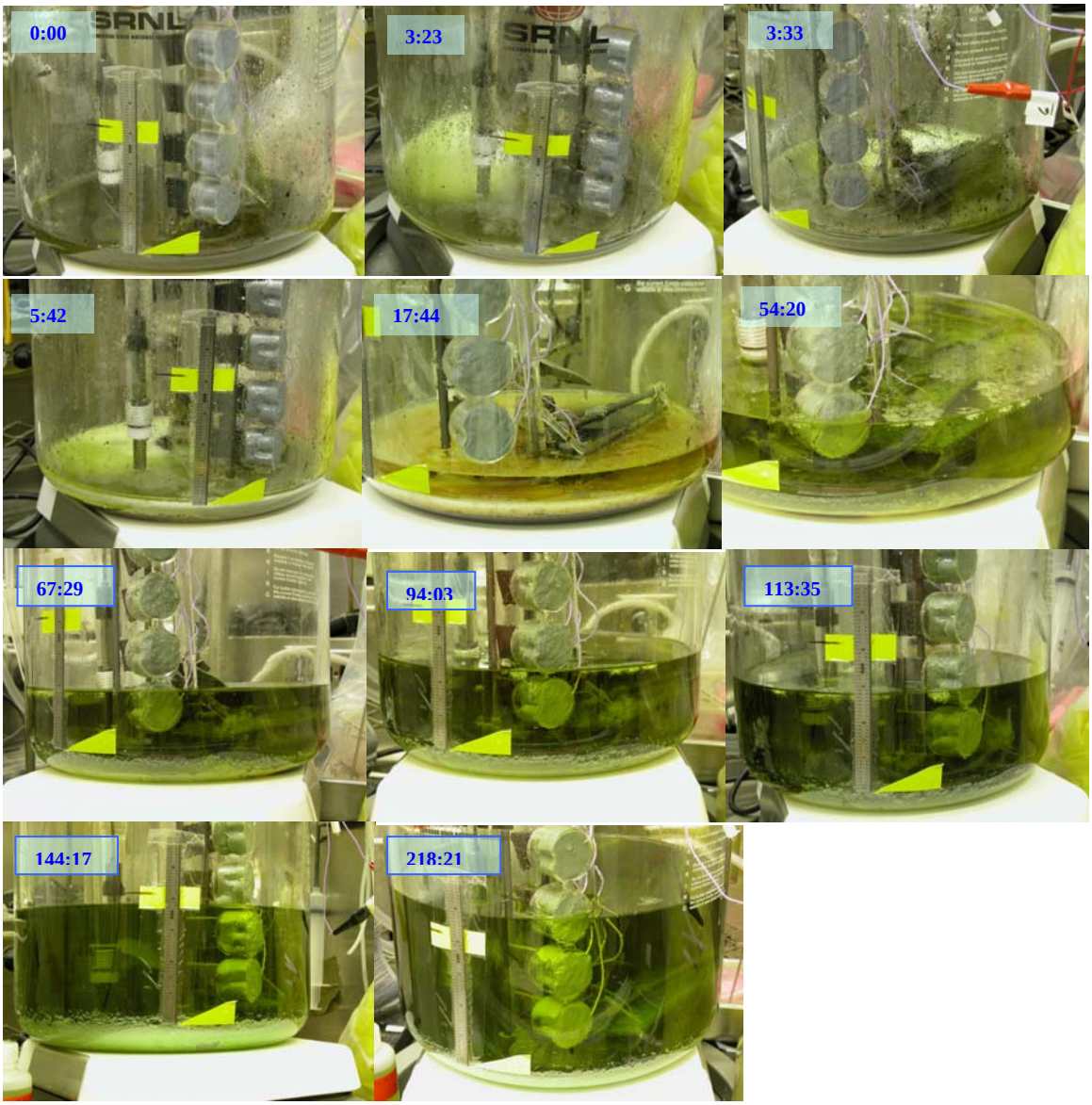

Figure 12. Stages of dissolution in Test 6 (25 °C, unmixed) from start of acid addition. The highlighted block shows the time (in hours:minutes) since start of the experiment.

The next sequence of pictures (Figures 13-16, 18-29, and 21) shows the individual test vessels at similar time intervals after the start of acid addition. In a given series, photos are not available for selected tanks at a given time and are not included. Additionally, the acid addition for Tests 1 and 5, at ~140 hours, was shorter that for the other tests (~170 hours). The pictures are displayed with Tests 1 thorough 3 (mixing tests) on the top row and Tests 4 though 6 (non-mixing tests) on the lower row. A blank space is left if a picture is not available for a particular test at that time. The Test 2 acid addition rate at the beginning of the test was determined to be less that the other tests due to a problem with the acid delivery pump. The total amount of acid added was consistent with the other tests; however, it was added at an accelerated rate at the end

of the test. The amount added in the final "batch" roughly scales to the equivalent of a single tanker addition into Tank 5F.

Figure 13 shows the Dissolution Vessel for individual tests approximately 20 hours after the start of acid addition. The effect of the different temperatures can be seen in the difference in the coloration of the bulk liquid. Also note that the liquid level is below the agitator so there was no mixing in any tests at this time.

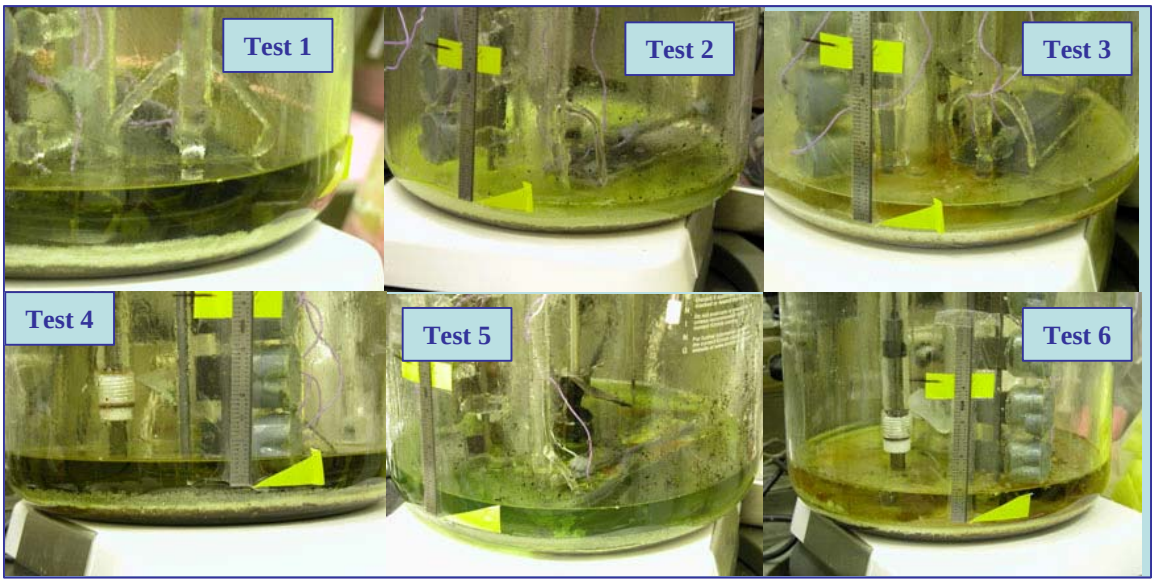

Figure 13. Dissolution Vessels for Tests 1-6 approximately 20 h after start of acid addition.

Figure 14 shows the six tests approximately 50 hours after the start of acid addition. Note that the acid addition rate of Test 2 continued to lag that used in the other tests. The liquid level in the Test 1 vessel reached the agitator at this point and mixing was initiated. The Test 3 and Test 6 (25 °C) vessels visually appeared to have less solids formation than the other tests (50 °C and 75 °C) apparently due to the reduced temperature. (This comparison is not obvious from the photos due to varying camera angle. Also, this observation is subjective.) The amount of sludge dissolved in the Test 3 and Test 6 vessels also appeared to lag the other vessels with the exception of Test 2. Test 2, again, showed an apparent slower rate of sludge dissolution due to the slower acid addition.

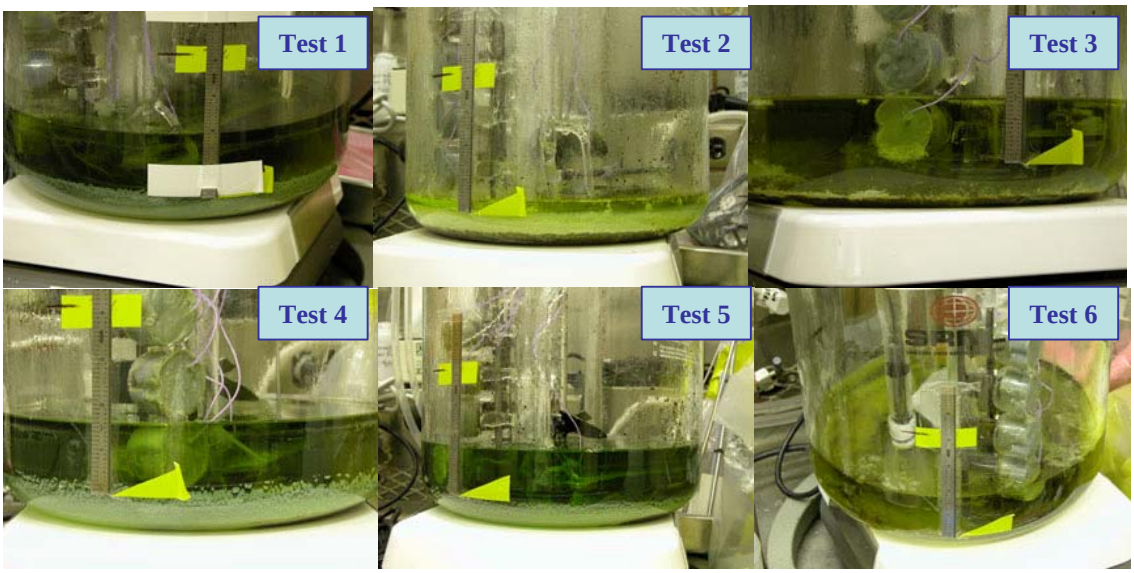

Figure 14. Dissolution Vessels for Tests 1-6 approximately 50 h after start of acid addition.

Figure 15 shows the vessels from Tests 2 though 6 approximately 70 hours after acid addition started. The Test 2 vessel continues to lag in the amount of acid added but by this point took on the characteristic emerald green coloring. All vessels showed the formation of light colored solids up the vessel side walls. At this time, the liquid level is the Test 3 vessel had reached the agitator and mixing was initiated. The Test 3 and Test 6 vessel contents had darkened from the bright emerald green to a more dark olive green coloration. The Test 3 and Test 6 vessels also developed whitish crystals that formed on several internal surfaces. Crystals were observed on metal, glass, plastic and carbon surfaces as well as the bulk liquid.

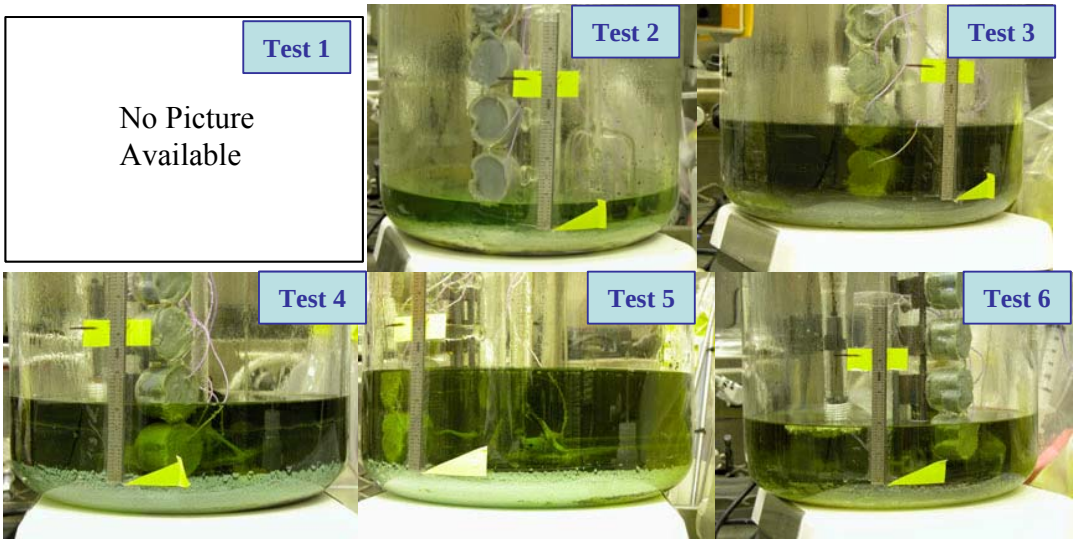

Figure 15. Dissolution Vessels for Tests 2-6 approximately 70 h after start of acid addition.

Figure 16 shows the Dissolution Vessel for Tests 1 and 3-6 approximately 90 hours after the start of acid addition. All tests appeared similar by this point. All had the dark green coloring with the accumulation of light colored solids in the bottom and up the sides of the vessel. The Test 3 vessel uniquely developed a haze up the vessel side walls. Significant gas generation continued to be evident in all vessels. Large quantities of small gas bubbles were observed throughout all test vessels.

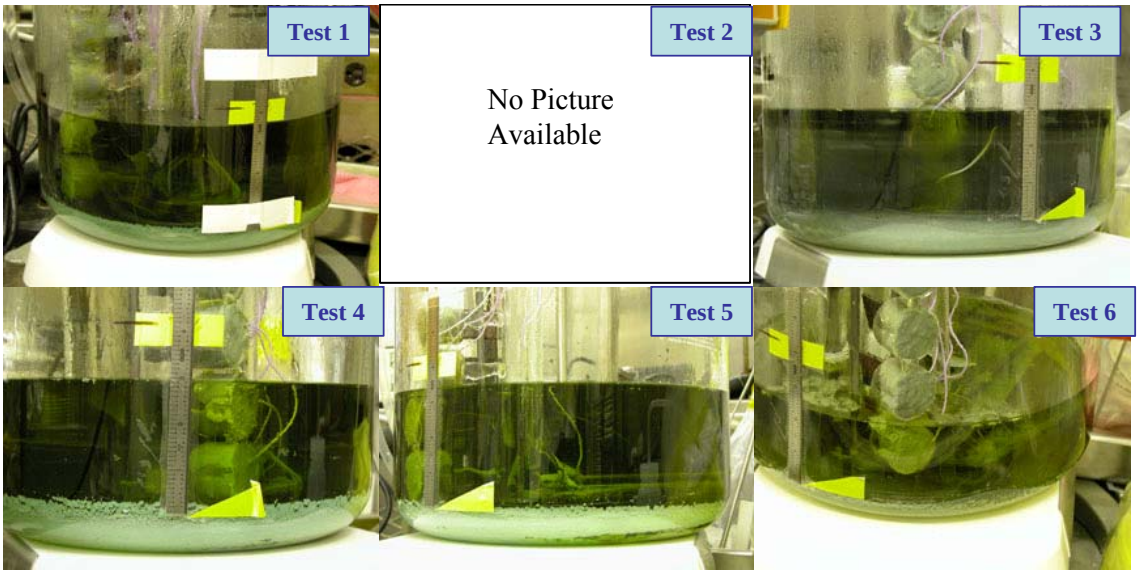

Figure 16. Dissolution Vessels for Tests 1, 3-6 approximately 90 h after start of acid addition.

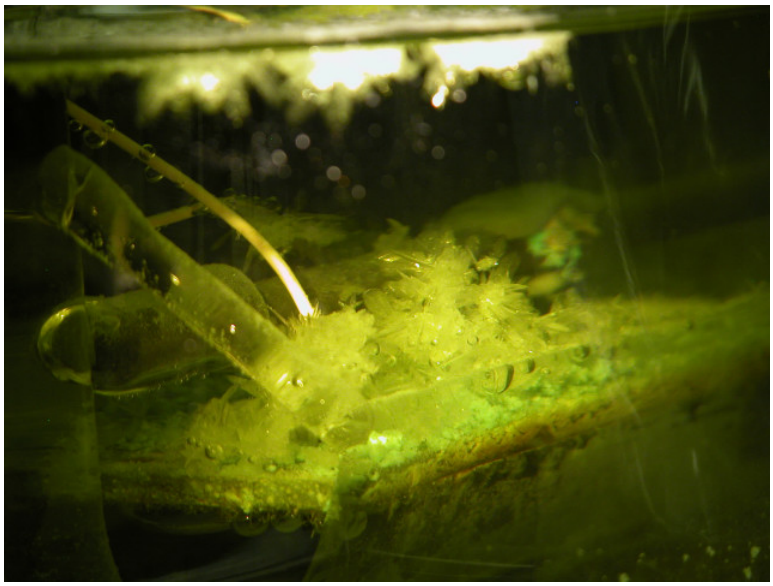

Figure 17. Dissolution Vessel for Test 6 showing gas bubble formation approximately 90 h after start of acid addition.

Figure 17 shows the development of crystals as well as the small gas bubble formation for Test 6 (25 °C, unmixed). The figure shows the crystal growth on the horizontal metal coupon. The crystals floating above the horizontal coupon (not in focus) are buoyed (i.e., suspended in the liquid) by adhering gas bubbles. Test 3 (25 °C, mixing) also experienced crystal formation prior to the start of mixing. Once the haze formed on the vessel walls it became difficult to observe the crystals. The initiation of mixing appeared to reduce the presence of crystals in Test 3.

Figure 18 shows the dissolution vessels for Tests 3 through 6 approximately 120 hours after the start of acid addition. The mixer for Test 2 (picture unavailable) was started approximately 10 hours prior to this time. All tests showed the similar green coloring. The haze formed during Test 3 showed signs of flaking off of the vessel walls. The Test 6 vessel continued to have large crystals attached to the vessel contents as well as floating crystals. The floating crystals appeared buoyed (i.e., suspended in the liquid) by adhering gas bubbles. The Test 6 vessel also visually appeared to have the least amount of the light colored solids found in all tests.

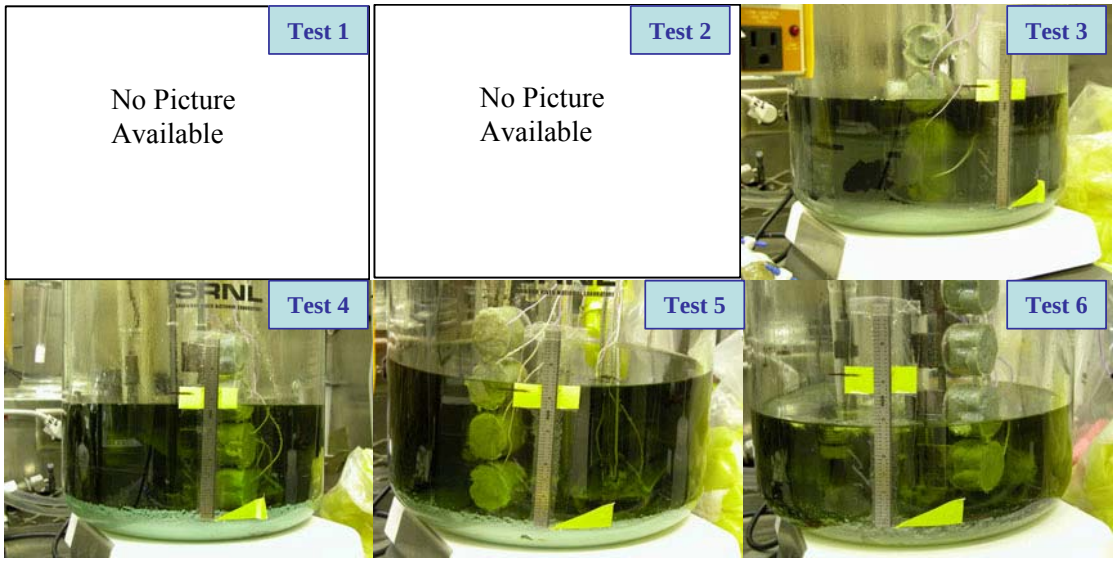

Figure 18. Dissolution Vessels for Tests 3-6 approximately 120 h after start of acid addition.

Figure 19 shows the Test 3-6 vessels approximately 140 hours after the start of acid addition. Acid addition for Test 1 (photo unavailable) completed at this time (139 hours after start of acid addition). All test vessels continued to show significant gas generation. Large sections of the haze on the Test 3 vessel started to flake off. The Test 6 vessel showed significant crystal growth and appeared to show less solids growth up the side walls. Generally, there appeared to be little change between the vessels from 120 hours after start of acid addition and 140 hours after the start of acid addition.

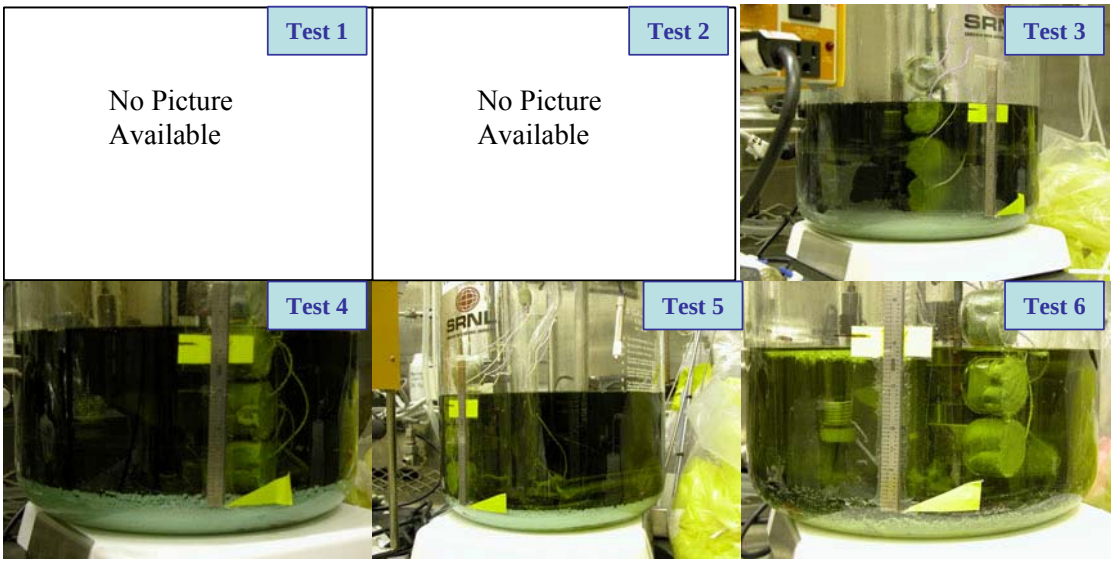

Figure 19. Dissolution Vessels for Tests 3-6 approximately 140 h after start of acid addition.

Figure 20 shows a picture of the crystals on the corrosion measurement reference probe. Crystals were also observed on other surfaces throughout the vessel. We presume that the lack of mixing and cooler temperature allowed the crystals to persist through the duration of the experiment.

Figure 20. Crystal growth on the reference electrode.

Figure 21 shows the vessels for Tests 2 through 6 at approximately 160 hours after the start of acid addition. All tests continued to show the dark green coloring of the bulk fluid. Significant gas evolution was still observed in all cases. Flakes of solids/corrosion products were observed in the Test 2 vessel. These flakes can be observed in Figure 21 in the top center picture with the

flakes seen in the lower left of the vessel protruding above the line of solids formed on the vessel bottom curvature.

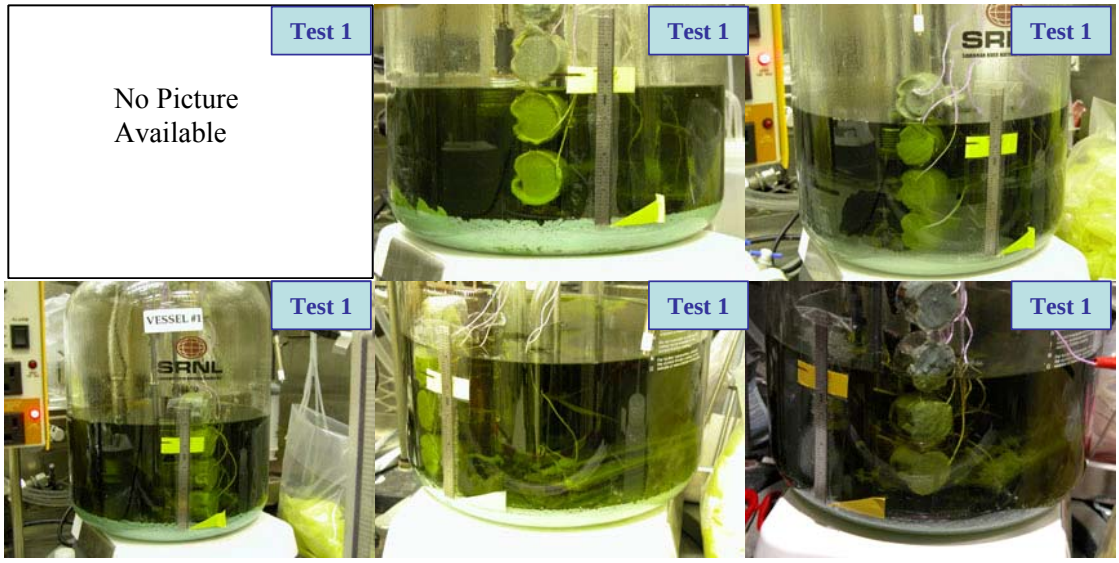

Figure 21. Dissolution Vessels for Tests 2-6 approximately 160 h after start of acid addition.

Figure 22 shows the daily samples taken during Test 5. The photo shows the color progression from the yellow/brown from the first sample (pH 12, leftmost photo), to the emerald green for the next two samples (pH 6 and 4 respectively). The remaining samples show the migration to a more olive green color (pH 1.5 and less).

Figure 22. Daily samples from Test 5 showing color progression of liquid from left to right.

It appears likely that an excess of acid led to the formation of the light colored solids. This is shown in Figure 23 as a sequence of three pictures from Test 5. The top picture is of the initial sludge and supernate prior to the start of acid addition. The amount of sludge is visible in the bottom of the vessel. The center picture shows the same vessel approximately 30 hours after the start of acid addition. It appears that a large portion, but not all, of the sludge has dissolved at this point and a small amount of light colored solids are beginning to form. As acid addition continues, more light colored solids begin to form in the bottom of the vessel and on the side

wall. This is illustrated in the bottom picture which was taken approximately 45 hours after the start of acid addition.

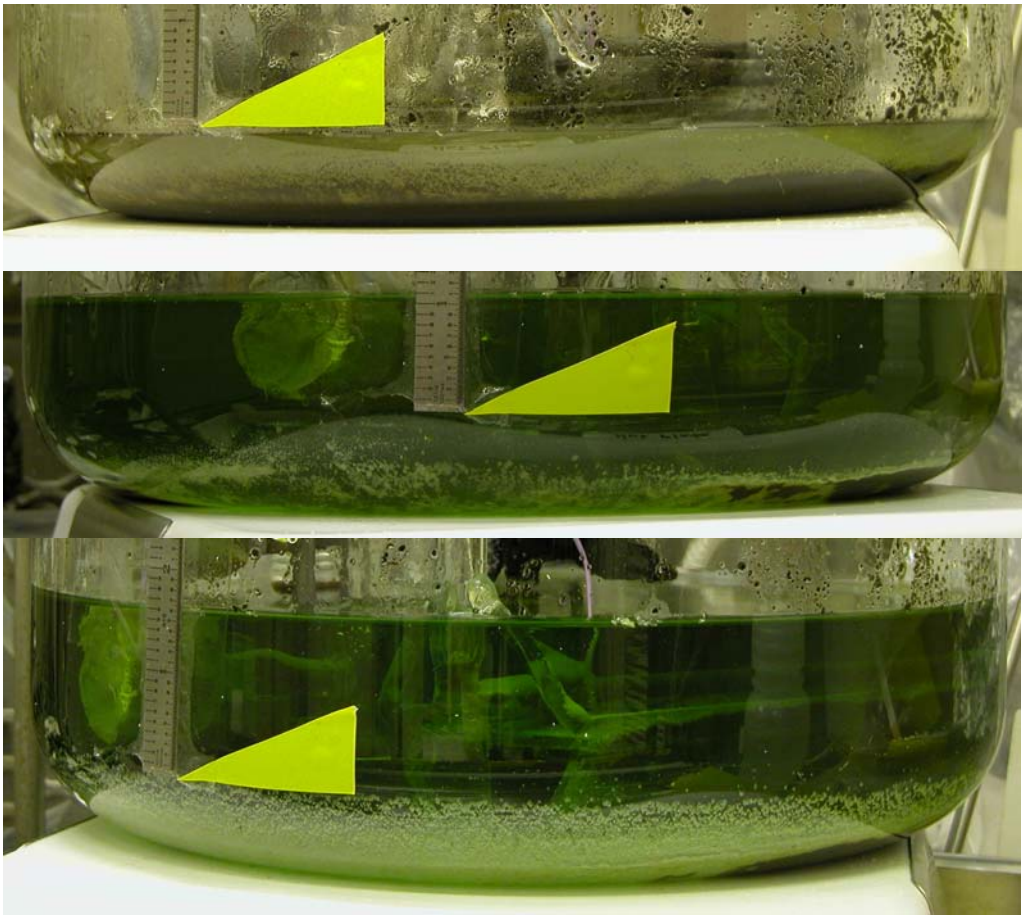

Figure 23. Test 5 initial sludge and solids at ~30 h and at ~45 h after start of acid addition.

Figure 24 illustrates the effect of temperature on the progression of the sludge dissolution and solids formation. The top picture was taken during Test 5 (75 °C, unmixed) approximately 30 hours after the start of acid addition. The center picture was taken approximately 115 hours after the start of acid addition. The bottom picture was taken during Test 6 (25 °C, unmixed) approximately 113 hours after the start of acid addition. Both the top and bottom pictures appear to have a comparable amount of sludge solids visible and a comparable amount of the light colored solids in the bottom of the vessel. The Test 6 vessel also shows large formations of crystals on the liquid surface, attached to the reference probe and on the horizontal metal coupon. The difference in temperature did not appear to change the amount of solids eventually formed, but appeared to change the rate of reaction throughout the test. The lower temperature tests generally appeared to progress slower than the higher temperature tests.

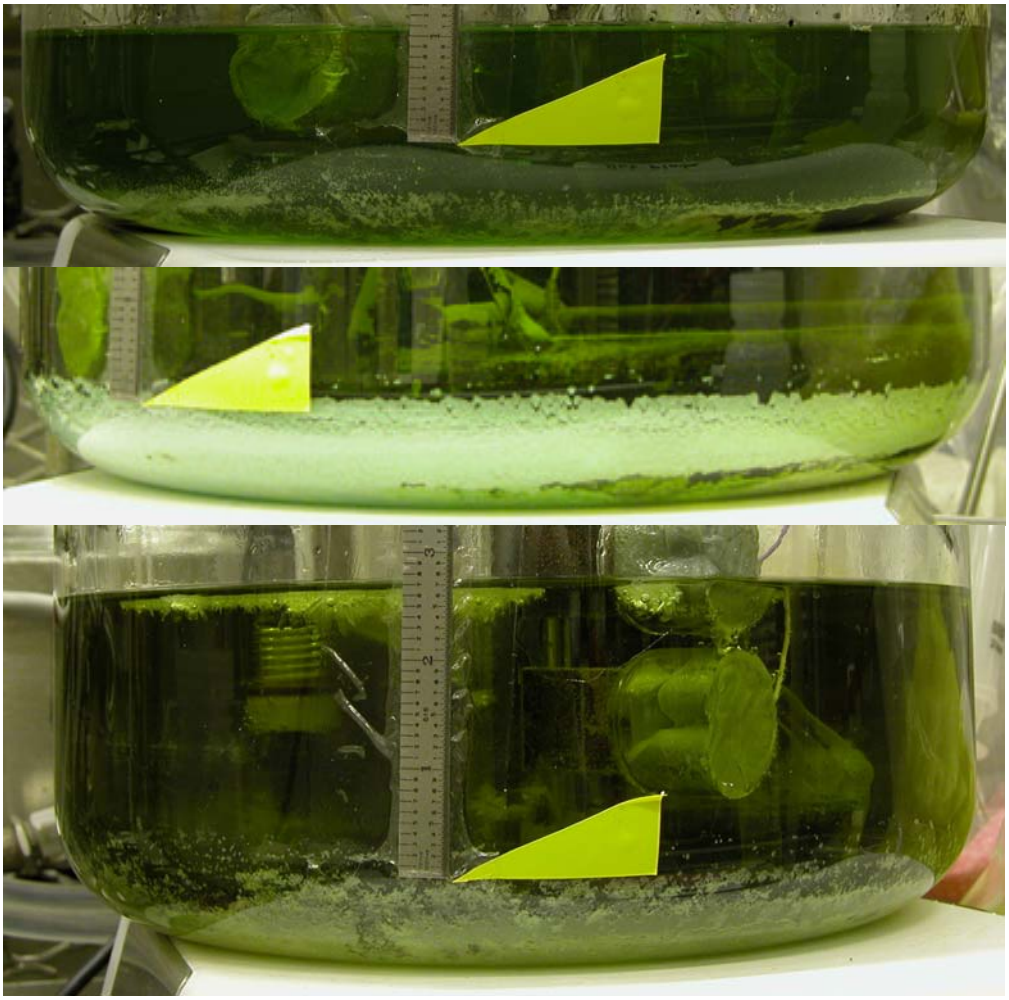

Figure 24. Solids 30 h and 115 h after start of acid addition in Test 5 (75 °C) vs. solids at 113 h after the start of acid addition in Test 6 (25 °C).

Transfer from Dissolution Vessel to Receipt Vessel

After completion of oxalic acid addition, the Dissolution Vessel was allowed to stand for 50 hours and then a portion of the vessel contents was transferred to a second vessel containing 5 L of simulated Tank 7F supernate. The Dissolution Vessel contents were transferred at rates that approximately represent the highest available pumping rates of existing Tank 5F equipment. Figure 25 shows the Receipt Vessel representing the receipt tank. All tests behaved in a similar manner during the transfer from the Dissolution Vessel to the Receipt Vessel.

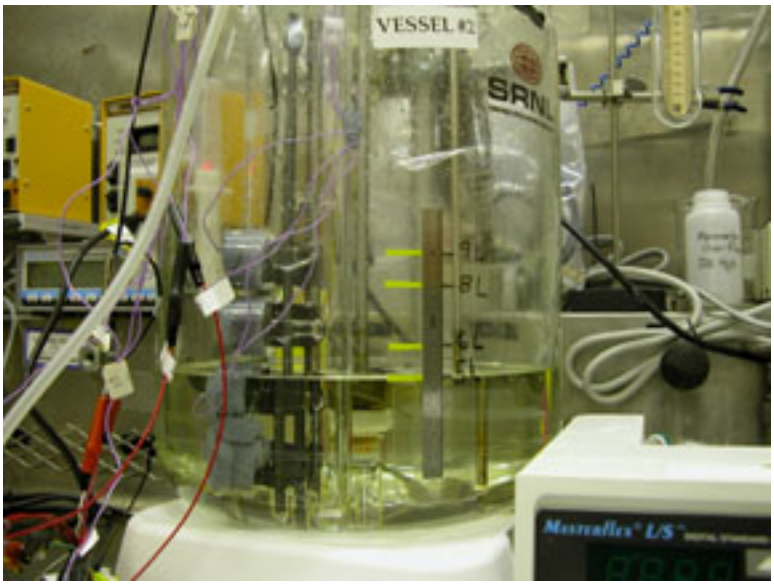

Figure 25. Receipt Vessel charged with Tank 7F simulated supernate prior to transfer of spent acid from Dissolution Vessel.

As the transfer started from the Dissolution Vessel to the Receipt Vessel, the Dissolution Vessel material rapidly rose to the top of the liquid in the Receipt Vessel due to density difference. A brown layer formed on the surface of the Receipt Vessel as the neutralization resulted in the precipitation of the dissolved solids from the Dissolution Vessel solution. Eventually, a channel was formed of the precipitated solids around the submerged transfer tube. Figure 26 shows these details from Test 1. Notice the solids completely engulf the feed tube restricting interaction with the bulk fluid. Figure 26 also shows the early stage of the low density layer forming on top of the bulk solution. These "floating" solids sank to the bottom of the vessel within several hours of formation. At the end of the transfer (17-18 hours) almost all of the solids were on the bottom of the vessel.

The transfer from the Dissolution Vessel to the Receipt Vessel used submerged tubes cleared of air prior to the transfer. Hence, minimal air was ingested during the transfer. The bilious dispersed solids apparently form without complete mixing of the transferred acid with the surrounding supernate. The low density fluid adhered to the solids and floated. Over time, diffusion of caustic and acid occurred to a sufficient extent – or nucleation and growth of solids occurred – such that the floating precipitates settled to the bottom of the vessel and compacted. The presence of trapped gas in the floating layer is not probable. First, visual inspection did not indicate a high population of gas bubbles on the solids. Second, if the solids did contain trapped gas, then upon release of the gas the entire liquid level would drop by a distance corresponding to the difference between the thickness of bilious solids and the compacted settled solids layers. No measurable drop in liquid level occurred.

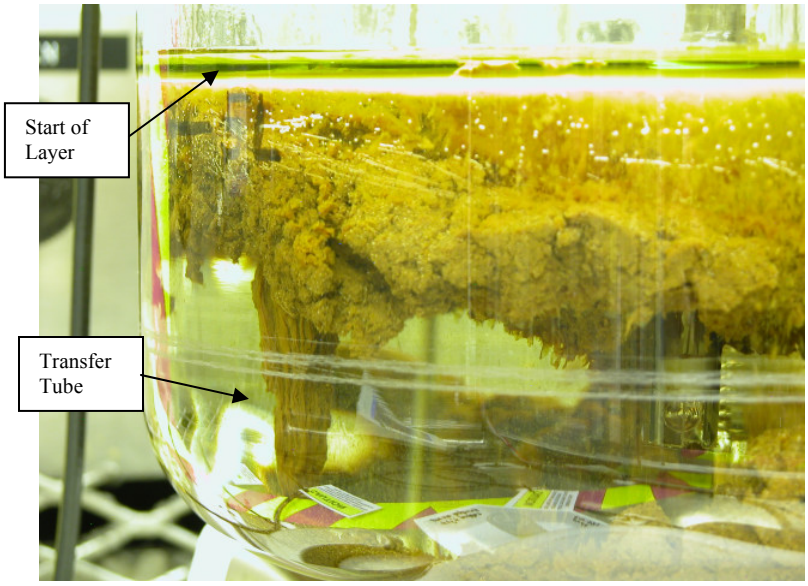

Figure 26. Feed tube and floating solids from Receipt Vessel.

As the transfer continued, three distinct layers formed in the Receipt Vessel. The limited mixing and the different densities of the acid and Tank 7F simulated solution allowed the various layers to segregate. A layer of the transferred the Dissolution Vessel material started to build up. Soon, three distinct layers were observed in the Receipt Vessel; the lower supernate layer containing precipitate solids that eventually sank, a middle turbid zone, and an upper layer of the Dissolution Vessel acid. An example of the vessel contents in three zones is shown as Figure 27. The pH was measured by sampling each layer during the tests. The pH of the lower layer (supernate) was typically +12, the pH of the turbid layer varied depending on the sample but was generally basic (pH 8-10), and the top layer had a low pH (2.2) when the samples were taken immediately after the transfer was completed. Samples obtained from the top liquid layer 4-5 hours later had reached a pH of 7.

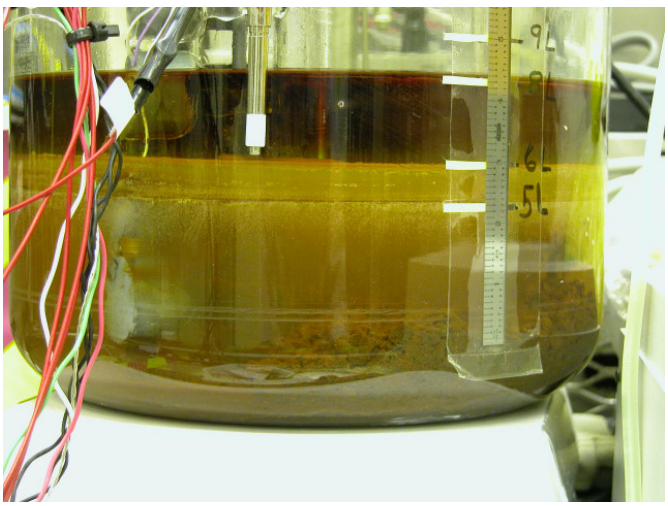

Figure 27. Test 5 Receipt Vessel after transfer of spent acid showing layer formation.

After the transfer from the Dissolution Vessel completed, we injected air from a syringe through a fine pore sintered metal aerator below the floating solids to determine if the suspended layer of solids would trap significant amounts of gas. Figure 28 shows the release of the air and the disturbance of the top liquid layer during the process. Researchers limited the injection to no more than a few mL of gas. A small number of gas bubbles rose and adhered to the floating solids. The bulk of the gas stirred the solids and broke through rapidly to the surface. Within hours, the adhered gas bubbles appeared to release and the floating solids began to sink.

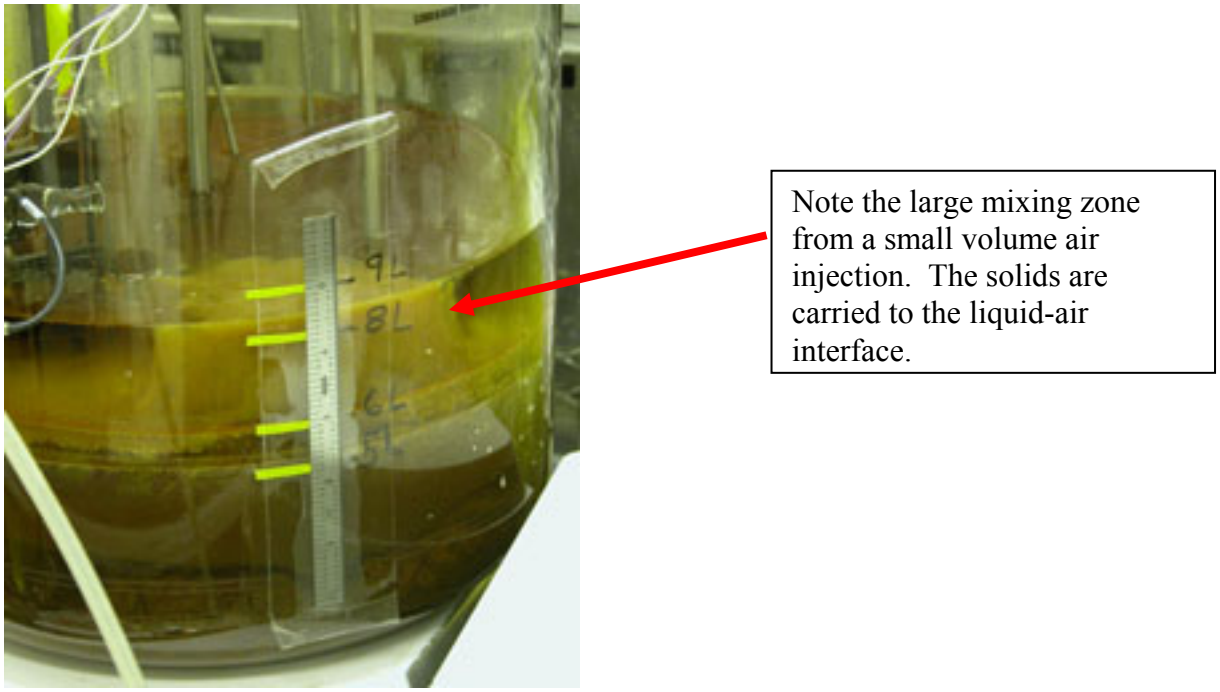

Figure 28. Receipt Vessel from Test 5 during aeration.

The mixer was then operated to determine the amount of mixing required to mix the separate liquid layers. Figure 29 shows a sequence of dated pictures during the mixing sequence. The agitator was set at 60 rpm, or the equivalent mixing energy of the smaller recirculation pumps proposed for Tank 5F. As can be seen in the figure, the layers mixed rapidly with a minimal amount of energy. Note that this mixing energy was insufficient to suspend the precipitated solids. When personnel increased the agitator speed to 180 rpm, the equivalent energy for a standard slurry pump, the solids were suspended with the exception of material near vessel hardware. When the agitator speed was increase to 240 rpm, the equivalent of the quad volute slurry pump, all material appeared suspended.

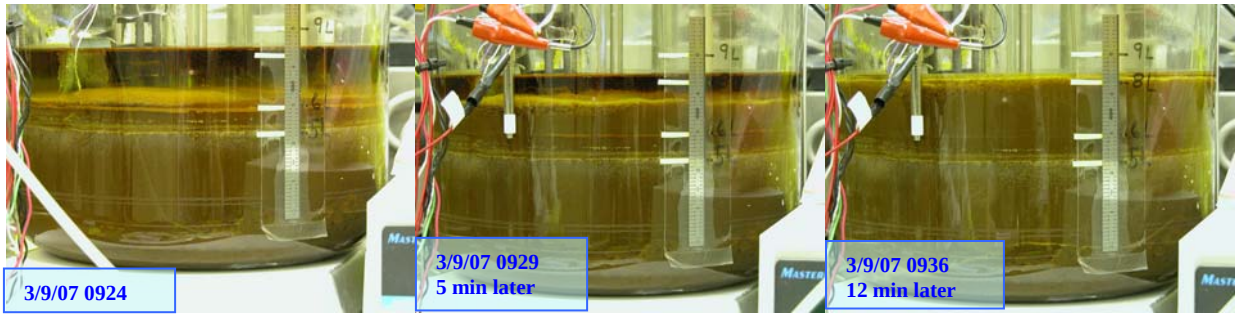

Figure 29. Test 5 Receipt Vessel showing mixing of layers.

The agitator speed was then increased to 270 rpm, the equivalent of the Submersible Mixing Pump (SMP), to assure that the precipitates solids could be suspended. After visual inspection indicated good solids suspension, mixing was stopped and the material allowed to settle. Figure 30 shows the receipt vessel after settling overnight. Two distinct layers of solids formed. The bottom layer was a more granular solid with a light-brown color. The upper layer appeared to be small "fluffier" solids that took longer to settle. The thickness of the layers shown in Figure 30 is not representative of the actual layer thickness. The bottom layer appears thicker in the picture than in actuality due to the curved walls of the vessel. The solids followed the contour of the vessel giving the illusion of a thick layer.

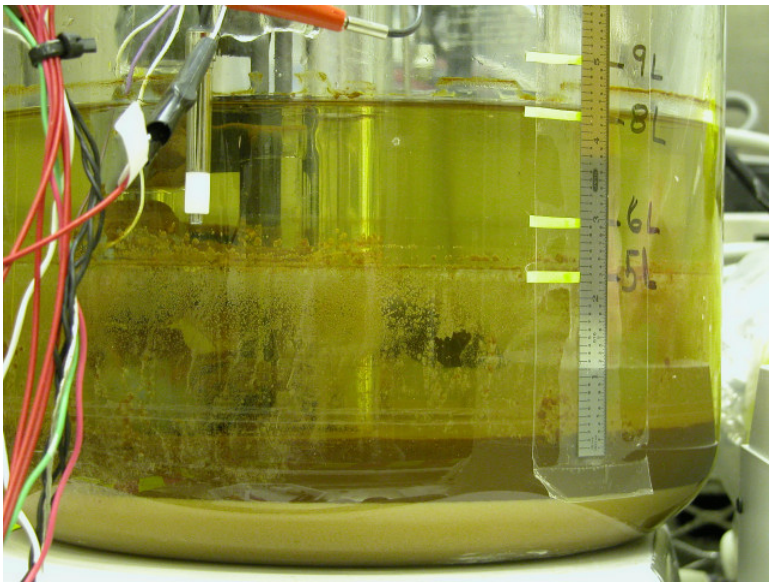

Figure 30. Test 5 Receipt Vessel after settling of solids.

Mixing of Dissolution Vessel

After the transfer from the Dissolution Vessel to the Receipt Vessel, the remaining contents of the Dissolution Vessel were mixed in an attempt to slurry the solids that formed in the dissolution tank. The mixer was increased in stages to 270 rpm, the same energy as an SMP. The vessel was left to mix for two days. Figure 31 shows a picture of the resulting slurry. While

a significant fraction of material had been suspended, there was also a significant portion of material stuck to the vessel walls and internals.

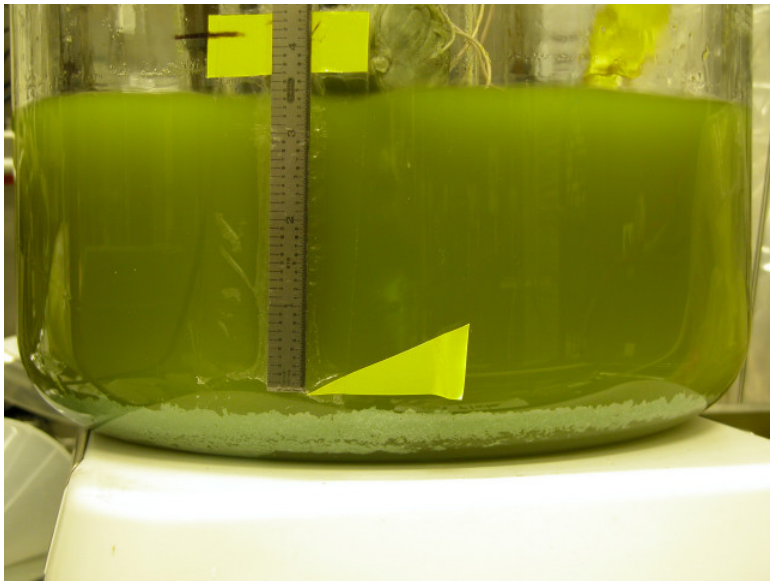

Figure 31. Post transfer mixing of Dissolution Vessel for Test 4.

Figure 32 shows the condition of the horizontal corrosion coupon – analogous to the tank bottom – after removing the slurry from the vessel. Solids adhered to the coupon and were not removed during mixing.

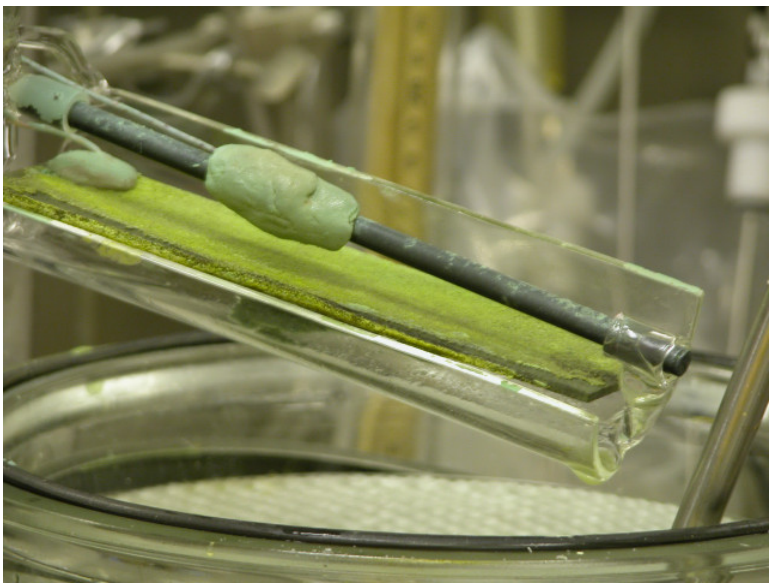

Figure 32. Removal of horizontal "coupon holder from Test 4 Dissolution Vessel.

Clinging solids also formed in the receipt vessel. As could be seen on the vessel side walls in earlier photos and the vertical coupon tree shown in Figure 33, solids adhered to the vessel walls and internals. They appeared more prominent at the interface between the two layers and persisted even after attempts to mix the contents. Solids adhered to the stainless steel, the glassware and to the graphite electrodes.

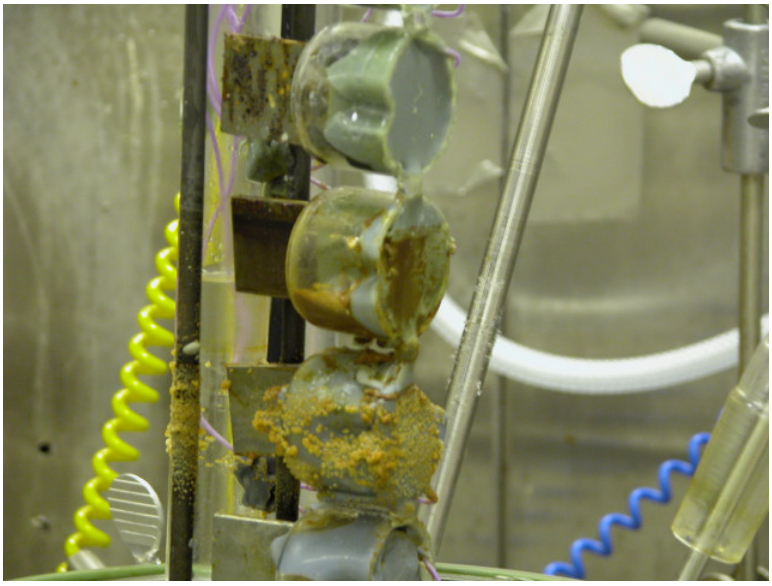

Figure 33. Removal of corrosion coupons from Test 1 Receipt Vessel.

Dissolution Vessel Solids Suspension

Approximately 5 grams of the solids left in the Dissolution Vessel from Test 4 (50 °C, unmixed) were added to each of three beakers containing simulated supernate, inhibited water and 8 wt % oxalic acid, respectively. These "screening tests" examined which solution would more effectively remove solids left in after dissolution (i.e. in Tank 5F after the first acid cleaning cycle). The beakers were then agitated using a magnetic stirring plate. The slurries are shown as Figure 34 as they appeared after a couple hours of stirring time.

Figure 34. Test 4 Dissolution Vessel solids added to (from left to right) simulated supernate, inhibited water and 8 wt % oxalic acid.

The slurry with the simulated supernate had two distinct layers. The dark top layer was significantly less dense than the bottom layer. The slurry also left a ring of residue on the beaker. The inhibited water slurry had a tan color with the solids settling less rapidly, approximately one-third the settling rate of the other slurries. The oxalic acid solution was a light green color with solids that would eventually settle over several hours leaving a clear supernate.

The solutions were examined after mixing overnight and are shown as Figure 35. The slurries in the inhibited water and oxalic acid appeared unchanged. The slurry in the simulated supernate was entirely the dark color and settled significantly more slowly than either of the other slurries.

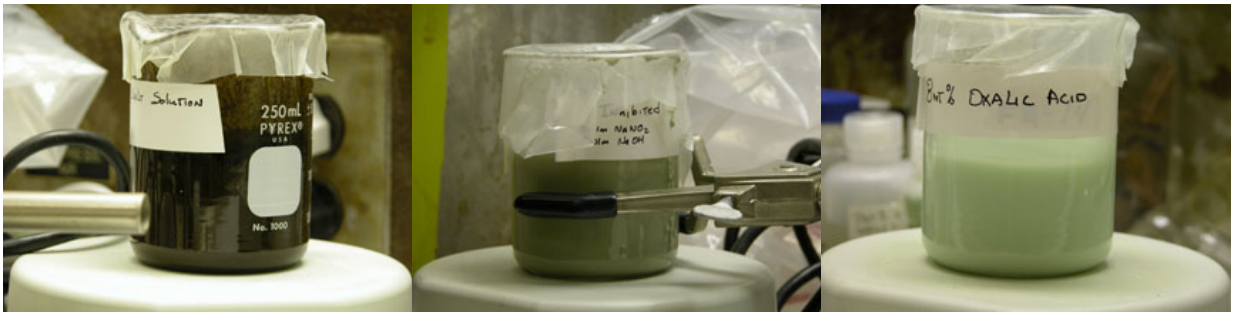

Figure 35. Test 4 Dissolution Vessel solids in (from left to right) simulated supernate, inhibited water and 8 wt % oxalic acid after stirring overnight.

These slurries are shown in Figure 36 after settling for several hours. Though the slurry with the simulated supernate settled the slowest, it also had the clearest supernate. None of the liquids appeared to have much success dissolving the original solids.

Figure 36. Test 4 Dissolution Vessel solids in (from left to right) simulated supernate, inhibited water and 8 wt % oxalic acid after settling.

Addition of simulated supernate, inhibited water or additional oxalic acid did not visually appear to dissolve the solid residues collected from the Dissolution Vessel. Addition of supernate did change the nature of the solids, but we do not verify whether the supernate would loosen solids adhered to the metal surfaces. The addition of the inhibited water (0.01 M NaOH) also affected changes to the solids though not as dramatically. Again, it is unknown if adhered solids would

become mobile in presence of inhibited water. The addition of extra (8 wt %) oxalic acid appeared to have very little effect on the solids.

The precipitate from the beaker containing the Dissolution Vessel solids and the simulated supernate were submitted for XRD analysis with results shown in Figure 37. The primary phase is a sodium oxalate with minor amounts of sodium nitrate, quartz and sodium-hydrogen-oxalate. An amorphous iron compound was also identified.

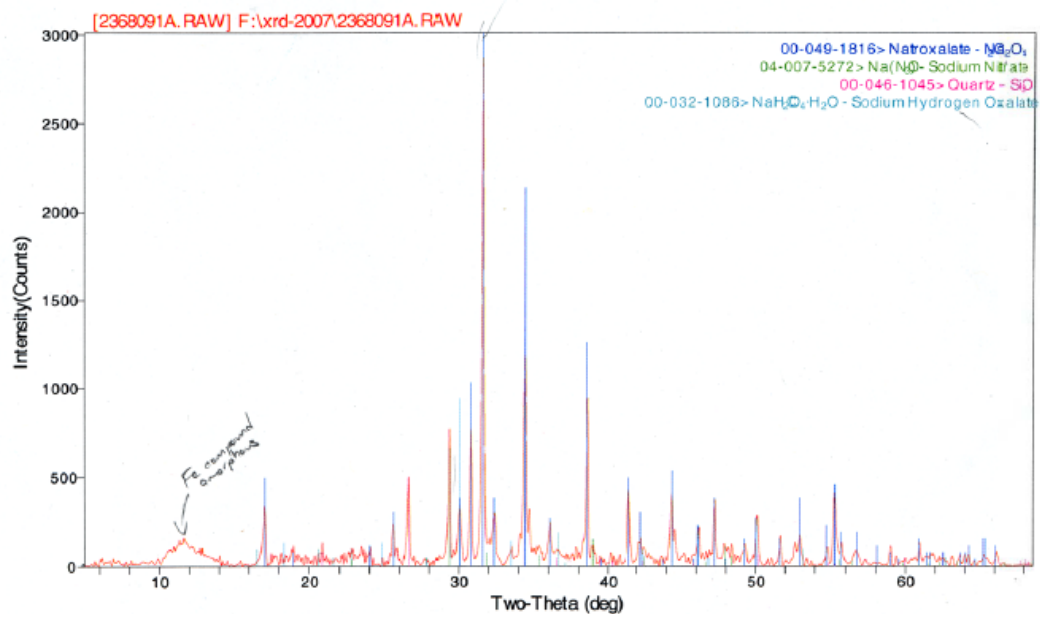

Figure 37 XRD of Vessel 1 Solids with Simulated Supernate

Exit Gas Composition

Test 1: 50 °C with Mixing

During the simulant demonstration tests, personnel purged the vapor space of the Dissolution Vessel with air and a helium tracer (17.1 cm^3/min air and 0.1 cm^3/min helium for Test 1). (Initially personnel established a He flow of 35 cm^3/min but subsequently reduced this flow to allow greater sensitivity for hydrogen detection.) Following its exit from the Dissolution Vessel, the vapor passed through a condenser and a chiller to remove water vapor. Following these processed steps, the vapor phase was analyzed with an online GC. Figure 38 shows the composition of the vapor as a function of time for Test 1.

The plot shows the concentration of helium, hydrogen, oxygen, and nitrogen during the test. It also shows the sum of these gases as a function of time. At the start of the test, the vapor phase contained ~ 80% nitrogen and ~ 21% oxygen, which is close to the composition of air. After approximately 5 hours, the sum of the concentrations of helium, hydrogen, oxygen, and nitrogen was less than 100%. The likely cause of the difference is carbon dioxide, which could not be

measured with the GC used in Tests 1 – 3.[b] After approximately 30 hours, the concentration of the unmeasured gas was approximately 20% of the total. The unmeasured gas concentration decreased from ~ 20% after 30 hours to 0% after 84 hours. Between 140 hours and 150 hours, the unmeasured gas concentration increased to 40% of the total. No hydrogen was detected in the gas during this test. (Detection limits for hydrogen ranges between 2-6 ppm during most of the experiments.)

Periodically throughout all the tests, the GC showed random presence of a trace amount of a low molecular weight (i.e., short retention time) component. Despite attempts to identify this gas – through offline analysis of grab samples, addition of a second GC column, and consultation with the vendor representative for the GC (see Gas Sample Analyses for a more complete discussion) – the compound remains unknown. The amount present is too small to see in Figure 38.

Figure 39 shows the ratio of nitrogen to oxygen during the test. Since the purge gas contained 80% nitrogen and 21% oxygen, this ratio should be 3.8. A nitrogen-to-oxygen ratio greater than 3.8 indicates that oxygen is being consumed by a chemical reaction occurring in the Dissolution Vessel. A ratio less than 3.8 would indicate that oxygen is being generated by a chemical reaction.

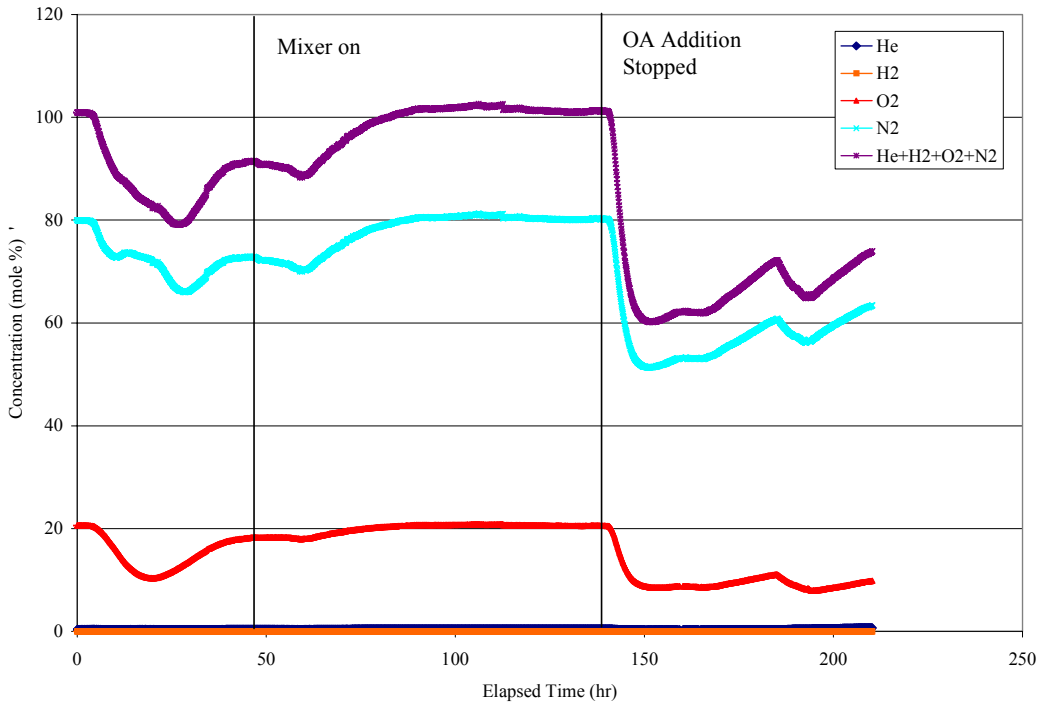

Figure 38. Composition of gas from Dissolution Vessel of Test 1 (50 °C, mixed).

[b] Carbon dioxide gas formed in concurrent tests with actual Tank 5F waste as measured using a gas chromatograph with a column designed for the measurement of carbon dioxide. Tests 4 - 6 in this series also later confirmed the formation of carbon dioxide as did the tests with simulated waste that examined the influence of radiation.

Shortly after the start of the test, the N_2:O_2 ratio increases from 3.9 to 7.0, indicating that oxygen consumption by a chemical reaction in the Dissolution Vessel. This result is consistent with the generation of an unmeasured gas (likely CO_2 based on analyses from subsequent tests) seen in subsequent tests. Between 50 hours and 140 hours, the N_2:O_2 ratio is ~ 3.9, indicating no net oxygen consumption. Between 140 hours and 150 hours, the ratio increases from 3.9 to 6.0, and it remained above 6.0 for the remainder of the test, indication oxygen consumption.

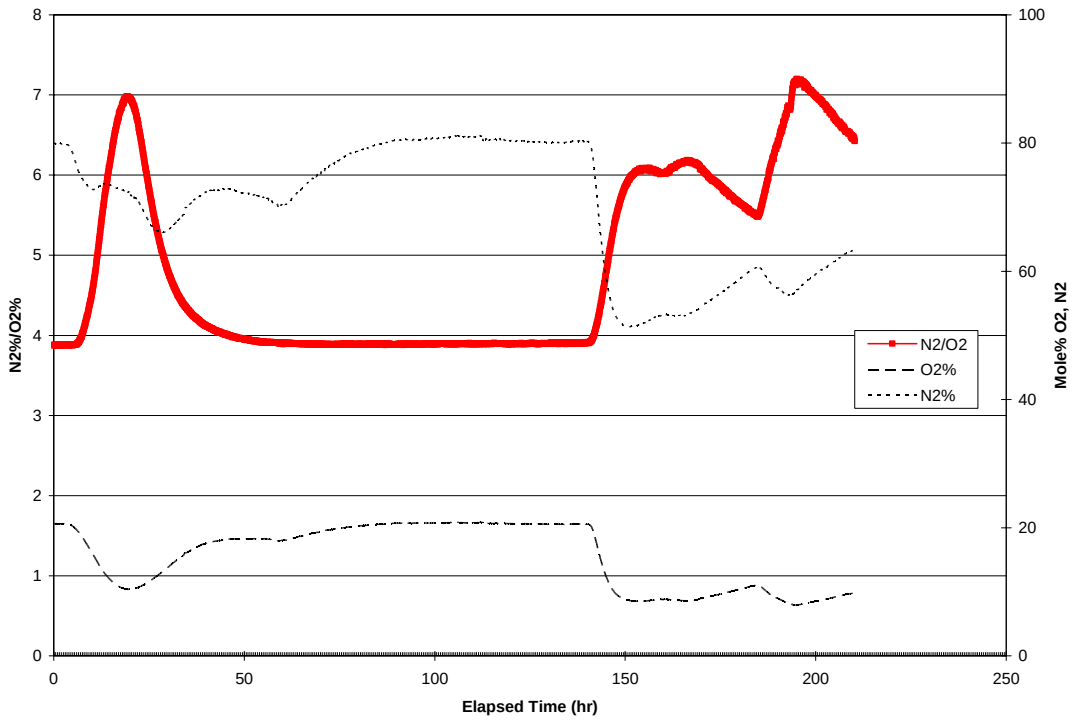

Figure 39. Nitrogen-to-oxygen ratio during Test 1 (50 °C, mixed).

The generation of CO_2 (the likely unmeasured gas) from corrosion would require consumption of oxygen as indicated by the reaction in equation 5. Note that part of the initial CO_2 comes from acid reaction with the carbonates in the supernate and sludge and this portion is not accompanied by oxygen consumption.

- Metal Dissolution Reaction
  $Fe^{0} \rightarrow Fe^{2+} + 2\,e^{-}$

- Cathodic Reactions
  $Fe^{3+} + e^{-} \rightarrow Fe^{2+}$
  $2\,H^{+} + 2\,e^{-} \rightarrow H^{2}$

- Oxygen Consumption
  $Fe^{2+} + \frac{1}{2}\,O_2 + 2\,H^{+} \rightarrow 2\,Fe^{3+} + H_2O$

- Precipitation and Carbon Dioxide Generation

  $Fe^{3+} + 3\ C_2O_4^{2-} \rightarrow Fe(C_2O_4)_3^{3-}$

  $Fe(C_2O_4)_3^{3-} + \text{light} \rightarrow Fe(C_2O_4) + 3\ (C_2O_4)^{2-} + 2\ CO_2$ equation 5

Test 2: 75 °C with Mixing

Figure 40 shows the composition of the vapor as a function of time for Test 2. The plot shows the concentration of helium, hydrogen, oxygen, and nitrogen during the test. It also shows the sum of the concentration of these gases as a function of time. At the start of the test, the vapor phase contained ~ 79% nitrogen and ~ 21% oxygen, which is close to the composition of air. After approximately 30 hours, the sum of concentrations of helium, hydrogen, oxygen, and nitrogen was less than 100%. As in Test 1, the likely cause of the difference is carbon dioxide, which could not be measured with the GC used in Tests 1 – 3. After approximately 60 hours, the unmeasured gas concentration was approximately 20% of the total. The unmeasured gas concentration was ~50% of the total after 90 hours and greater than 60% of the total after 160 hours. The unmeasured gas concentration decreased from 60% after 160 hours to less than 5% by the end of the test. No hydrogen was measured in the gas during this test (i.e., < ~5 ppm).

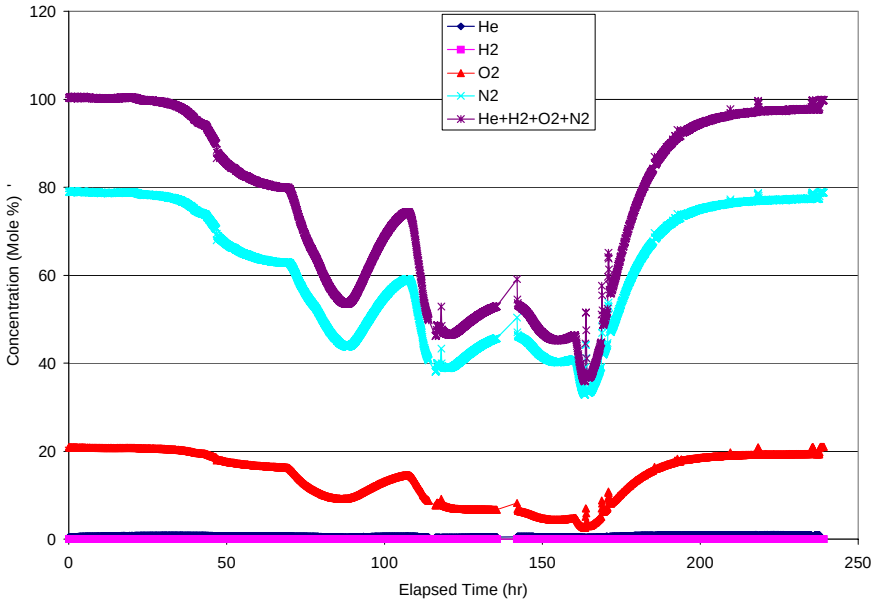

Figure 40. Composition of gas from Dissolution Vessel of Test 2 (75 °C, mixed).

Figure 41 shows the ratio of oxygen to nitrogen during the test. Shortly after the start of the test, the N_2:O_2 ratio is constant at ~3.8. Between 70 hours and 80 hours it increases from 3.9 to 4.9. It decreases to 4.1 at 110 hours, and then increases to 12.5 at ~ 160 hours. It decreases to 4.0 at 200 hours and remains there until the end of the test.

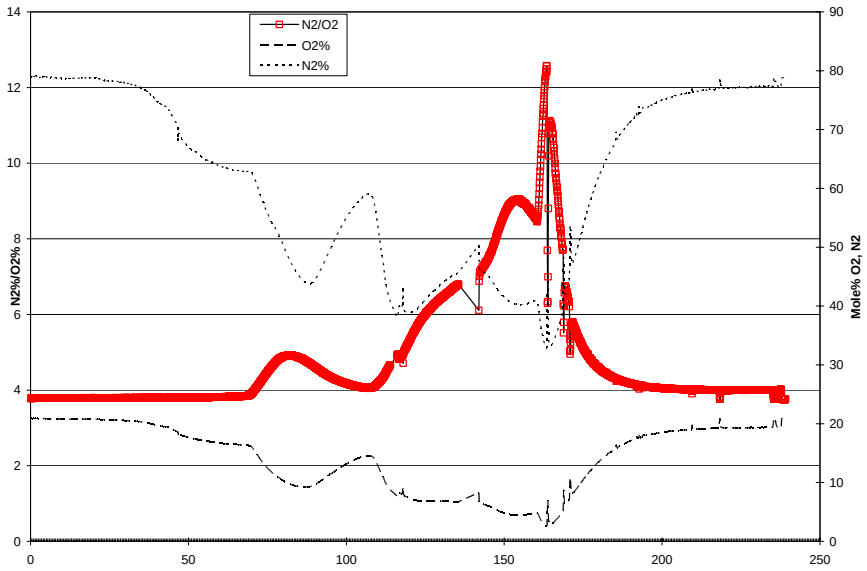

Figure 41. Nitrogen-to-oxygen ratio during Test 2 (75 °C, mixed).

Test 3: 25 °C with Mixing

Figure 42 shows the composition of the vapor as a function of time for Test 3. The plot shows the concentration of helium, hydrogen, oxygen, and nitrogen during the test. It also shows the sum of the concentrations of these gases as a function of time. At the start of the test, the vapor phase contained ~ 78% nitrogen and ~ 21% oxygen, which is close to the composition of air. After approximately 20 hours, the sum of the helium, hydrogen, oxygen, and nitrogen was approximately 85%. The likely cause of the difference is carbon dioxide, which could not be measured with the GC used in Tests 1 – 3. It remained steady at ~ 85% until 65 hours when it decreased to 75%. It then increased to ~ 90% at the end of the test.

Some hydrogen (< 0.005 mole %, < 50 ppm)) was detected during the test. Figure 43 shows the measured hydrogen during the test. The initial concentration is zero. Between 60 and 160 hours, hydrogen was measured. Mixing of the vessel started 66 hours after the start of acid addition. At this time, the mixer was touching the surface of the liquid. The mixing impeller became completely submerged over the next 24 hours. The GC data shows no apparent peak of hydrogen generation or liberation during the mixing of the vessel. Also, at the conclusion of the test, personnel mixed the contents of the dissolution vessel by increasing agitator speed to the equivalent of a Submersible Mixing Pump without any detection of an increase in vapor space hydrogen. The maximum concentration was 42 ppm during the entire test. One can observe a lot of scatter in the measured hydrogen concentration. One reason for the scatter is that the hydrogen concentration is close to the detection limit of the GC (~2-6 ppm).

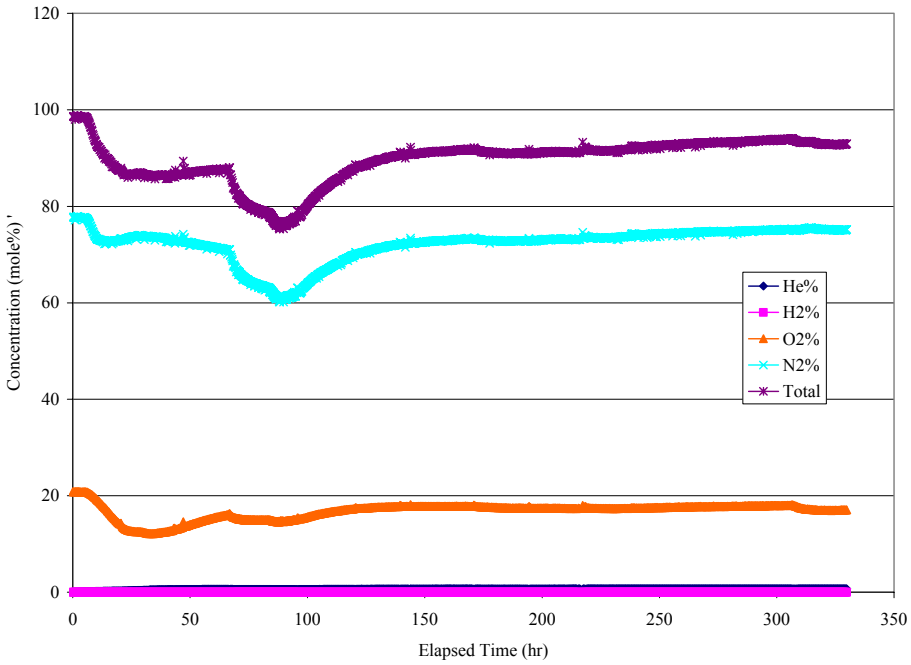

Figure 42. Composition of gas from Dissolution Vessel of Test 3 (25 °C, mixed).

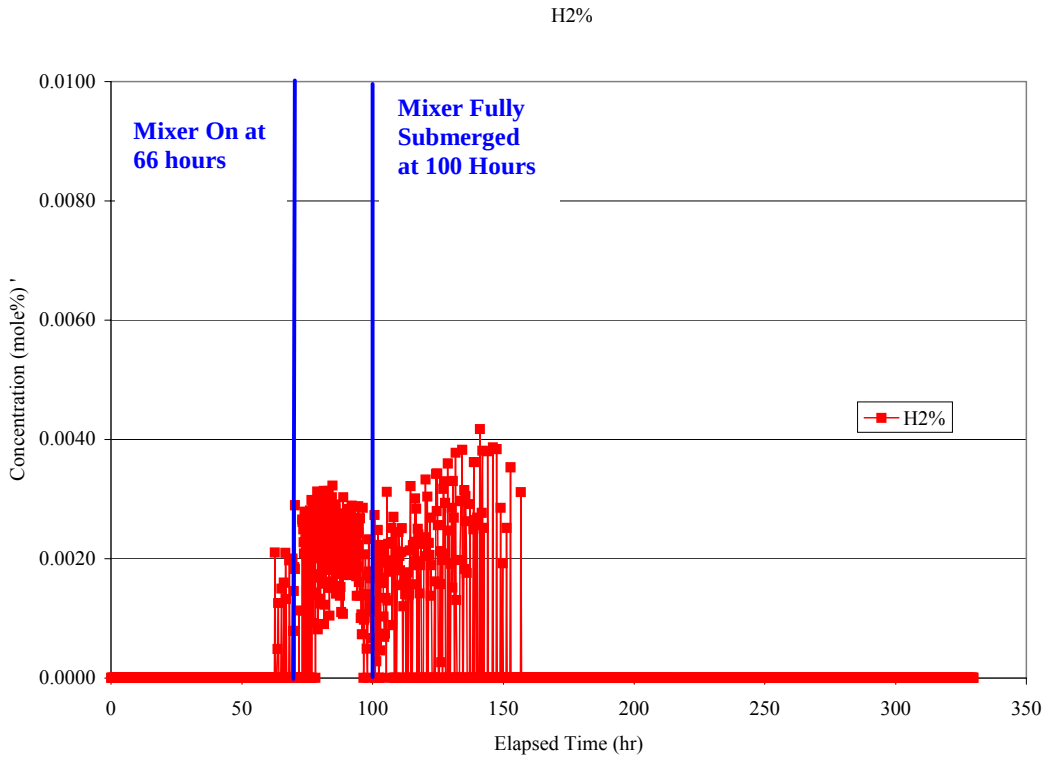

Figure 43. Hydrogen (mol %) in gas from Dissolution Vessel of Test 3 (25 °C, mixed).

Figure 44 shows the ratio of nitrogen-to-oxygen during the test. Shortly after the start of the test, the N_2:O_2 ratio increases from 3.8 to 6.1, indicating that oxygen is being consumed by a chemical reaction in the Dissolution Vessel. After ~100 hours, the ratio decreases to 4.1 and remains between 4.1 and 4.2 until ~310 hours when it increases to 4.4. This result is consistent with Figure 42, which shows an unknown gas being formed throughout the test (i.e., gas sums to <100%).

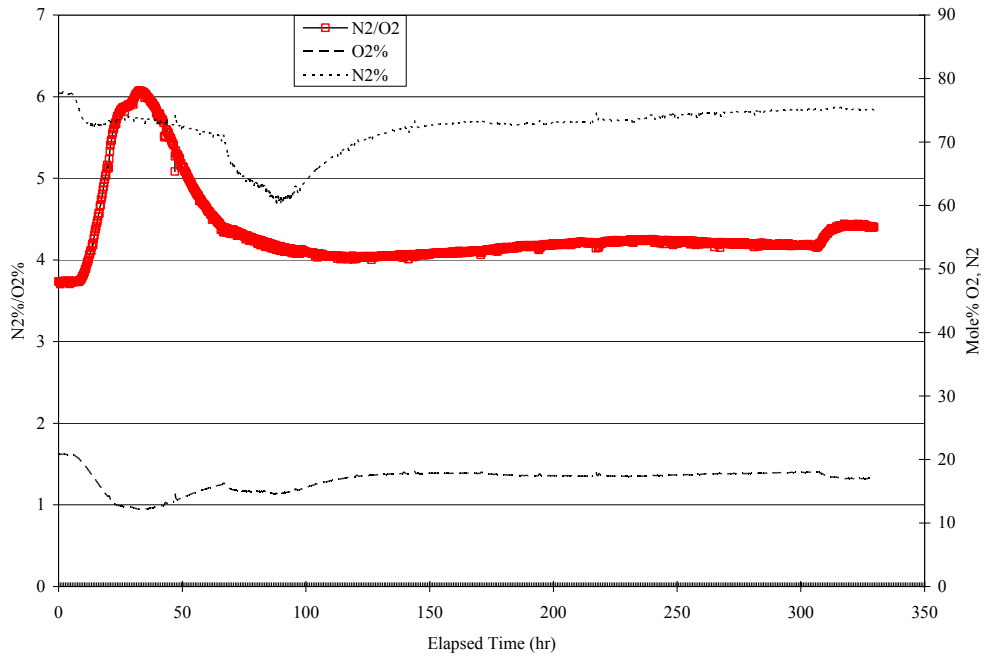

Figure 44. Nitrogen-to-oxygen ratio during Test 3 (25 °C, mixed).

Test 4: 50 °C without Mixing

Figure 45 shows the composition of the gas exiting from the Dissolution Vessel. During Tests 4 – 6, researchers added a second column to the GC to measure CO_2 and N_2O. The total measured gas was between 95 and 100% throughout the test. The measured CO_2 concentration was as high as 43% during the test. The measured N_2O was as high as 3.3%. The CO_2 was an order of magnitude higher than the N_2O, and over 95% of the exit gas was identified. Therefore, the unmeasured gas during Tests 1 – 3 was most likely CO_2.

Approximately 6 hours after startup, the measured CO2 started increasing and peaked at 25% after 37 hours. The CO_2 concentration decreased and then started increasing after an additional 37 hours, reaching a maximum of 43% at 144 hours. After 144 hours, the CO_2 concentration decreased to ~ 4% at the end of the test.

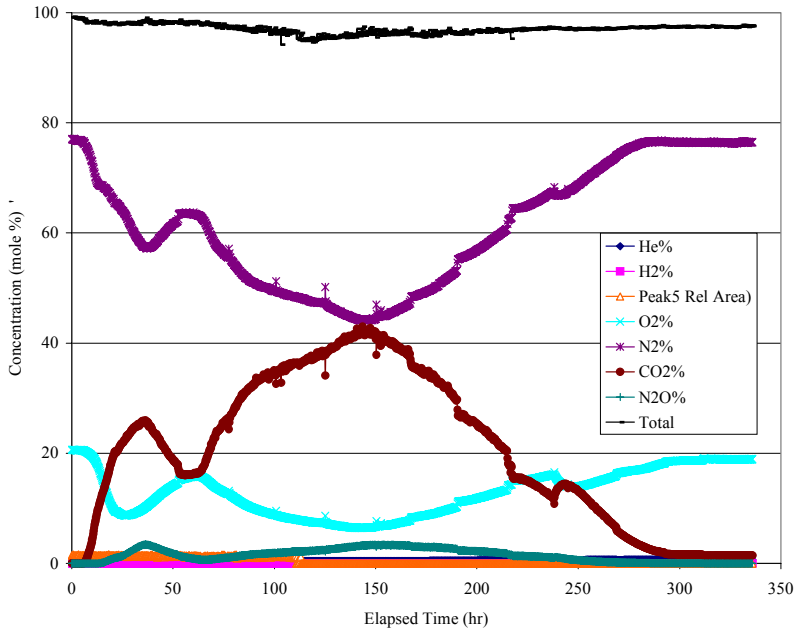

Figure 45. Composition of gas from Dissolution Vessel of Test 4 (50 °C, unmixed.

Figure 46 shows the measured hydrogen during the test. (The randomly appearing unknown gas is labeled "Peak 5"). Hydrogen is observed between 50 and 100 hours. The maximum concentration is 170 ppm. Hydrogen is also observed at the end of the test (310 – 335 hours). The concentration is less than 50 ppm. Note that personnel started the mixer 237 hours after the start of acid addition and mixed for the next 98 hours at a constant 270 rpm. As seen in the figure, the mixer did not induce the release of hydrogen at the end of the experiment.

Figure 47 shows the N_2:O_2 ratio during the test. Initially, the ratio is 3.7, which approximates the ratio in air. After 12 hours, the ratio increases and reaches 7.3 after 26 hours. This peak is at approximately the same time as the first peak in the CO_2 concentration. The ratio decreases to 4 after ~ 50 hours, and then increases to 6.9 after 143 hours. This second peak is consistent with the second peak in the CO_2 concentration. The N_2:O_2 ratio decreases to 4 at the end of the test. A third peak is observed at 250 hours, which is consistent with a third peak in the CO_2 concentration.

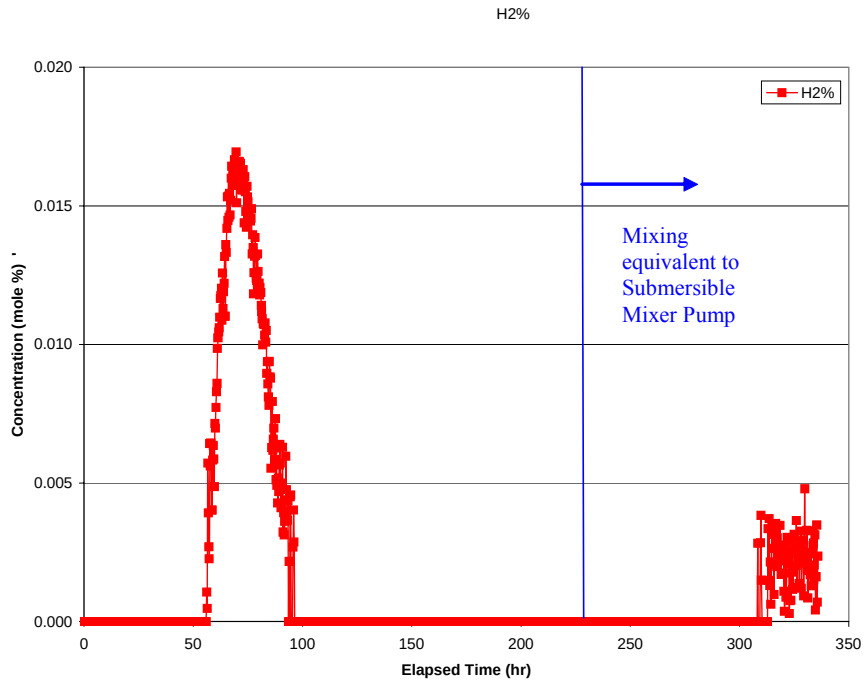

Figure 46. Hydrogen (mol %) in gas from Dissolution Vessel in Test 4 (50 °C, unmixed).

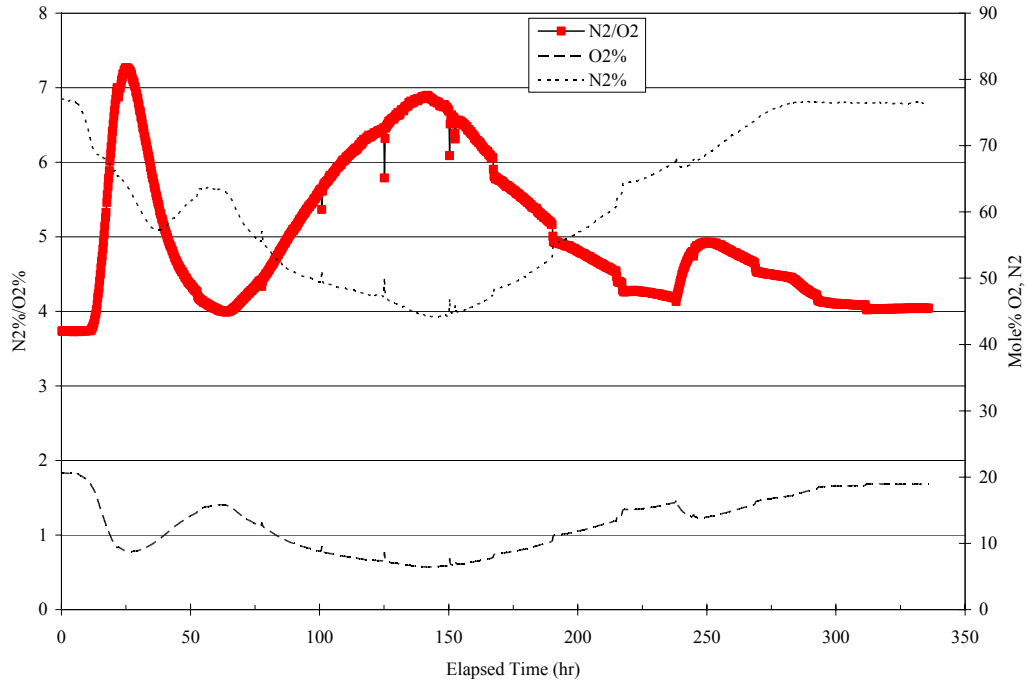

Figure 47. Nitrogen-to-oxygen Ratio during Test 4 (50 °C, unmixed).

Test 5: 75 °C without Mixing

Figure 48 shows the composition of the gas exiting the Dissolution Vessel during Test 5. The sum of the measured gases is between 95 and 100% throughout the test. The CO_2 concentration starts at zero and increases to 35% after 36 hours. It decreases to 14% after 65 hours, and then dramatically increases to 52%. Following the increase, it decreases to less than 1% by the end of the test. The N_2O shows similar behavior, but its concentration is about an order of magnitude less than the CO_2.

Figure 49 shows the measured hydrogen concentration during Test 5. No hydrogen is measured during the first 110 hours of the test. After 110 hours, hydrogen is detected, but the concentration is less than 80 ppm, which is close to the detection limit.

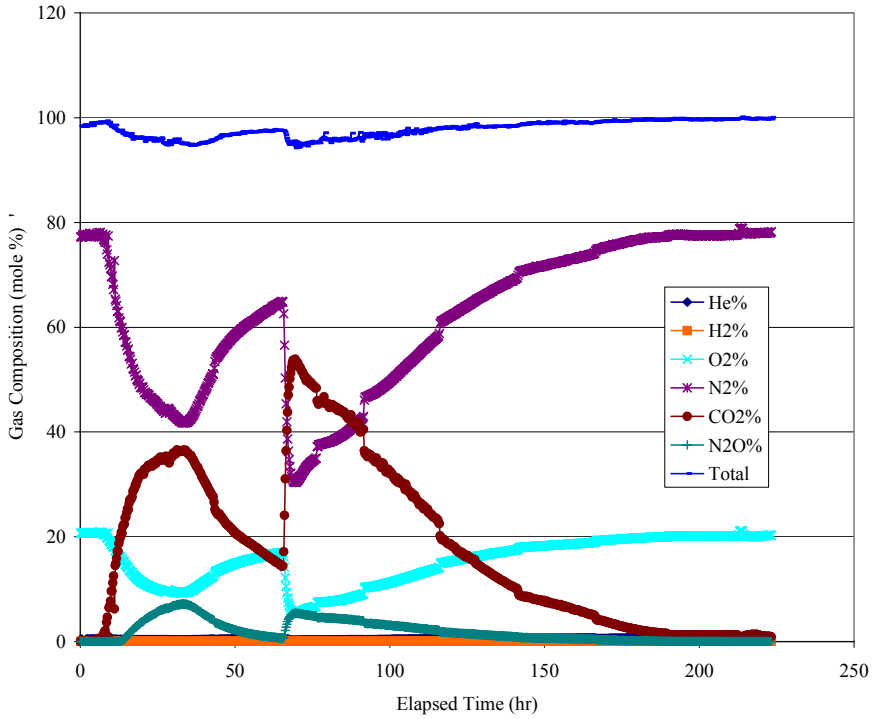

Figure 48. Composition of gas from Dissolution Vessel during Test 5 (75 °C, unmixed).

Figure 50 shows the N_2:O_2 ratio. The ratio starts at 3.7 which would be expected for air. After 28 hours, it increases to 4.6, and then decreases. After 66 hours, the ratio dramatically increases to 5.6 and then decreases to 3.8 by the end of the test. The changes in the N_2:O_2 ratio are consistent with the changes in the gas composition during Test 5.

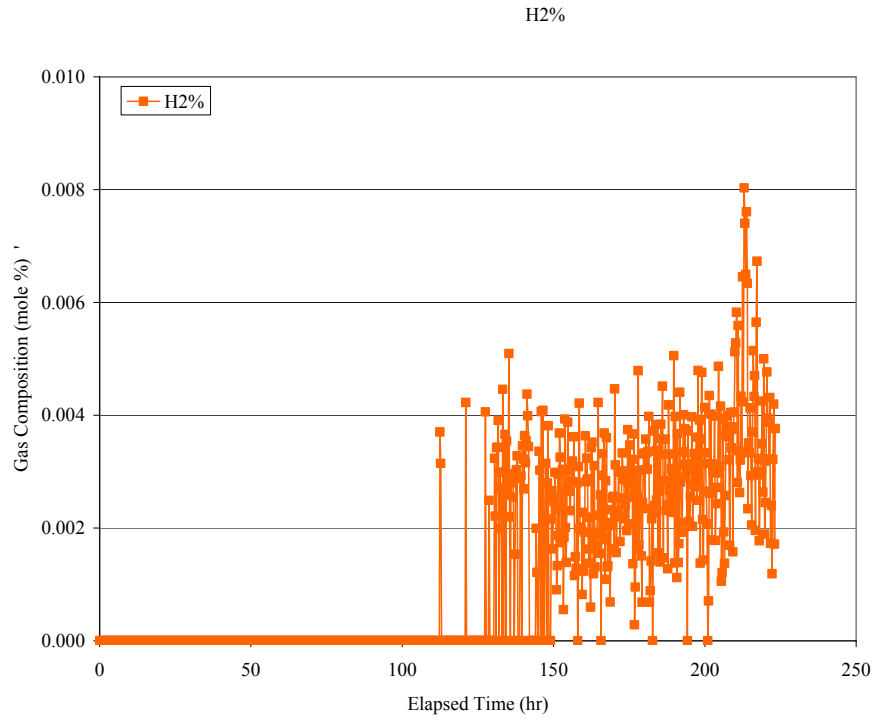

Figure 49. Hydrogen (mol %) in gas from Dissolution Vessel in Test 5 (75 °C, unmixed).

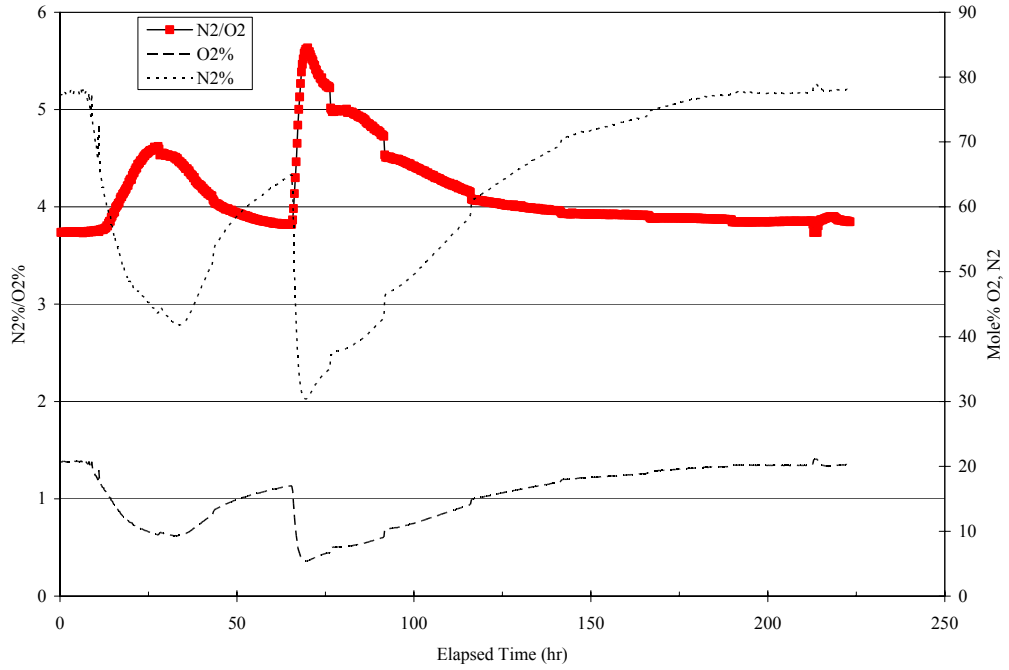

Figure 50. Nitrogen-to-oxygen ratio during Test 5 (75 °C, unmixed).

Test 6: 25 °C without Mixing

Figure 51 shows the composition of the gas exiting the Dissolution Vessel during Test 6. The sum of the measured gases is between 98 and 100% indicating almost all of the gas is identified. The CO_2 concentration starts at zero and increases to 13% after 25 hours. It remains approximately steady until the end of the test when it increases to 18%.

Figure 52 shows the hydrogen concentration during the test. Initially, no hydrogen was measured. After 125 hours, hydrogen is measured. The maximum concentration is 82 ppm.

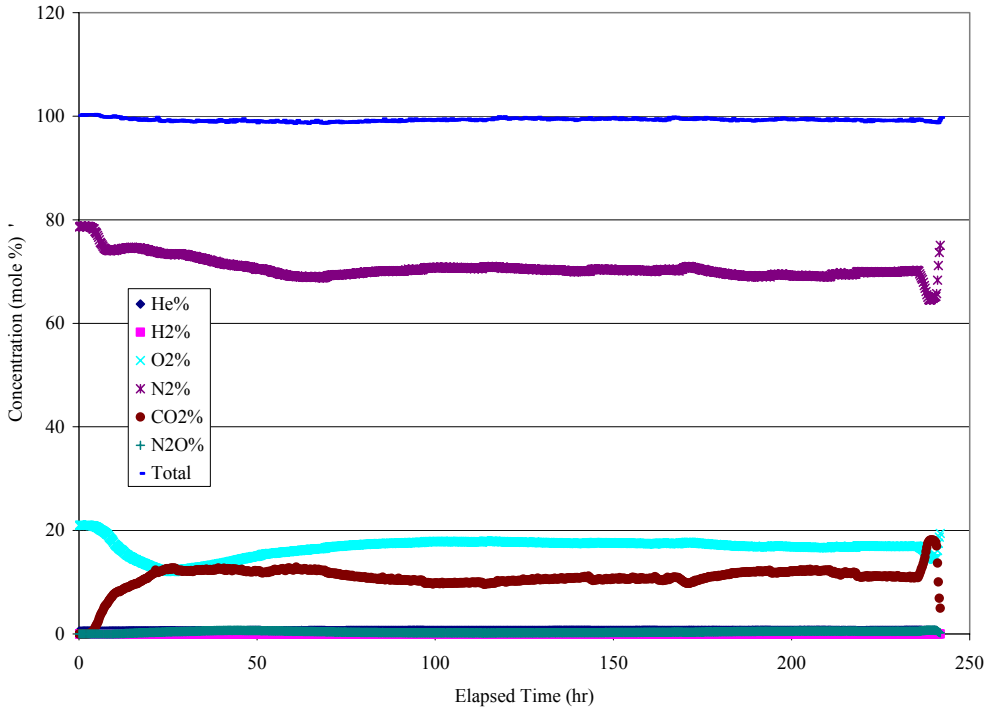

Figure 51. Composition of gas from Dissolution Vessel of Test 6 (25 °C, unmixed).

Figure 53 shows the N_2:O_2 ratio. The ratio starts at 3.8 and increases to 6.1 after 27 hours. The ratio decreases to ~ 4 where it remains until the end of the test when it increases to 4.5. The results are consistent with the gas composition data in Figure 51.

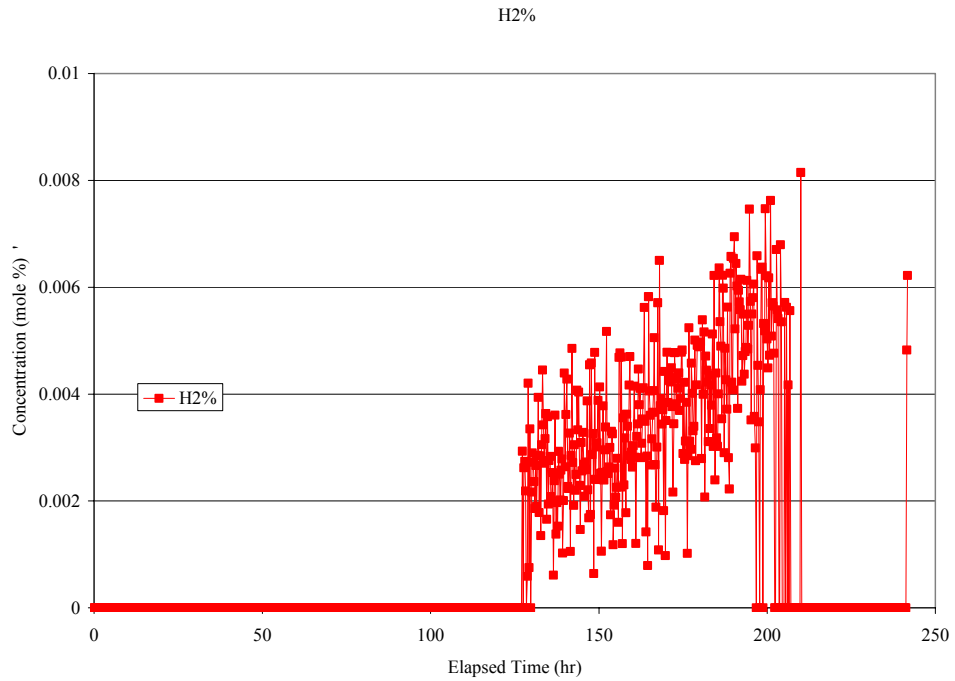

Figure 52. Hydrogen (mol %) in gas from Dissolution Vessel in Test 6 (25 °C, unmixed).

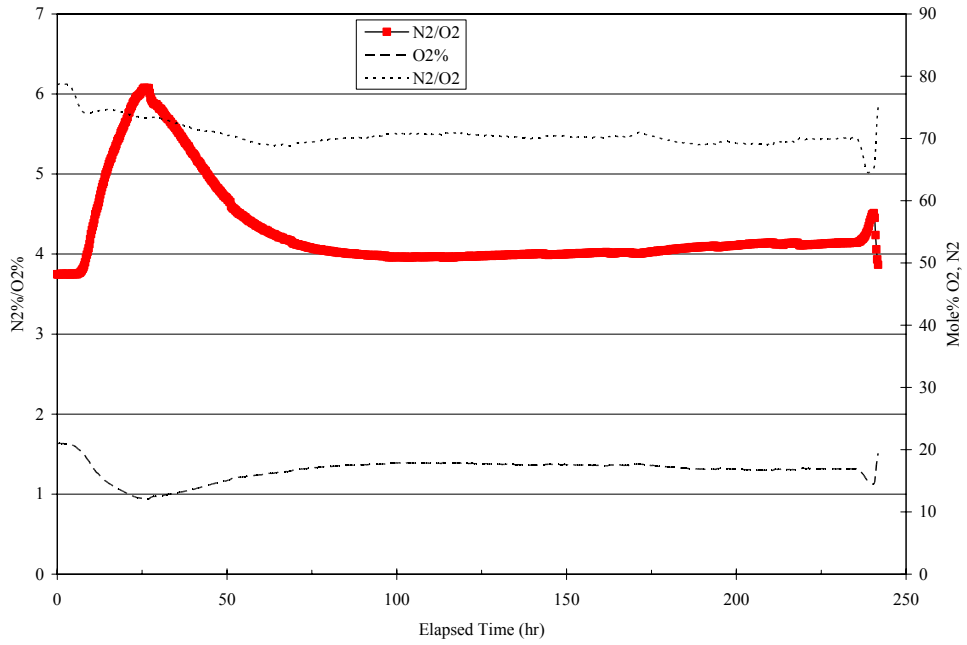

Figure 53. Nitrogen-to-oxygen ratio during Test 6 (25 °C, unmixed).

Gas Generation

Figure 54 and Table 16 show the amount of gas exiting from the Dissolution Vessel. In Table 16, the generation rates are the average rate over the duration of the experiments. The figure contains three lines. One line is the amount of gas exiting the vessel and being analyzed by the GC with no corrections. Equation 6 shows the calculation.

Gas (no correction) = [purge rate] equation 6

A second line shows the amount of gas exiting the vessel and being analyzed by the GC with a correction that accounts for the difference in the measured helium concentration versus the helium concentration in the purge gas (see equation 7).

Gas (He correction) = Gas (no correction) * [Purge gas He]/[Measured He equation 7

A third line shows the amount of gas exiting the vessel and being analyzed by the GC with a correction that accounts for the difference in the measured nitrogen concentration versus the nitrogen concentration in the purge gas (see equation 8).

Gas (N_2 correction) = Gas (no correction) * [Purge gas N_2]/[Measured N_2] equation 8

Since helium is inert and has a low concentration in air, decreases in the measured helium concentration would indicate increases in the amount of gas in the vessel or in-leakage of air to the vessel. Because the vessel was opened to add the sludge, the initial helium concentration is low. The nitrogen concentration provides another method to measures changes in the amount of gas in the vessel. Nitrogen is inert in this environment, so changes in the nitrogen concentration will indicate changes in the amount of gas in the system.

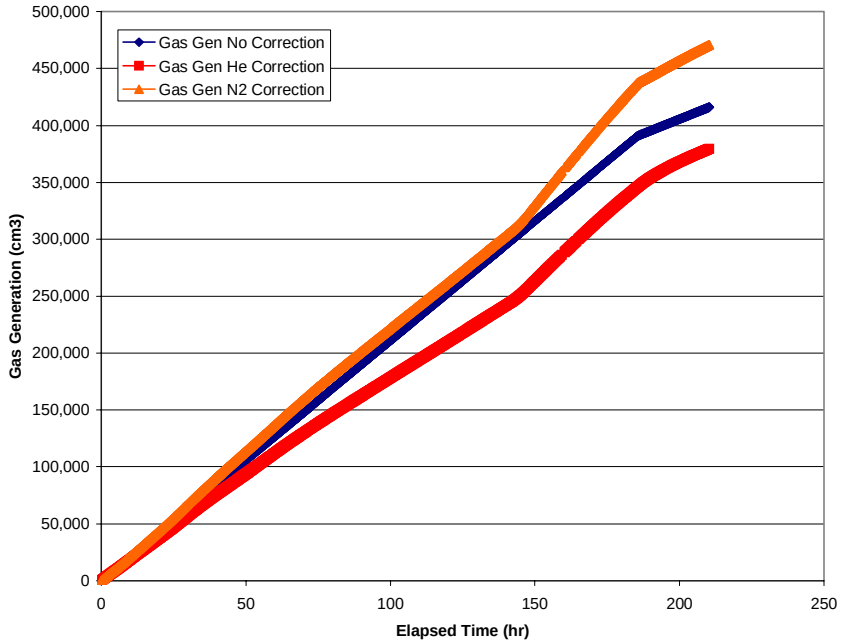

Figure 54. Cumulative gas volume from Dissolution Vessel in Test 1 (50 °C, mixed).

The helium correction shows a 36,000 cm^3 decrease in gas during the test (9%), while the nitrogen concentration shows a 55,000 cm^3 increase in gas (13%). Based on the GC detection limit, this demonstration generated less than 1.0 cm^3 of H_2 over the duration of the experiment.

Figure 55 and Table 17 show the gas generation measured during Test 2. The helium correction shows an 82,000 cm^3 increase in gas (33%), while the nitrogen correction shows an 87,000 cm^3 increase in gas (35%). Based on the GC detection limit, this demonstration generated less than 1.8 cm^3 of H_2 over the experiment.

Table 16. Gas generation during Test 1 (50 °C, mixed).

	Total Gas (cm^3)	**Gas Generated (cm^3)**	**Gas rate (cm^3/min)**	**Average Gas Generation (or Consumption) Rate (cm^3/min)**
Purge Gas	416,000		33.0	
Exit Gas – He correction	380,000	-36,000	30.1	-2.9
Exit Gas – N_2 correction	471,000	55,000	37.3	4.3

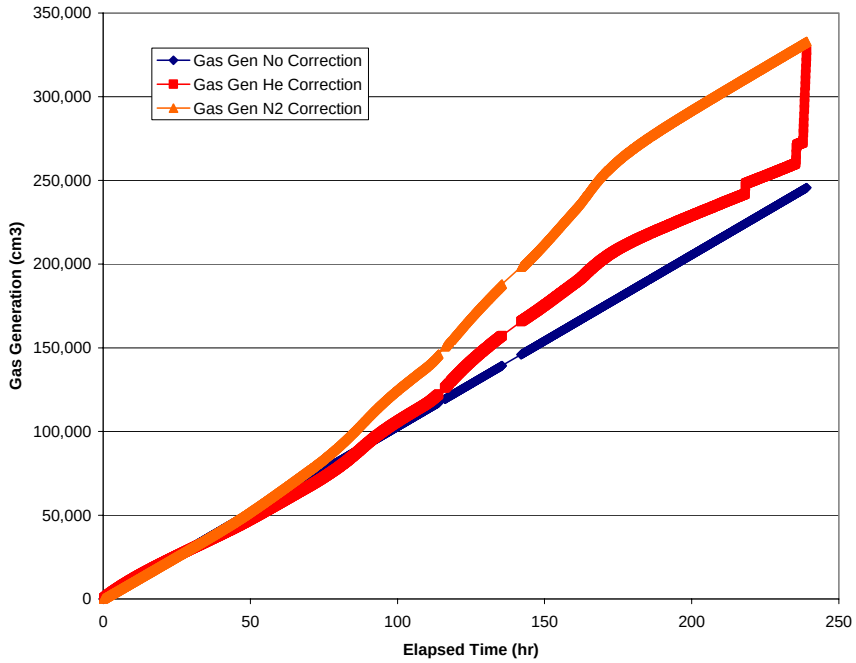

Figure 55. Cumulative gas volume from Dissolution Vessel in Test 2 (75 °C, mixed).

Table 17. Gas generation during Test 2 (75 °C, mixed).

	Total Gas (cm^3)	Gas Generated (cm^3)	Gas rate (cm^3/min)	Gas Gen Rate (cm^3/min)
Purge Gas	246,000		17.1	
Exit Gas – He correction	328,000	82,000	22.8	5.7
Exit Gas – N_2 correction	333,000	87,000	23.2	6.1

Figure 56 shows the gas generation during Test 3. The helium correction shows an increase of 21,000 cm^3 (6%), and the nitrogen correction shows an increase of 26,000 cm^3 (8%). Figure 57 shows the hydrogen generation during the test. The amount is very low (1.5 cm^3). On average, the hydrogen is ~0.0005% of the gas exiting the vessel and < 0.01% of the gas generated with a peak concentration of 0.004 vol % H_2 observed in the vapor space.

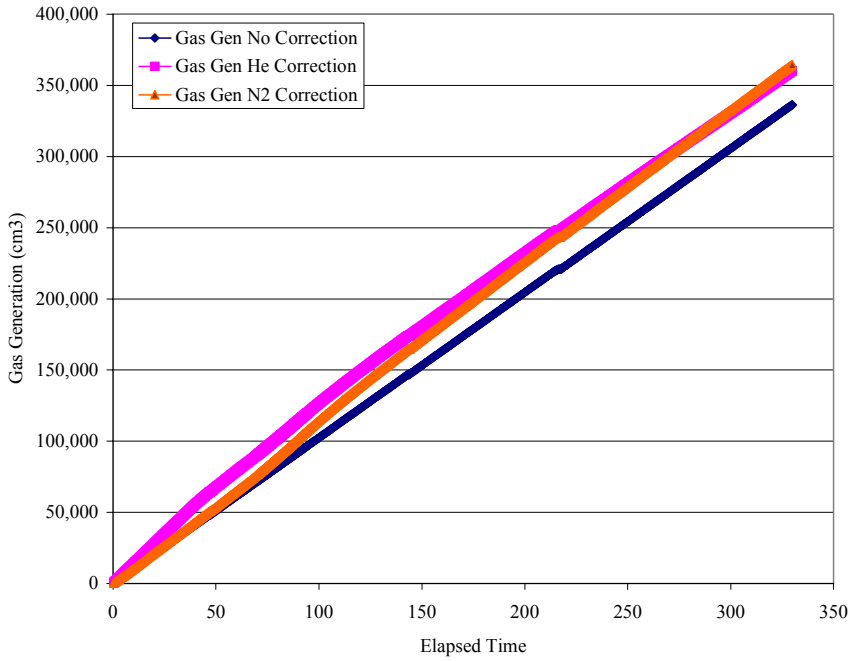

Figure 56. Cumulative gas volume from Dissolution Vessel in Test 3 (25 °C, mixed).

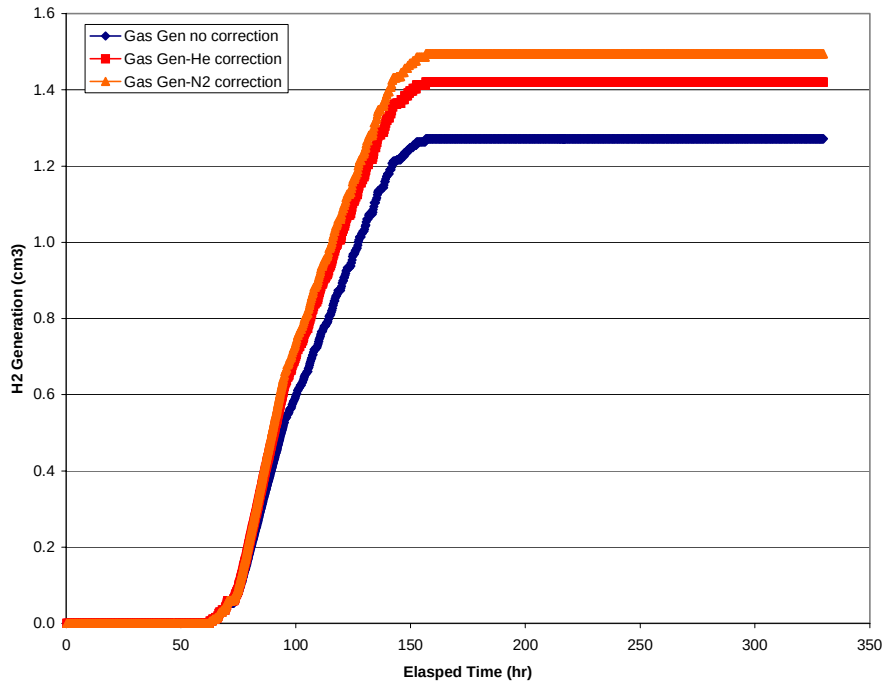

Figure 57. Cumulative hydrogen generation in Test 3 (25 °C, mixed).

Table 18. Gas generation during Test 3 (25 °C, mixed).

	Total Gas (cm^3)	Gas Generated (cm^3)	Gas rate (cm^3/min)	Gas Gen Rate (cm^3/min)	H_2 Generated (cm^3)
Purge Gas	339,000		17.1		1.3
Exit Gas – He correction	360,000	21,000	18.2	1.1	1.4
Exit Gas – N_2 correction	365,000	26,000	18.4	1.3	1.5

Figure 58 shows the gas generation during Test 4. The helium correction shows a 115,000 cm^3 increase in gas (33%). The nitrogen correction shows a 109,000 cm^3 increase in gas (32%). Figure 59 shows the hydrogen generation. Less than 10 cm^3 of hydrogen formed during the test with the average and peak hydrogen concentration during testing of 0.0014 vol % and 0.017 vol %, respectively.

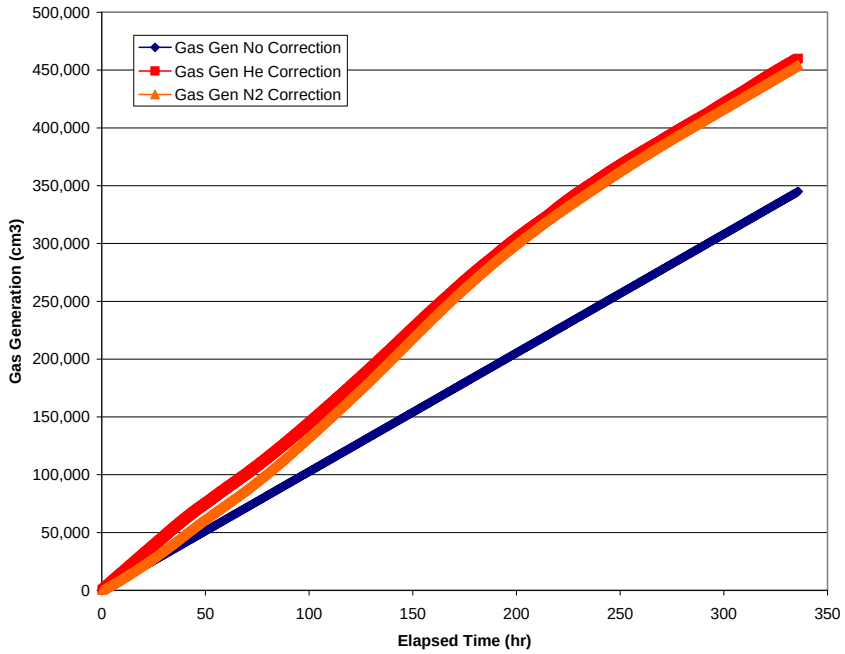

Figure 58. Cumulative gas volume from Dissolution Vessel in Test 4 (50 °C, unmixed).

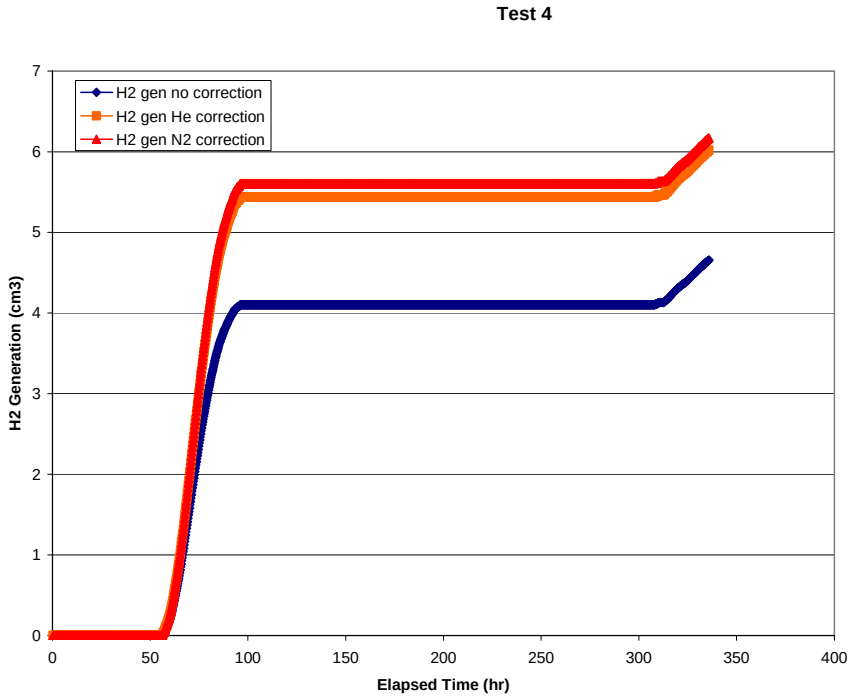

Figure 59. Cumulative hydrogen generation in Test 4 (50 °C, unmixed).

Table 19. Gas generation during Test 4 (50 °C, unmixed).

	Total Gas (cm^3)	Gas Generated (cm^3)	Gas rate (cm^3/min)	Gas Generation Rate (cm^3/min)	H_2 Generation (cm^3)
Purge Gas	345,000		17.1		4.7
Exit Gas – He correction	460,000	115,000	22.8	5.7	6.0
Exit Gas – N_2 correction	454,000	109,000	22.6	5.5	6.2

Figure 60 shows the gas generated during Test 5. The helium correction shows a 119,000 cm^3 increase (52%), and the nitrogen correction shows a 79,000 cm^3 increase (35%). The hydrogen generated (Figure 61) was less than 3 cm^3 with the average and peak hydrogen concentration observed during testing of 0.0011 vol % and 0.0080 vol %, respectively.

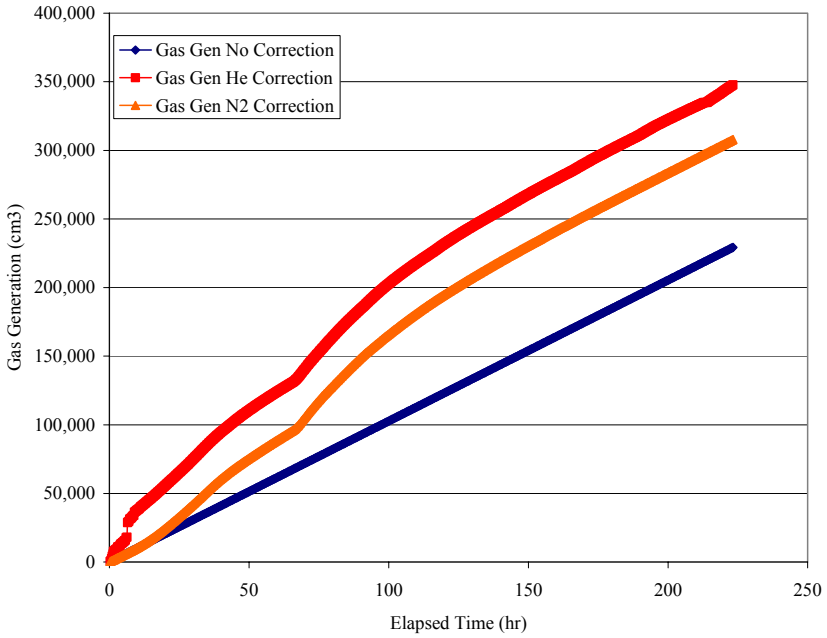

Figure 60. Cumulative gas volume from Dissolution Vessel of Test 5 (75 °C, unmixed).

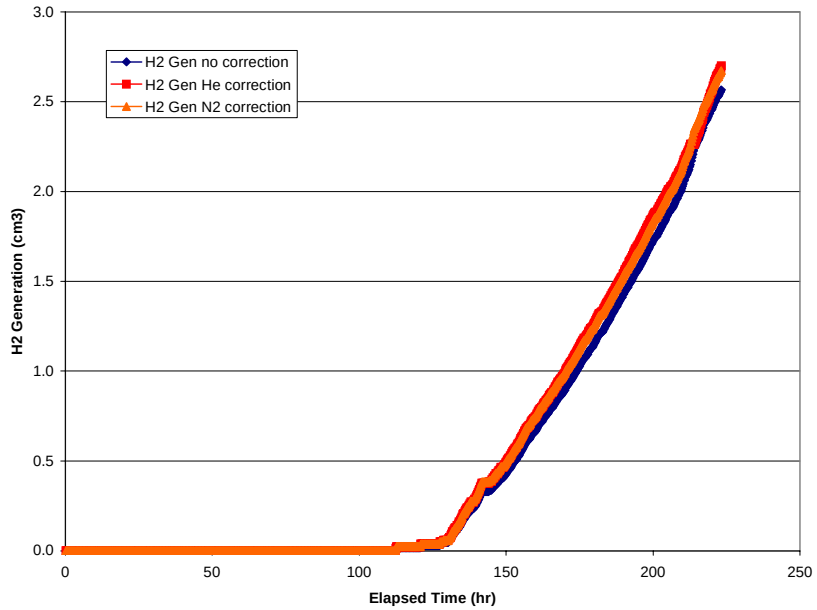

Figure 61. Cumulative hydrogen generation in Test 5 (75 °C, unmixed).

Table 20. Gas generation during Test 5 (75 °C, unmixed).

	Total Gas (cm^3)	Gas Generated (cm^3)	Gas Rate (cm^3/min)	Gas Generation Rate (cm^3/min)	H_2 Generation (cm^3)
Purge Gas	229,000		17.1		
Exit Gas – He correction	348,000	119,000	26.0	8.9	2.7
Exit Gas – N_2 correction	308,000	79,000	23.0	5.9	2.7

Figure 62 shows the gas generated during Test 6. The helium correction shows an additional 13,000 cm^3 of gas generated (5%). The nitrogen correction shows a 26,000 cm^3 increase (11%). Figure 63 shows the hydrogen generation. Hydrogen represented less than 4 cm^3 of the total gas generated with the average and peak hydrogen concentration observed during testing of 0.0012 vol % and 0.0081 vol %, respectively.

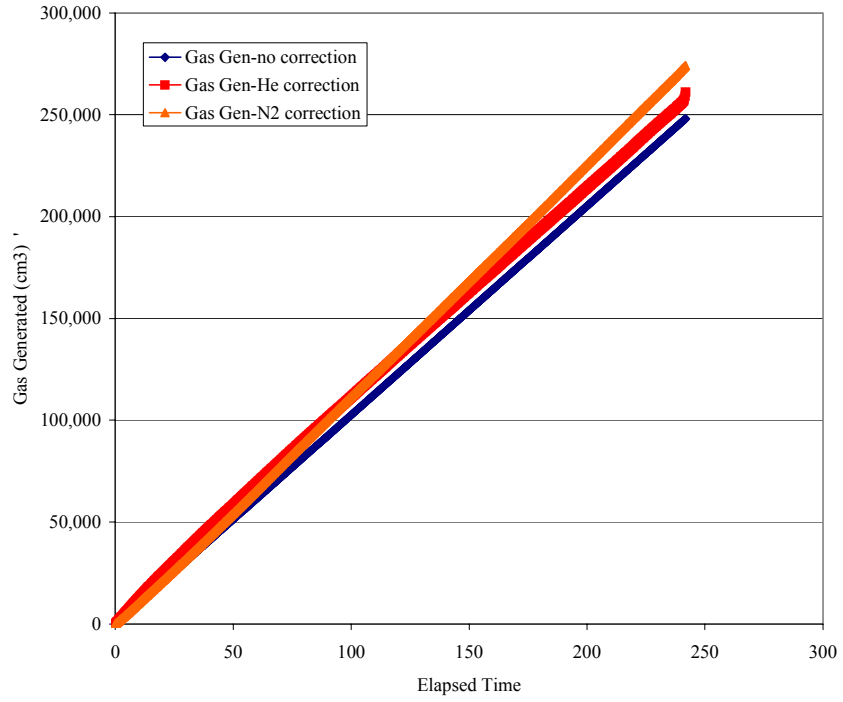

Figure 62. Cumulative gas volume from Dissolution Vessel in Test 6 (25 °C, unmixed).

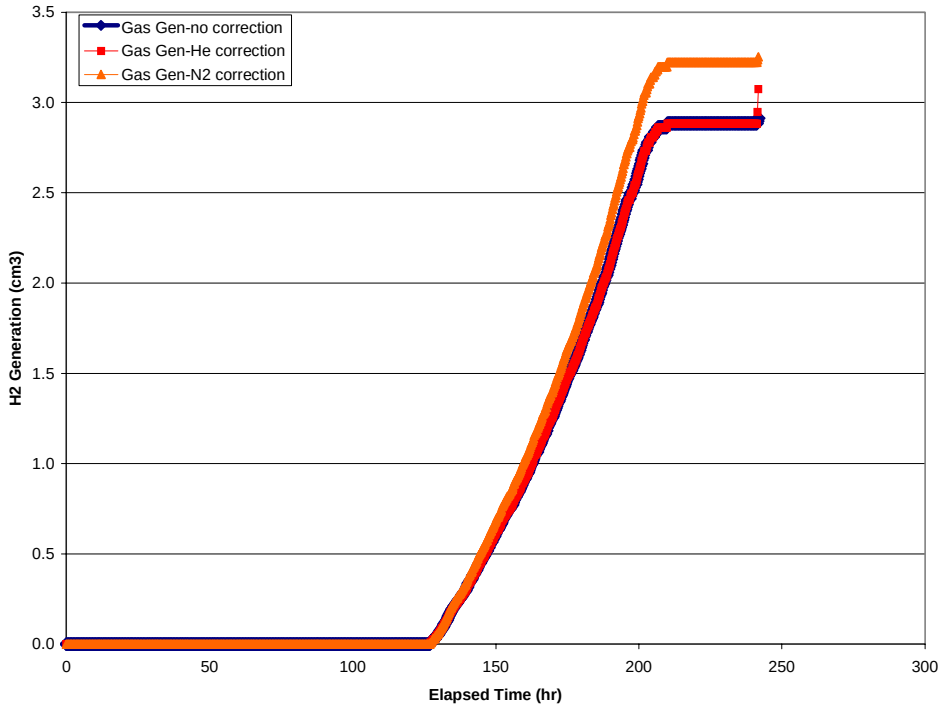

Figure 63. Cumulative hydrogen generation in Test 6 (25 °C, unmixed).

Table 21. Gas generation during Test 6 (25 °C, mixed).

	Total Gas (cm^3)	Gas Generated (cm^3)	Gas rate (cm^3/min)	Gas Gen Rate (cm^3/min)	H_2 Generation (cm^3)
Purge Gas	248,000		17.1		2.9
Exit Gas – He correction	261,000	13,000	18.0	0.9	3.1
Exit Gas – N_2 correction	274,000	26,000	18.9	1.8	3.3

Gas Sample Analyses

The first three tests used a GC that could not detect CO_2. Analyses showed a significant fraction of gas as unidentified. Also, the GC showed random presence of a trace amount of a low molecular weight (i.e., short retention time) component. In an attempt to identify the unknowns, personnel collected two vapor space samples during Tests 2, 3, and 4 and submitted for Volatile Organic Compound (VOC) by gas Chromatography / Mass Spectrometry (GC/MS). Table 22 shows these analytical results and the corresponding data from the in-line GC.

Table 22. Vapor space samples and "concurrent" Agilent GC (in blue) data.

Test Conditions	He	O_2	N_2	CO_2	N_2O	VOC, ppmv	Total
75 °C, mixed	N/A	22	76	5.2	N/A	11	114
75 °C, mixed	0.91	17.63	72.73	N/A	N/A	N/A	91
75 °C, mixed	N/A	21.00	78.00	< 0.1	N/A	1.30	100
75 °C, mixed	0.94	17.72	72.99	N/A	N/A	N/A	92
25 °C, mixed	N/A	20.00	70.00	6.40	N/A	N/A	96
25 °C, mixed	0.37	12.58	73.77	N/A	N/A	N/A	87
25 °C, mixed	N/A	20.00	75.00	< 0.1	N/A	11.00	106
25 °C, mixed	0.63	16.07	70.84	N/A	N/A	N/A	88
50 °C, unmixed	0.11	16.00	67.00	N/A	N/A	< 1.0	83
50 °C, unmixed	0.40	9.31	65.14	20.51	1.08	N/A	96
50 °C, unmixed	0.15	14.00	74.00	N/A	N/A	< 1.0	88
50 °C, unmixed	0.43	7.45	47.43	37.39	2.34	N/A	95

*No Hydrogen was found in the samples or by the on-line GC.

The detection limit was 0.1% (1000 ppmv) for all samples. No hydrogen was found in any of the samples or by the GC at the approximate time when of sample collection. Only toluene was found at the ppmv levels shown above. Toluene is not an expected gas during this evolution and is considered a residual contaminant on the GC column or on the gas bulbs used to obtain the vapor samples. Note that carbon dioxide was not detected in the 50 °C (unmixed) test sample. This is due to the CO_2 concentration exceeding the calibration range of the GC. Calibration was carried out prior to and after the sample analyses, as well as calibration verification using blank air. Samples were run in duplicate for confirmation of results. While the off-line GC is not quantitatively reliable, the data suggests the bulk of the unidentified gas in the first several tests was CO_2 with no other common flammable gases detected.

Identify of the randomly appearing constituent remains unknown. The analyses above and the additional separation column used in Tests 4-6 did not resolve the identity. The technical representative for the Agilent GC reviewed sample chromatograms and indicated the peak is likely an actual species of low weight. He speculated the species may be a NO_x compound.

Dissolution Efficiency and Kinetics

As expected the use of an agitator promoted uniform reaction kinetics among the various elements hence the smoother and more gradual lines for data obtained during Tests 1 – 3 versus the lines for Test 4 – 6 which were unstirred. However, it appears that between the 6^{th} and 7^{th} days for Tests 3 - 6 the solution in the Dissolution Vessel began to stabilize. This coincides with the same time frame between the 2-hr and 25-hr soak for Tests 1 and 2 indicating time and the amount of oxalic acid added to be deciding factors for stabilization independent of mixing. (See the Appendix for plots of the solution concentrations versus time.)

The uranium and aluminum concentrations for the mixed tests (Tests 1 – 3) exhibited similar behavior. With the exception of iron, all of the species seem to reach a stable concentration between the sixth and seventh day. This is believed to be due to the solution reaching

equilibrium and the elements reaching their respective solubility limits in the OA solution which had a final pH of 1.

The initial mass ratio of iron to uranium of the starting sludge was calculated to be 1.7. Below (Table 23) is a comparison between the Fe/U ratios measured for various solution samples for each test. (Note fewer analyses exist for the first two tests since the original experimental design only included three analyses for each experiment during the 50 hour soak period. After the first experiment, the authors realized from visual observations of the slurry that the sparse data set would prove insufficient and increased the frequency of sampling to daily.)

Table 23. Mass ratio of dissolved iron to uranium concentrations (mg/L).

50 °C mixed	75 °C mixed	25 °C mixed	50 °C unmixed	75 °C unmixed	25 °C unmixed
		0.472	0.051	0.001	0.003
	0.949	0.915	0.959	0.468	0.899
		0.949	0.578	0.576	0.903
	1.542	1.283	0.990	1.007	0.861
		1.384	1.417	1.094	0.813
	1.730	1.403	1.729	1.328	0.834
1.704	1.781	1.460	1.906	1.513	0.889
2.077	1.916	1.531	2.014	1.570	1.021
2.261	1.884	1.534	2.061	1.811	1.539
		1.650	2.101	1.854	1.727

Based on this data, the 25 °C tests exhibit iron to uranium (Fe/U) mass ratios less than 1.7 (i.e., the originally calculated ratio) indicating this temperature proved least effective for maintaining poison for uranium. The increasing ratios indicate uranium is dissolving at a faster rate than iron. Since uranium in solution is not a criticality concern the slower dissolution of iron is advantageous for this evolution.

The individual concentration trends for each of the tests follow. A composite graph for uranium dissolution (Figure 64) shows relative solution concentration at the end of each test. Additionally, a composite graph was made for iron (Figure 65) and manganese (Figure 66) since they are the poisons present in the simulated Tank 5F sludge. Data for nickel is shown as Figure 67. As depicted in Figure 64 the uranium concentration appears to level out at an approximate concentration of 3000 mg/L.

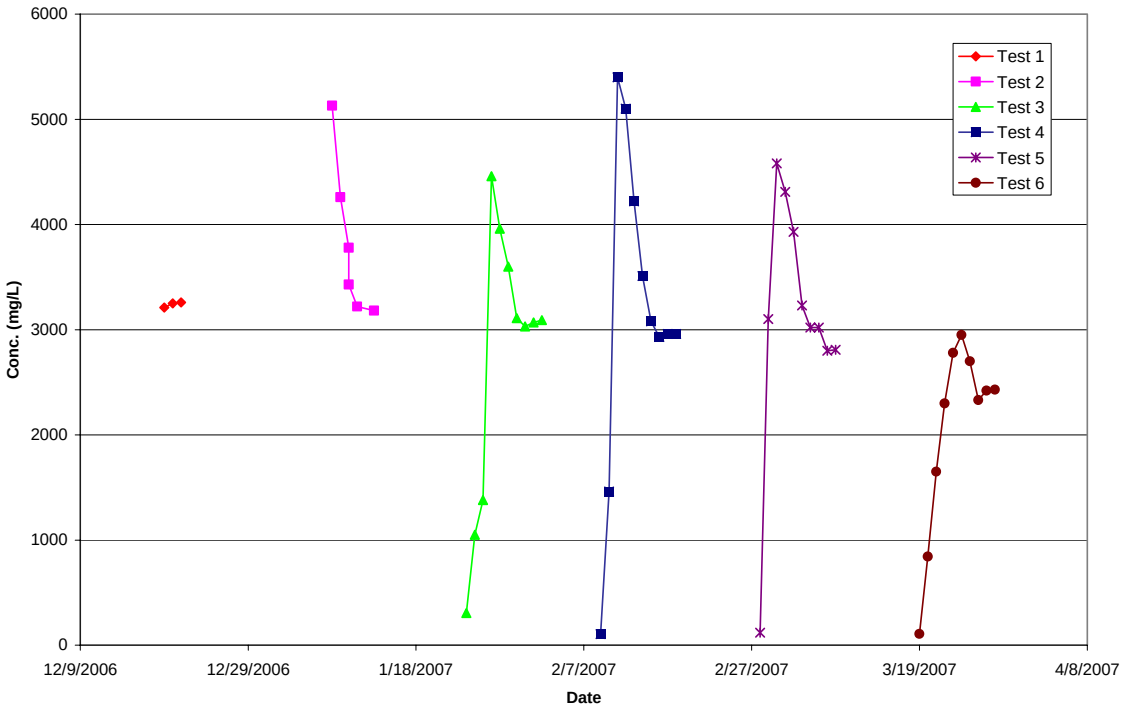

Figure 64. Uranium dissolution trend.

Material balances for elemental uranium, iron, and manganese, were performed to determine their chemical composition in the DU sludge, the amounts dissolved in the Dissolution Vessel during oxalic acid addition, and the amount precipitated in the caustic Tank 7F supernate simulant in the Receipt Vessel. From the material balance 190 g of simulant sludge were weighed out for each test and uranium makes up about 13% of the sludge. As shown in the following table, dissolution of uranium was greater than 98%. Note that the dissolution tables are calculated assuming no solids transferred to the Receipt Vessel and an identical starting sludge sample used in each test.

Table 24. Uranium dissolution.

Test	Initial U-238 in Test (g)	Dissolved U-238 (g)	% Dissolved U-238	U-238 Xferred to V1 / PPT in V2 (g)
Test 1 (50 ^{o}C w/ mixing)	25.08	25.02	99.76	9.04
Test 2 (75 ^{o}C w/ mixing)	25.08	24.81	98.92	5.73
Test 3 (25 ^{o}C w/ mixing)	25.08	24.98	99.60	5.76
Test 4 (50 ^{o}C w/o mixing)	25.08	24.92	99.38	5.75
Test 5 (75 ^{o}C w/o mixing)	25.08	24.76	98.72	8.95
Test 6 (25 ^{o}C w/o mixing)	25.08	24.87	99.17	5.74

It will be assumed that all solution transferred from the acidic contents of the Dissolution Vessel to the caustic the Receipt Vessel will be precipitated out in the Receipt Vessel. According to this assumption the greatest amount of precipitate occurred during Test 1.

Iron, which makes up approximately 20% of the simulated sludge and one of the main poisons for the uranium present in the sludge, appears to dissolve as well as uranium in the 8 wt % oxalic acid solution yielding dissolution greater than 93% as shown in the table below. Theses values are calculated from comparing the concentration of dissolved iron to the starting concentration in the sludge with no correction for the added iron from corrosion of the metal coupons. Hence, dissolution efficiency values based on iron in this table are likely biased high.

Table 25. Iron dissolution.

Test	Initial Fe in Test (g)	Dissolved Fe (g)	% Fe Dissolved	Fe Xferred to V1 / PPT in V2 (g)
Test 1 (50 ^{o}C w/ mixing)	39.33	39.04	99.26	14.11
Test 2 (75 ^{o}C w/ mixing)	39.33	36.81	93.59	8.49
Test 3 (25 ^{o}C w/ mixing)	39.33	39.11	99.44	9.02
Test 4 (50 ^{o}C wo/ mixing)	39.33	37.58	95.55	8.67
Test 5 (75 ^{o}C w/o mixing)	39.33	38.66	98.30	13.97
Test 6 (25 ^{o}C w/o mixing)	39.33	39.27	99.86	9.06

However based on the composite trend below the endpoint concentrations for iron do not have a constant endpoint like that of uranium. The last few data points on the individual curves show an increase in the iron concentration. We believe at this point all the other species have reached their solubility limits in oxalic acid or have all been dissolved (as demonstrated in the figure for uranium) and the increase in additional iron anions is due to the corrosion of the coupons in the liquid.

Manganese, another poison for the sludge, makes up 6% of the sludge. Based on the data in the table, the amount of manganese dissolved ranged from a low of about 23% to a high of about 57%. For Test 6, the overall mass material balance proved less reliable with a notable discrepancy for manganese.

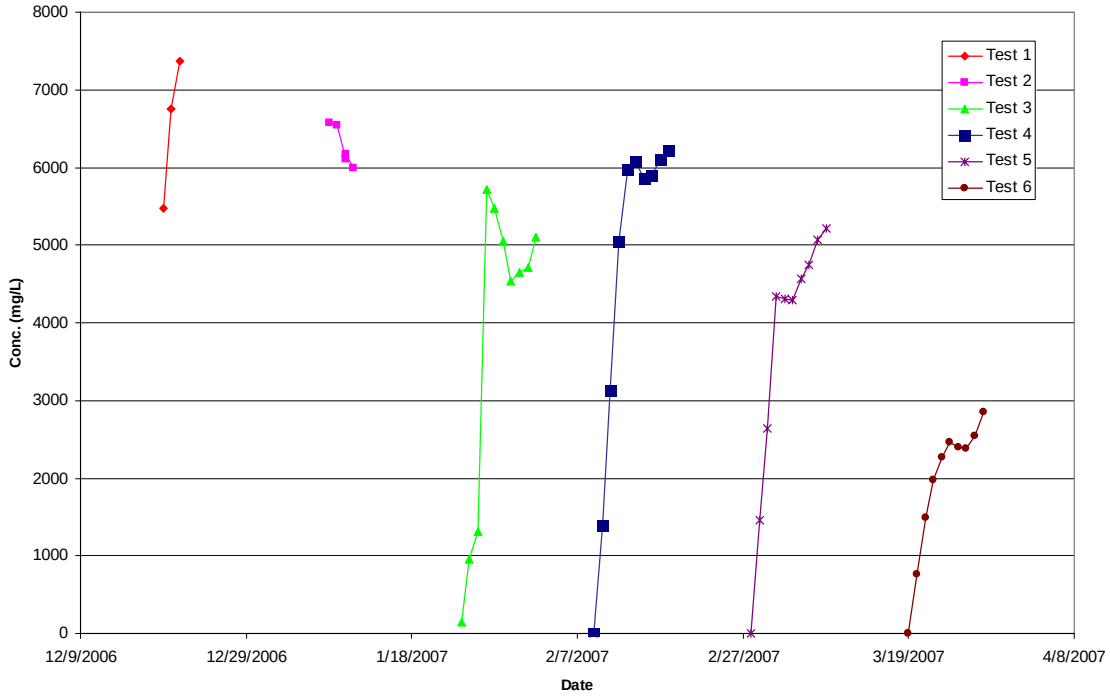

Figure 65. Iron dissolution trend.

Table 26. Manganese dissolution.

Test	Initial Mn in Test (g)	Dissolved Mn (g)	% Mn Dissolved	Mn Xferred to V1 / PPT in V2 (g)
Test 1 (50 °C w/ mixing)	11.19	4.84	43.21	1.75
Test 2 (75 °C w/ mixing)	11.19	2.66	23.76	0.61
Test 3 (25 °C w/ mixing)	11.19	3.60	32.19	0.83
Test 4 (50 °C w/o mixing)	11.19	3.67	32.83	0.85
Test 5 (75 °C w/o mixing)	11.19	4.10	36.64	1.48
Test 6 (25 °C w/o mixing)	11.19	6.41	57.25	1.48

The composite trend for manganese shows a variance in the final Mn concentration in solution with temperature conditions. For example, Test 2 and Test 4 which are both performed at 75 °C both appear to have an ending concentration of about 450 mg/L, whereas the final Mn concentrations is nearer 300 mg/L for experiments at 25 °C (i.e., Tests 3 and 6). Since it was apparent by the previous table that not all of the manganese was dissolved as in the case for uranium, it is believed that this behavior is due to the solubility of manganese being a function of temperature.

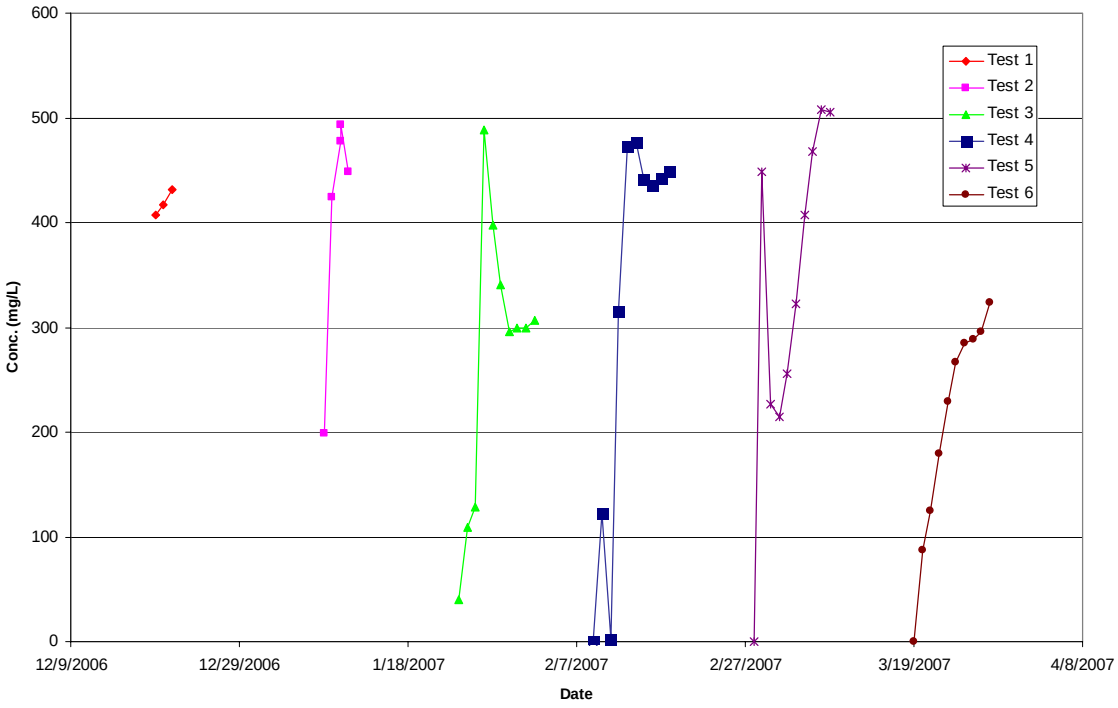

Figure 66. Manganese dissolution trend.

Nickel, the third neutron poison also makes up 6% of the sludge. From the following composite trend it is apparent that nickel (with the exception of 3 outliers) does not exceed a concentration of 50 mg/L.

From the dissolution data it can also be seen that nickel is the least soluble of the three poisons resulting in a maximum dissolution of 37% in the 8 wt % oxalic acid solution.

Analysis of Solids

The solids remaining from the Dissolution Vessel and the Receipt Vessel were digested by aqua regia and analyzed by ICP-ES for RCRA metals (Ag, Ba, Cd, Cr, and Pb) for disposal purposes and Al, Fe, Mn, Ni, and U for determining material balances. Additionally U concentration was determined by ICP-MS since the emission peak given off using ICP-ES for this particular element overlaps emission peaks and interferes with the detection of other desired elements. Material balances were completed for U, Fe, Mn, and Ni to track the extent of dissolution of these elements in the Dissolution Vessel and the precipitation subsequent to transferring into the Receipt Vessel.

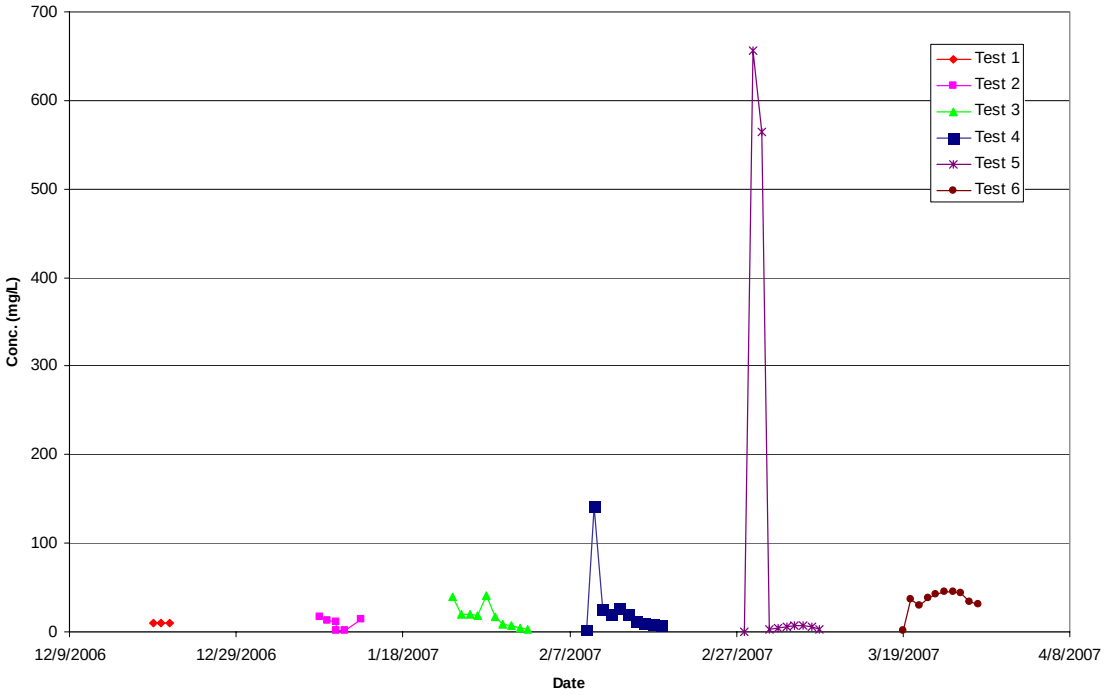

Figure 67. Nickel dissolution trend.

Table 27. Nickel dissolution.

Test	Initial Ni in Test (g)	Dissolved Ni (g)	% Ni Dissolved	Ni Xferred to V1 / PPT in V2 (g)
Test 1 (50 ^{o}C w/ mixing)	11.21	2.24	19.99	0.81
Test 2 (75 ^{o}C w/ mixing)	11.21	1.06	9.48	0.25
Test 3 (25 ^{o}C w/ mixing)	11.21	0.97	8.63	0.22
Test 4 (50 ^{o}C w/o mixing)	11.21	0.20	1.79	0.05
Test 5 (75 ^{o}C w/o mixing)	11.21	0.10	0.88	0.04
Test 6 (25 ^{o}C w/o mixing)	11.21	4.17	37.19	0.96

FT-Raman Analysis

Personnel located and calibrated a Kaiser Optics spectrometer that utilizes a Holospec filter units in conjunction with a CCD (Charge Coupled Device) for detection. Personnel aimed a 0.5 mm diameter size laser spot (785 nm wavelength) on the glass vessel. Personnel moved the laser focal spot past the glass vessel by monitoring the Raman signature to ensure the signal from the glass container is not observed and the signal from the sludge was observed. Each signal is the combined sum of 30 scans and each scan the detector was exposed to the Raman signal for 5 seconds.

SEM-EDS Analysis

Personnel collected solids from the oxalic acid (8 wt %) Dissolution Vessel and solids from the caustic Receipt Vessel of the oxalic acid leached solution. The solids were air dried and then, using a double-sided sticky tape mounted on a stage, the tape was pressed against the sample and some of the sample attached to the tape. The stage was placed in a vacuum chamber. The sample was coated with a thin carbon (a few nanometers) layer to minimize static charge.

The sample was then introduced into the vacuum chamber of the SEM instrument and illuminated with a narrow beam of electrons (diameter can be adjusted from a few millimeters to a few microns). The sample emits electrons (secondary and back scattered) which are detected by a detector that determines their kinetic energy and from this data a topographical image is made of the sample. The sample also emits X-rays whose wavelengths are characteristic of the element from which the X-rays originate. This allows the analyst to determine the elemental composition of the sample spot being interrogated (Energy Dispersed Spectroscopy or EDS). Therefore, the technique provides a topographical image as well as a elemental composition of the area being image. Please note the peaks (counts) in the EDS spectrum are only proportional to the amount of that element. The peak ratio (either peak area or height) between elements is proportional to the elemental ratio. This fact is used in this study to estimate the ratio of neutron poisons (such as iron and manganese) to uranium (to represent fissile material) for the solids remaining during the oxalic acid leaching and from the solids obtained during caustic neutralization of the oxalic acid leached Tank 5F sludge.

"As Made" Tank 5F Simulant Sludge

Personnel submitted portions of the "As Made" Tank 5F simulant sludge for elemental analysis spatial distribution (i.e., EDS image). Figure 68 shows a backscattered image of a grain from the simulant sludge. Bright areas are indication of electron enriched elements while dark areas are indication of element with lesser amount of electrons. Inspection of Figure 68 indicates that the "As Made" Tank 5F simulant sludge is a heterogeneous mixture of particles embedded in a nearly uniform matrix. Some particles are enriched with uranium while others are enriched with silicon. The majority of the bulk material is composed of iron with minor traces of manganese, nickel, uranium, calcium and barium.

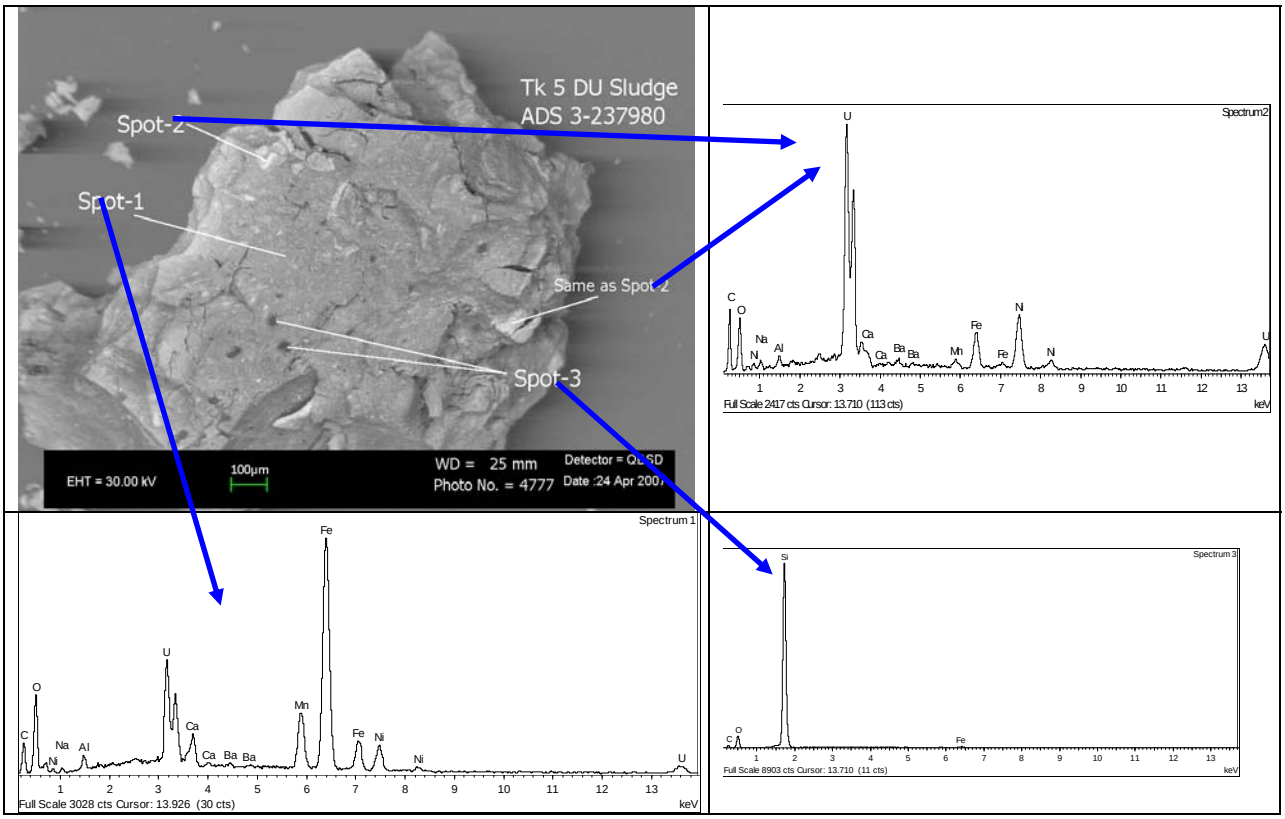

Figure 68. Backscattered electron image of a grain from the "As Made" Tank 5F simulant sludge and elemental composition for selective locations.

Residues from Leaching Tank 5F Simulant Sludge with 8 wt % Oxalic Acid

At the end of the oxalic acid addition to the Tank 5F sludge, a layer of whites solids with a slight blue color remained at the bottom of the glass (borosilicate glass (DOW 7740) containing silicon, aluminum, boron and sodium). A laser (785 nm) was focused on the solids and the Raman spectrometer detected two different spectra. Figure 69 shows a picture of the solids remaining in the glass vessel and the two Raman spectra for those solids. The Raman spectra indicate the presence of sodium oxalate, iron oxalate and iron hydroxide. (Note that Fe and Mn oxalates are not easily discriminated by the Raman analysis. Hence, the reported iron oxalates may include Mn oxide. The same analytical limitation exists for the respective oxides.) In the same figure, the XRD (X-Ray Diffraction) indicates the presence of calcium oxalate. The products are consistent with the low solubility of iron and calcium in oxalic acid. The presence of sodium oxalate is due to the large concentration of sodium that exceeds the sodium solubility in oxalic acid. Temperature (25 °C to 75 °C) and mixing (no mixing) had no effect on the residues compositions. The data shown in Figure 69 is representative of the data obtained from residues seen in experiments with variable temperature and mixing. Also shown is the spectrum of an organic material (as noted by the peaks at 2830-2880 cm^{-1}) present in the residue. During the testing personnel noticed plastic debris originating from a plastic ring surrounding the rotating shaft falling on the contents of the vessel. We believe the FT-Raman detected this plastic debris in the residue.

Residues from Caustic Neutralization of Spent Acid

A large portion of the oxalic acid leached Tank 5F simulant sludge was added to a caustic salt simulant (1.8M [OH]) to drop out the metals and actinides. The addition involved no mixing and therefore, the rate of neutralization and settling was controlled by mass diffusion, particle nucleation, growth and settling. Dual color layers (one brown and the other light brown) formed at the bottom of the vessel. Figure 70 shows the XRD and FT-Raman data of the residues obtained from neutralizing leached Tank 5F simulant sludge slurry. The XRD indicates the presence of natroxalate ($Na_2C_2O_4$) and sodium uranyl carbonate ($NaUO_2C_2O4$). (Recall that air drying and vacuum does not transform amorphous materials into crystalline forms.) The FT-Raman indicates the presence of mostly sodium oxalate in the "light" brown layer while sodium oxalate and uranyl oxalate were detected in the "dark" brown layer. All identified compounds are consistent with neutralizing an acidic solution, however, both XRD and FT-Raman failed to detect the iron, manganese and nickel oxide (or hydroxides). The lack of diffraction lines attributable to iron, manganese, or nickel suggest that these compounds are amorphous, which is common for metals precipitated under the conditions used in this testing, and their molecular vibrations may be too polar (ideal for FT-IR) for the Raman to detect.

Spatial Distribution of the Elements in Dissolution Vessel Solids

A small portion of the residues obtained from the oxalic acid leaching of Tank 5F simulated sludge was analyzed by SEM and EDS. Recall that SEM provides topographical and chemical imaging. The EDS provides spot size (micron size) elemental composition of topographical features found in the SEM scan. For clarity, only the spectra of iron, manganese, and uranium are shown. Figure 71 (75 °C, no mixing experiment) shows the SEM images and corresponding EDS of selective areas in the SEM image. The SEM shows an array of particles of different sizes and shapes. In particular, there are cylindrical particles with an EDS analysis indicating particles are enriched in uranium (Spots 4 and 5) and depleted in iron. This is an indication of mostly uranium crystals with iron impurities. The brightness of these particles relative to the remaining features is an indication that the particles are composed of an electron rich element consistent with uranium. This is evidence of separation between uranium and iron atoms at the micron level. However, the starting material also shows regions (Figure 68) with high concentrations of uranium with little fissile poison (e.g., iron). Since one would not expect the oxalic acid dissolution conditions to effectively dissolve these materials. When an EDS analysis is done on 1 x 1 mm^2 area the iron to uranium ratio is very large. Magnification to the micron level (10 microns) indicates a physical separation between some uranium and iron particles. Fortunately, the amount of uranium remaining in the residues is small since a large quantity of uranium dissolved in the oxalic acid leaching. Spot 3 contains mostly Ag and Cl. Spot 6 is composed of Ca, Ce, Pr, La, Mn, and Ni. Finally, Spot 7 is composed of mostly Ca with traces of Mn and Ni.

.

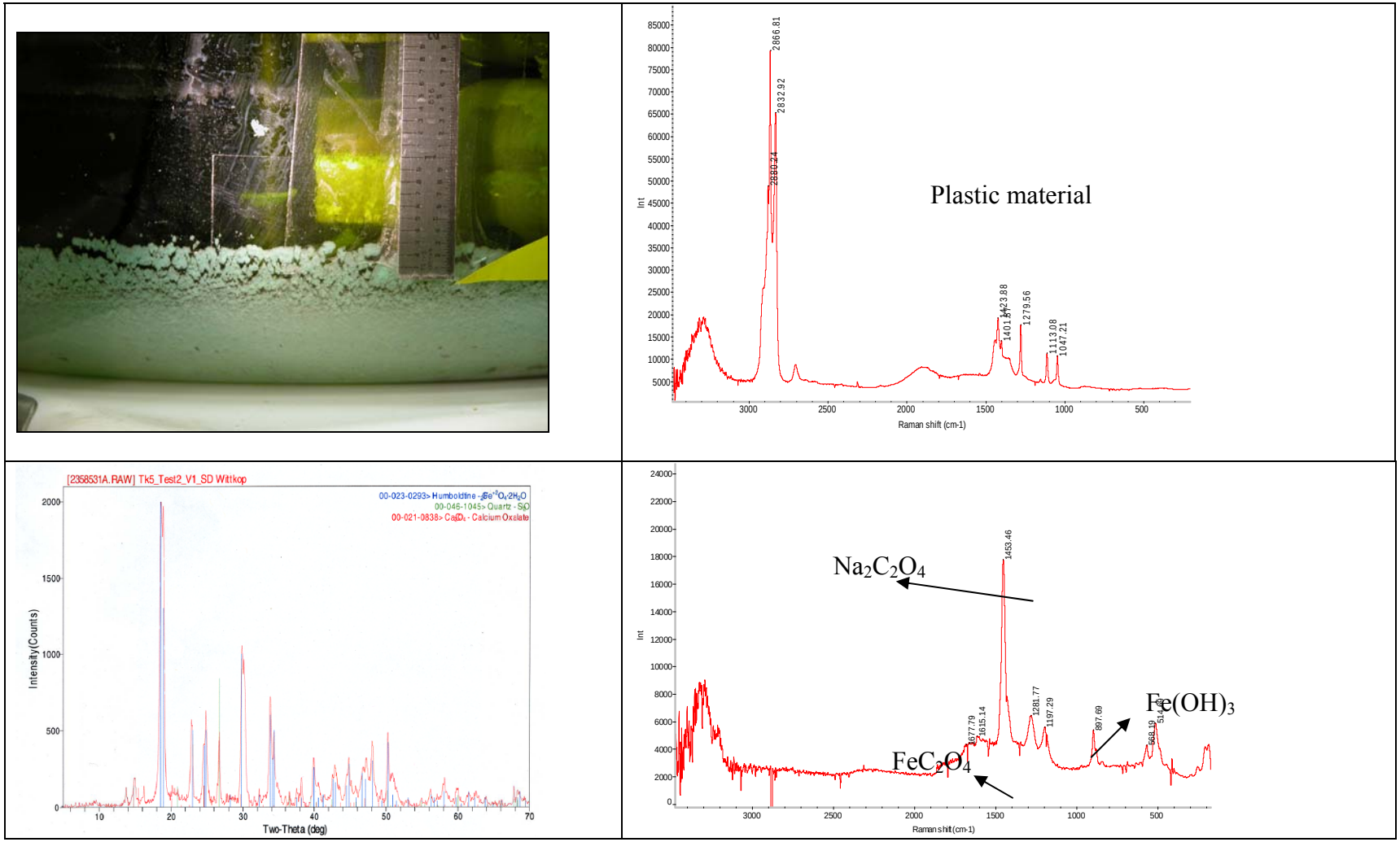

Figure 69. XRD and FT-Raman of solids from Dissolution Vessel (75 °C, mixed).

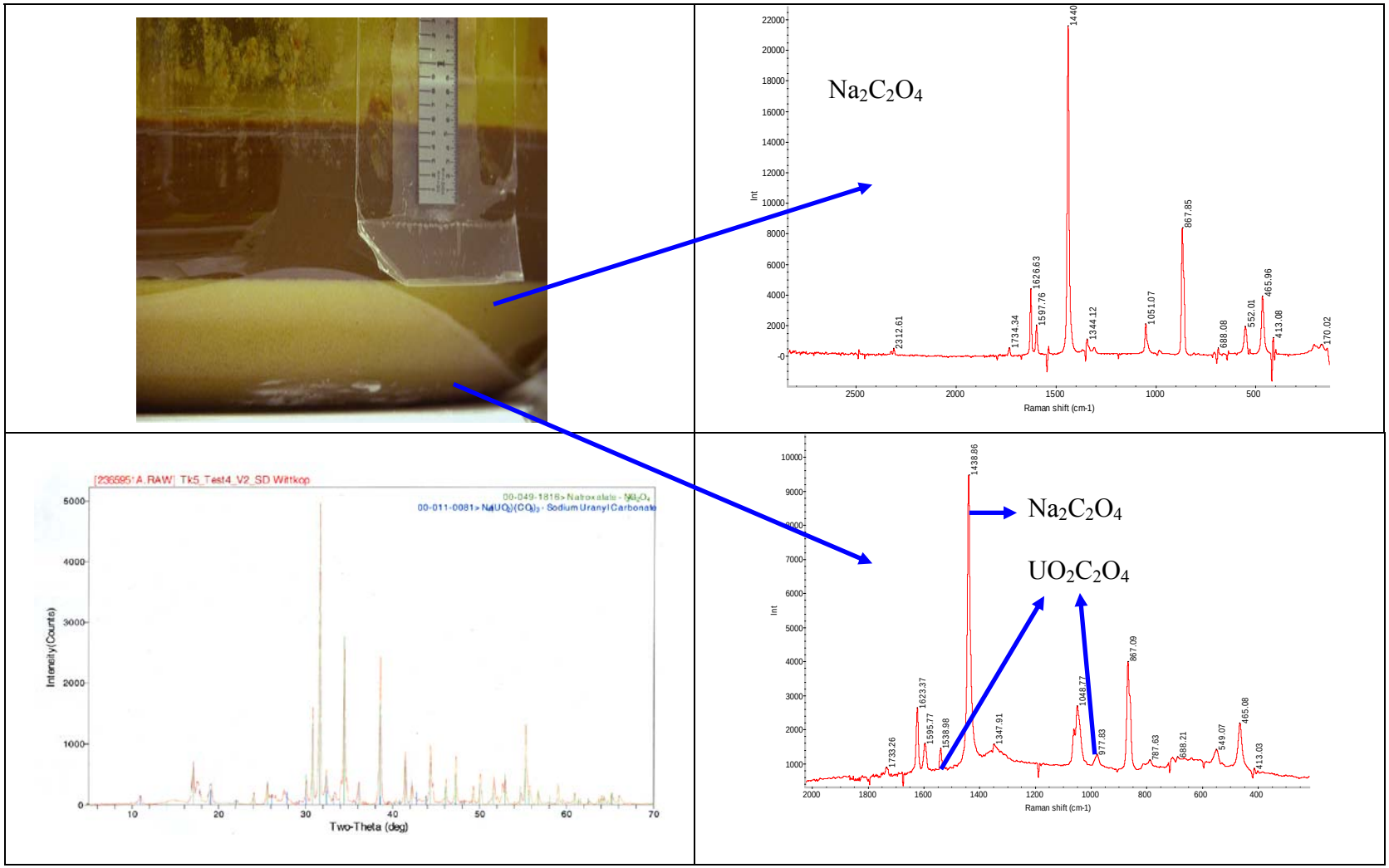

Figure 70. XRD and FT-Raman of the different solids from Receipt Vessel (50 °C, unmixed).

No uranium phase was found in the solids remaining in the OA leaching of Tank 5F sludge conducted at 25 °C with no mixing. Elements found included Mn, Ni, Si, Al, Ba, Ca and Ag. Recall that the remaining residues are insoluble in oxalic acid and the residue is expected to be heterogeneous. Heterogeneity impacts sampling. Depending on the sampling method, different answers may be obtained.

Effect of Temperature and Mixing on the Elemental Spatial Distribution of Receipt Vessel Solids

Figure 72 and Figure 73 show the effect of temperature (75 °C vs. 25 °C, respectively) and mixing on the spatial distribution of elements as determined from EDS. Inspection of the figures shows particles abundant in uranium with less iron. If the data can be generalized, increasing temperature and adding mixing appears to increase the size of the uranium enriched particles in the residue (from 10 microns to several hundred microns). Large particles will settle faster than smaller ones given the same density, and the increase in the uranium enriched particles may lead to layered settling. In addition, mixing may aggregate these particles into small regions creating a undesirable geometrical concentration. In Figure 72, Spot 1 – spectra not shown – contains Fe, Na, and traces of Mn, U, Ca and Al. In Figure 73, Spot 2 – spectra not shown – contains mostly Na with traces of F.

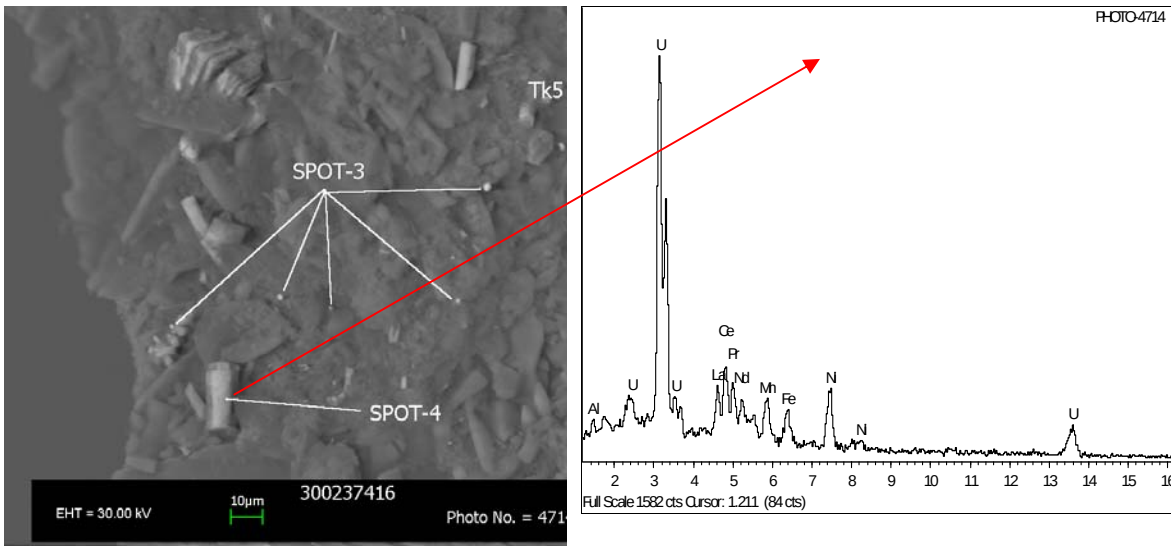

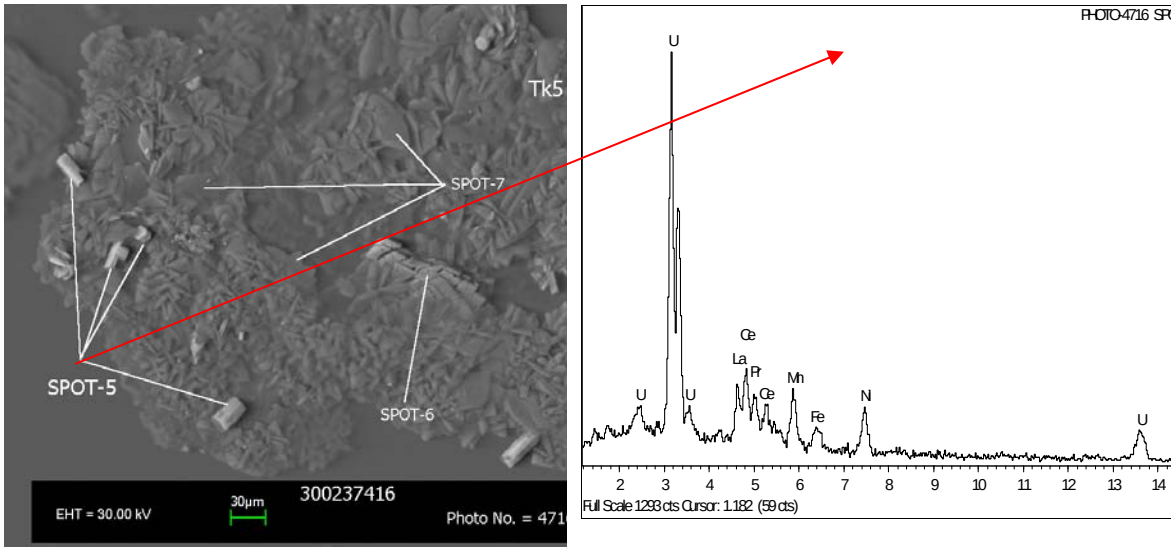

Figure 71. Precipitates remaining from the oxalic acid leaching of simulated Tank 5F sludge at 75 °C with no mixing.

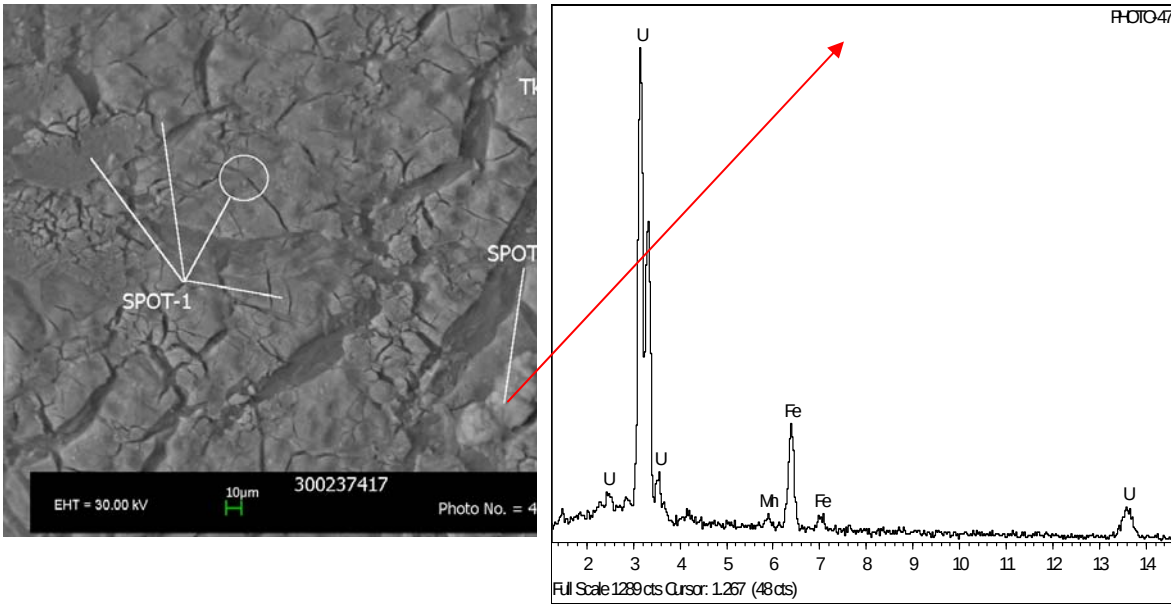

Figure 72 Solids from the precipitation in caustic solution (1.81 M [OH]) from the 75 °C oxalic acid leaching of simulated Tank 5F sludge with no mixing.

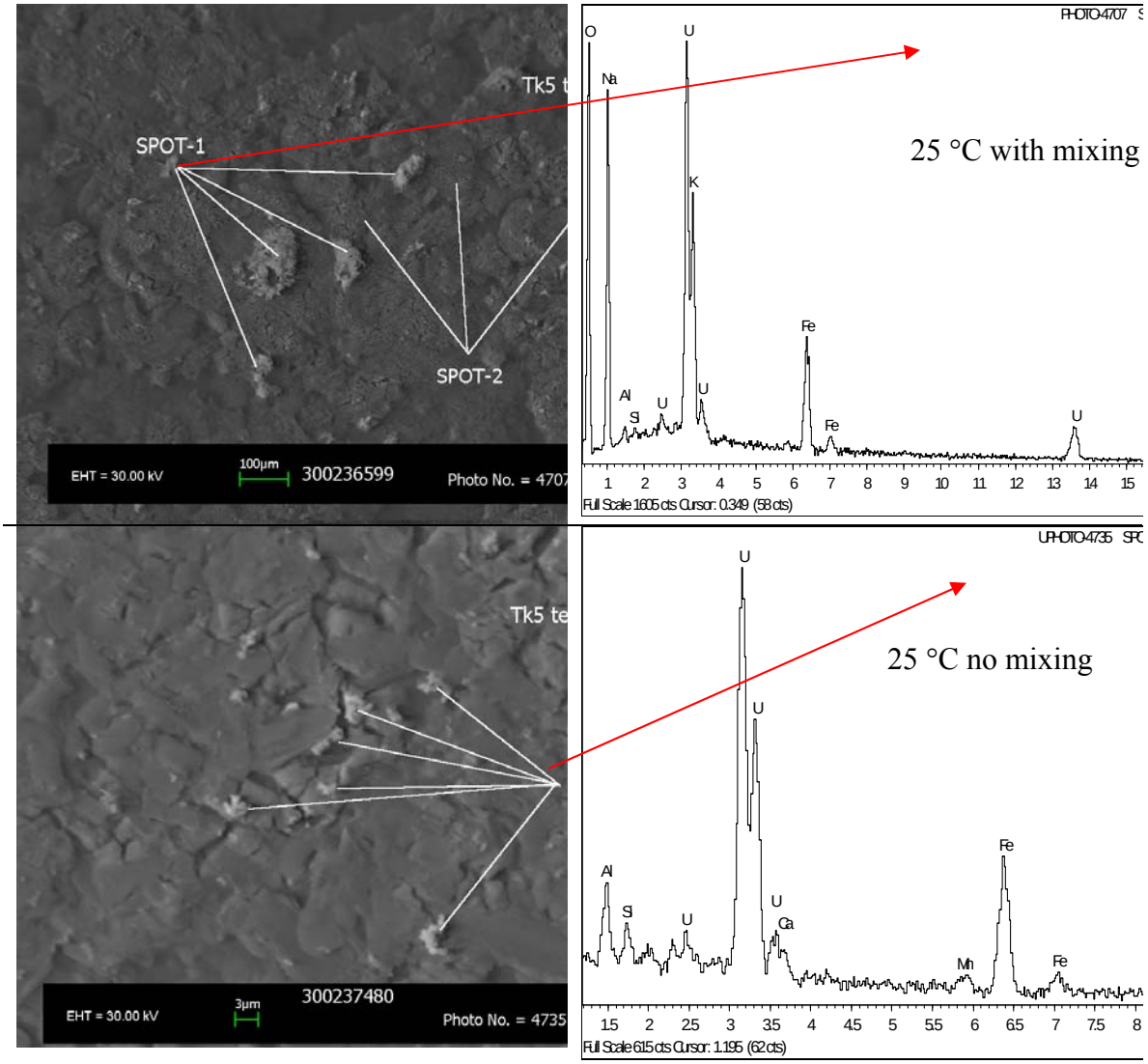

Figure 73 Solids from the precipitation in caustic solution (1.81 M [OH]) of the oxalic acid leaching of simulated Tank 5F sludge at 25 °C with no mixing.

Areal Density of Particles Enriched with Uranium

The images from Figure 68, Figure 71 and Figure 72 were analyzed for the surface area occupied by the particles enriched with uranium relative to the remaining material. Table 28 contains the percentage of are assigned to uranium for each. Assuming the spatial distribution of particle and their corresponding elemental compositions are representative of the "As Made" synthetic sludge and the residues from the Dissolution Vessel and 2, inspection of Table 28 indicates that fraction of particles enriched with uranium is small.

Table 28. Areal density of particles enriched with uranium from EDS images.

Sample Image	% of Surface Area as Uranium
"As Made" Tank 25F Sludge (Figure 68)	0.15
Residue from OA leaching at 75 °C without mixing (Figure 71)	1.61, 2.31
Residues from Caustic Precipitation of the Dissolution Vessel solution (OA leached at 25 °C without mixing) (Figure 72)	1.48, 1.78

Results of In-situ Monitoring of Corrosion Coupons

These experiments examined whether hydrogen generation is thermodynamically favorable and, if favorable, the rate of formation. The E_{corr} measurements investigated the thermodynamics, while the LPR measurements addressed the kinetics issue. The tests also explored the effect of material (e.g., surface condition of coupon) and environmental (e.g., temperature and mixing) variables. Recall, the experiments used four containers simultaneously: two located inside the irradiation cell and two control containers located outside the cell.

The thermodynamics of corrosion is best represented by Potential-pH diagrams or, as they are frequently referred to as, Pourbaix diagrams.[23] The diagrams are generated from thermodynamic calculations and present a map of the regions of stability of a metal and its corrosion products in aqueous environments. The Pourbaix diagram for water, with no metal, is shown as Figure 74.[24] The two diagonal lines, identified as (a) and (b), define the region of stability for water as a function of potential and pH. For potential and pH conditions between lines (a) and (b) water is thermodynamically stable. For potentials above line (b) water is thermodynamically unstable and oxygen is liberated, while at any conditions of potential and pH below line (a) water is thermodynamically unstable and hydrogen gas forms. Therefore, from measurements of pH and potential made during these experiments we can investigate whether it is thermodynamically possible for the corrosion reaction to generate hydrogen. If the measured E_{corr} value from a test is below line (a), hydrogen evolution is possible.

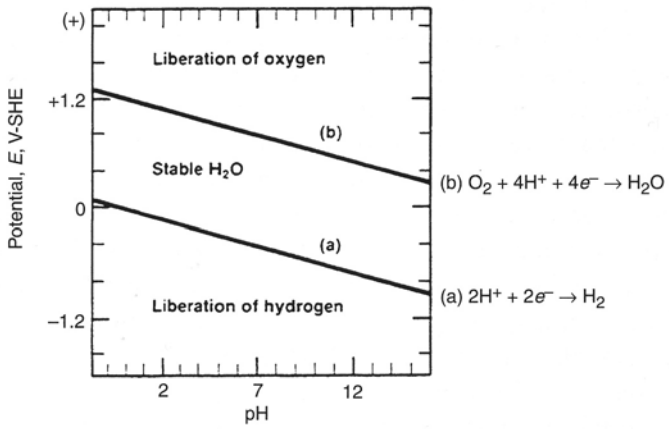

Figure 74. Pourbaix diagram for water.

The equation for line (a) is derived from the Nernst equation:

$$E = E° - \frac{RT}{nF} * pH \qquad \text{equation 9}$$

where E° is the standard potential for hydrogen, R is the ideal gas constant, T is the temperature, n is the number of electrons involved in the hydrogen reduction reaction and F is the Faraday constant. Thus, given the pH and temperature of the test, the potential below which hydrogen evolution would occur may be calculated. For the sludge dissolution tests, the pH of the solution was approximately 1, and for the hydrogen reaction E° is 0.000 V. Table 29 shows the potential as a function of temperature. The potential utilized in the Nernst equation is with reference to the hydrogen electrode. The measurements during these tests were made with a saturated Ag/AgCl electrode. To convert the hydrogen potential to one with reference to the Ag/AgCl, subtract 197 mV. These potentials are also shown in Table 29. The E_{corr} values measured during the tests will be compared to these values to determine if hydrogen evolution is possible.

Table 29. Hydrogen evolution potential (E_{H2}) values for the sludge dissolution tests.

Temperature	E_{H2} (mV vs. NHE)	E_{H2} (mV vs. Ag/AgCl)
25 °C	-59	-256
50 °C	-55	-252
75 °C	-51	-248

Wiersma and Peacock derived the following relationship between the corrosion rate and the hydrogen generation rate (G_r).[25]

$$G_r = 3.8 \times 10^{-5} * CR * SA \qquad \text{equation 10}$$

where CR is the corrosion rate in mpy and SA is the surface area of the coupon in ft^2. This equation is only applicable if the cathodic reaction that occurs is hydrogen evolution. The corrosion rates determined by the LPR measurements were used to estimate the rate at which hydrogen is evolving.

Sludge Dissolution Vessel Corrosion Results

E_{corr} measurements

The results of the E_{corr} vs. time measurements for the six tests are shown in Figure 75 through Figure 80 and are summarized in Table 30. The time shown in each figure is relative to the initial addition of oxalic acid to the dissolution vessel. A line is drawn on each plot to indicate the potential below which hydrogen generation is possible. Each figure shows the results from each coupon in the vessel. The "Plate" is the horizontal coupon at the bottom of the vessel. "Position 1" is the lowest vertically oriented coupon with the remaining vertical coupons identified consecutively as the distance above the vessel bottom increases.

The behavior of E_{corr} at the 50 and 75 °C was similar (see Figure 75, Figure 76, Figure 78 and Figure 79). At 50 °C and 75 °C, E_{corr} for the plate and Position 1 coupons initiated at potentials below E_{H2} and increased to potentials 150 to 200 mV greater than E_{H2}. The low initial E_{corr} was likely due to two factors: lack of mixing and surface condition. The lack of mixing left the metal in direct contact with oxalic acid for a period of time, rather than in contact with oxalic acid containing dissolved sludge. Visual observations of these two coupons during the test indicated that, at this stage of the test, the metal surface remained in a pristine (i.e., no iron oxides present) condition. Separate tests on pristine coupon in pure oxalic acid also resulted in E_{corr} values within this range. At these conditions, hydrogen evolution is the preferred cathodic reaction due to the limited amount of dissolved sludge present in the solution. The subsequent increase in potential is likely associated with the increase of ferric ion in solution as the sludge dissolves. Thus, the preferred cathodic reaction becomes ferric ion reduction. The E_{corr} for coupons in Positions 2 and 3, in contrast, initiated at values 100 to 200 mV greater than E_{H2} and remained at these values for the duration of the test. The higher E_{corr} values are likely due to the presence of sufficient ferric ion in solution which contacted the coupons initially.

The effect of mixing is also evident as shown in Figure 78 and Figure 79. These tests yielded a greater difference in the values of E_{corr} than observed for the mixing tests. This result suggests that diffusion of the ferric ion limited the rate of the cathodic reaction. With mixing the concentration of the dissolved species remained more uniform and, thus, E_{corr} for all the coupons approached a similar value (see Figure 75 and Figure 76).

The behavior at the lower temperature (25 °C) was also controlled by the cathodic reaction (see Figure 77 and Figure 80). However, in this case the two competing reactions were oxygen reduction and hydrogen evolution. Unlike the higher temperature tests, we believe the concentration of ferric ion remained too low to affect the corrosion

reaction. The effect of mixing is also apparent. In tests with mixing, shown in Figure 77, both the plate and position coupon were exposed to unmixed conditions for the first ~30 hours they were immersed – complete immersion of these coupons did not occur until 30 or 40 hours after oxalic acid addition began and mixing did not begin until after 70 hours. Initially, the potential for the plate coupon was less than E_{H2}. We believe sufficient sludge dissolution had occurred in the lower regions of the vessel to limit oxygen solubility near the plate coupon and thus hydrogen evolution was the favored cathodic reaction. However, the coupon in Position 1, behaved as though it were controlled by oxygen reduction initially. We believe this behavior occurred because at this point the sludge species had not yet diffused to the upper region of the solution. The availability of oxygen near the interface also favored the oxygen reduction reaction. As the species from the dissolved sludge solution diffused to the top of the liquid, E_{corr} for the coupon in Position 1 decayed as the solubility of oxygen decreased. At initiation of agitation, the plate and coupons in Positions 1 and 2 were immersed. The initial effect was that E_{corr} for all three coupons increased. This behavior indicates that oxygen reduction is a more significant participant in the cathodic reaction. However, after approximately 50 hours (i.e., the 120 hour mark of the test), E_{corr} for all three coupons began to decay to values below E_{H2}. We hypothesize the presence of other species from the dissolved sludge in the solution limited the availability of oxygen to these coupons. Thus hydrogen evolution became the controlling reaction. When the coupon in Position 3 became immersed approximately 90 hours after mixing initiated, the initial E_{corr} was less than E_{H2}. This trend suggests that the solution was saturated with species from the dissolved sludge at this time and thus the availability of oxygen was limited thereby hydrogen evolution became the preferred cathodic reaction at this location.

For the non-mixing test at low temperature, shown in Figure 80, E_{corr} for the plate and the coupon in Position 1 remained less than E_{H2} for most of the test. (We are uncertain as to why the initial E_{corr} for the plate was at positive values well above E_{H2}.) In contrast, E_{corr} for the coupons in Position 2 and 3 initiated at values 25 to 200 mV above E_{H2} and decayed slightly for the remainder of the test. We speculate that a concentration gradient existed for the dissolved species in the sludge. The sludge dissolves at the bottom of the vessel and hence the concentration of dissolved species is greater at this location. The presence of these dissolved species in solution limits the availability of oxygen for the cathodic reaction. Thus, hydrogen evolution occurs at the plate and the coupon at Position 1. The concentration of the dissolved sludge species at the top of the liquid is less because these species have not yet diffused to this location. Thus, oxygen is more soluble and hence available to participate in the cathodic reaction at for coupons at Positions 2 and 3. The decay may reflect diffusion of the dissolved species toward the top of the liquid and hence a decreasing availability of oxygen.

The highest, or most noble, value of E_{corr} occurred during the 75 °C tests (see Figure 76). The E_{corr} for the horizontal plate shifted almost 250 mV after approximately 110 hours of exposure. These higher potentials typically indicate a shift into a passive region where corrosion rates are low. No such shift occurred in any other tests.

The Position 3 coupon tends to have the most positive or noble E_{corr}, while either the horizontal plate or Position 1 coupons have the most negative or active E_{corr} (see Table 30 and Figure 75 through Figure 80). The higher values of E_{corr} were likely due to the increased presence of the ferric ion in solution that first contacts the coupon. The difference in E_{corr} between the Position 3 coupon and the horizontal plate coupon at any given time is a function of mixing. The difference in the potential is greater for the non-mixing cases. Both of these observations indicate that oxygen and the ferric ion are factors in the corrosion behavior.

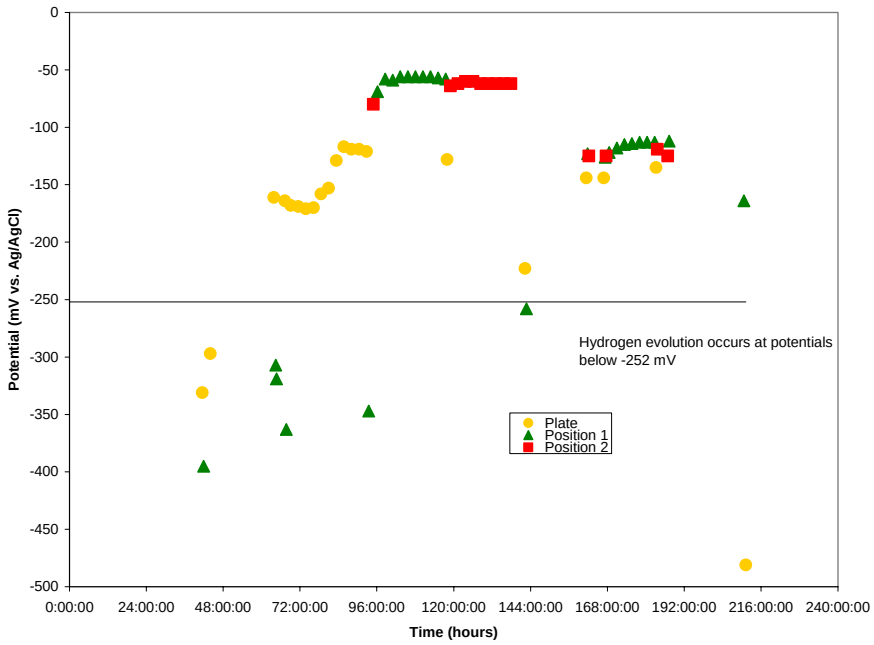

Figure 75. E_{corr} measurements for Test 1 (mixed at 50 °C): polished coupons.

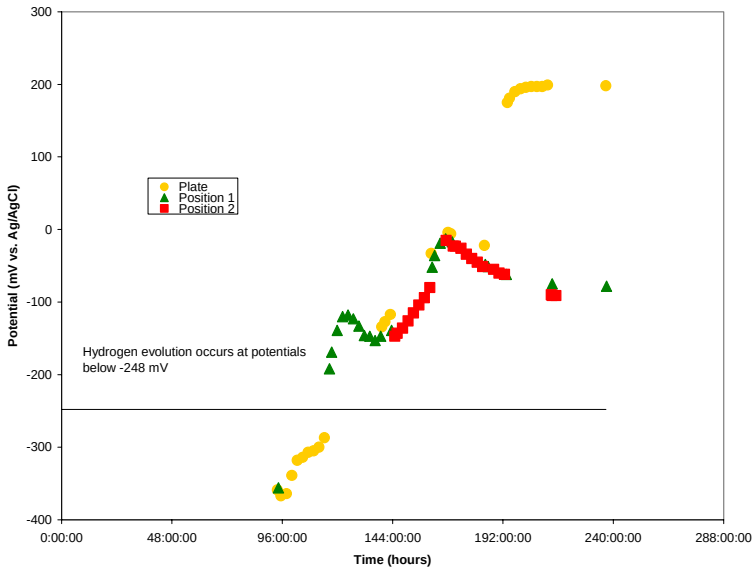

Figure 76. E_{corr} measurements for Test 2 (mixed at 75 °C): polished coupons.

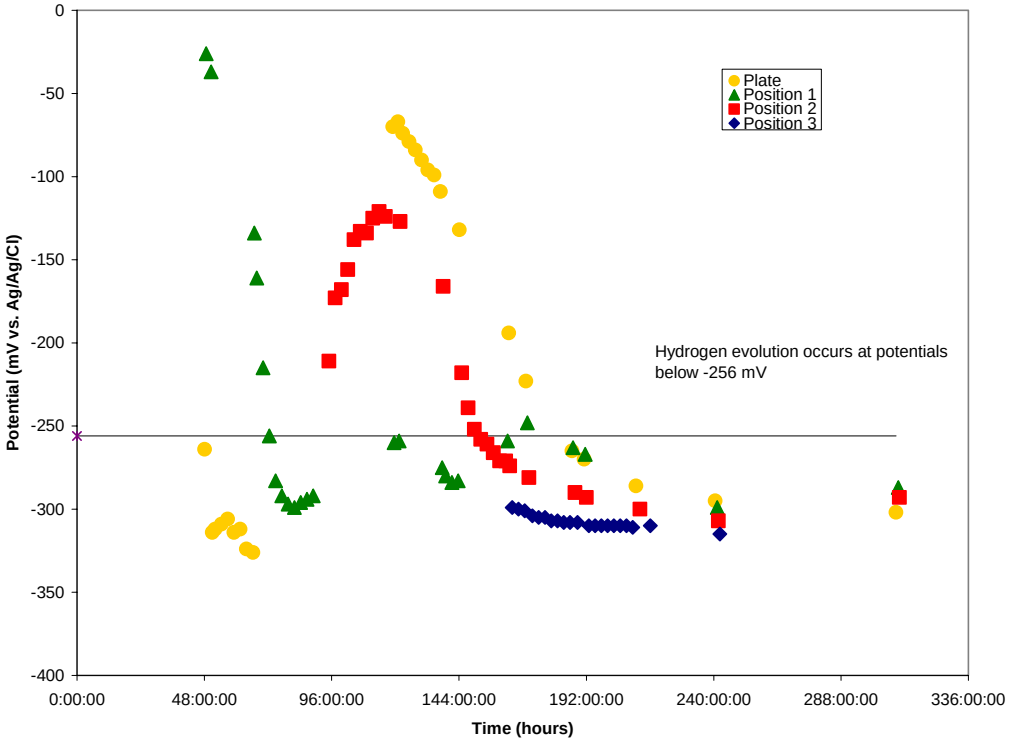

Figure 77. E_{corr} measurements for Test 3 (mixed at 25 °C): mill-scale coupons.

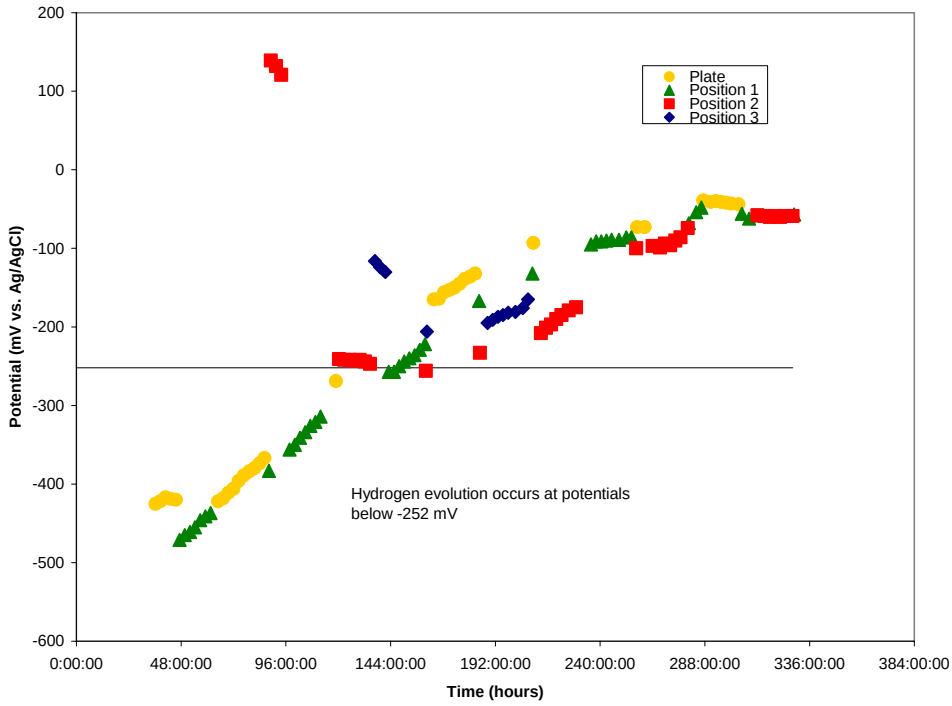

Figure 78. E_{corr} measurements for Test 4 (unmixed at 50 °C): mill-scale coupons.

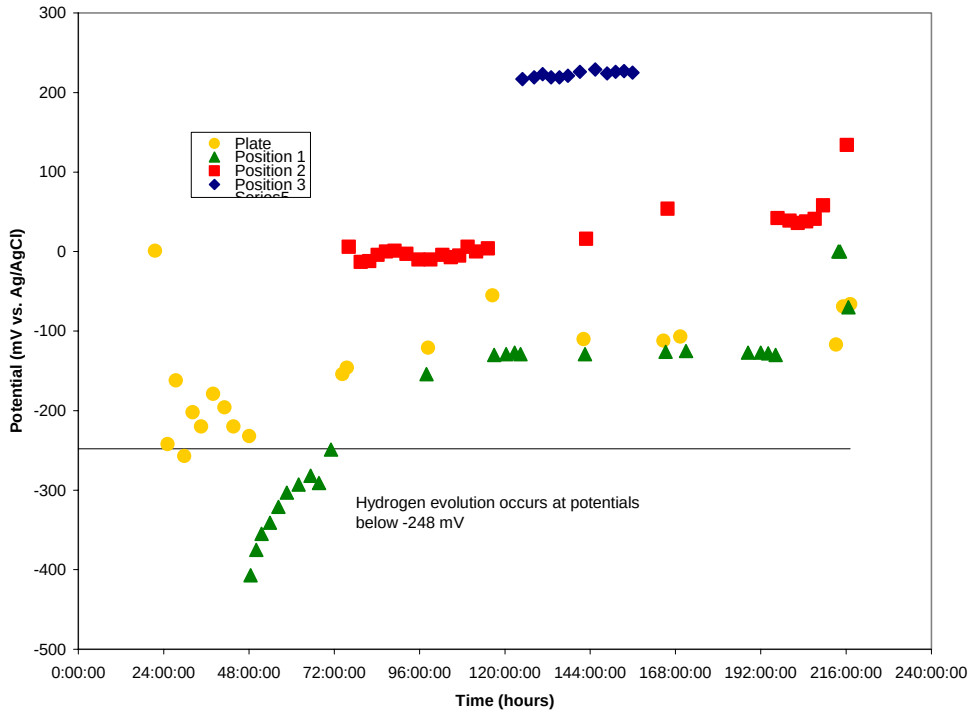

Figure 79. E_{corr} measurements for Test 5 (unmixed at 75 °C): mill-scale coupons.

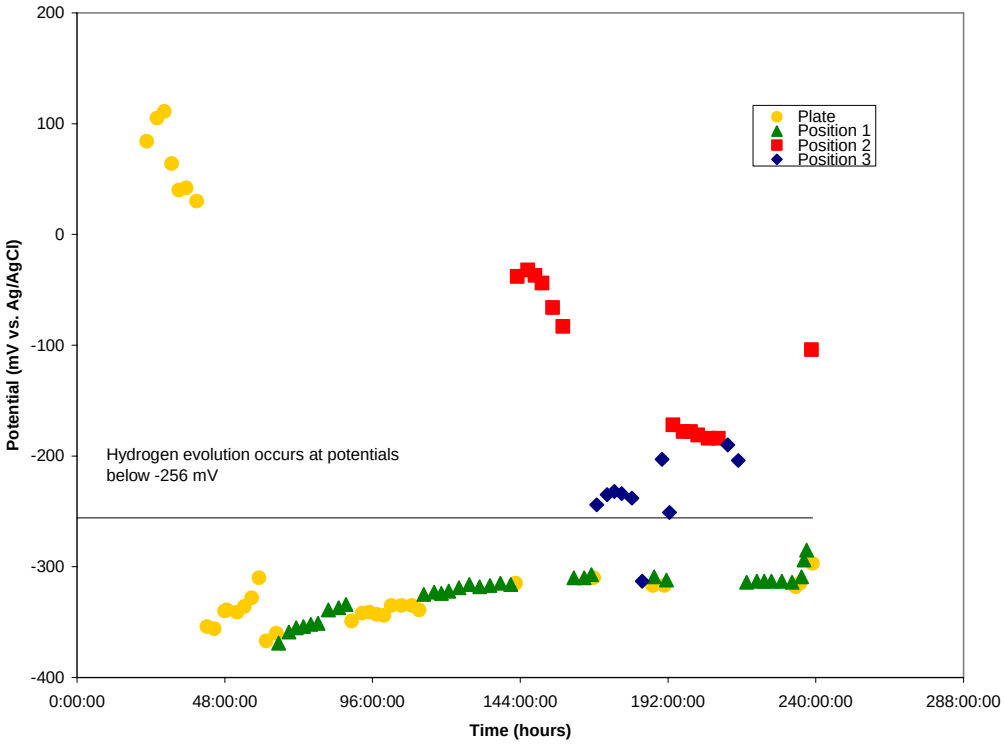

Figure 80. E_{corr} measurements for Test 6 (unmixed at 25 °C): mill-scale coupons.

Corrosion Rate Measurements

The corrosion rates also changed significantly during the experiments. Figure 76 shows an example of the changes. This figure shows the corrosion rate for the horizontal plate during Test 2 at 75 °C. Initially the corrosion rate is relatively low at approximately 5 mpy. Over the next 50 hours, the rate gradually increases to a maximum of 30 mpy. After 110 hours of exposure the corrosion rate decreases dramatically to less than 0.1 mpy. The drop in corrosion rate coincides with the positive shift in the E_{corr}. Heavy deposits were observed on the coupon at this time. Table 30 characterizes similar shifts in corrosion rate for the other tests. Five characteristic corrosion rates are reported: 1) the initial corrosion rate (earlier than 2 hours), 2) the final steady state corrosion rate (reached after > 100 hours of exposure), 3) the corrosion rate while E_{corr} is less than E_{H2} (which provides an estimate of the rate of hydrogen generation), 4) the maximum corrosion rate at a given time, and 5) the time averaged corrosion rate. The latter corrosion rate is determined by integrating beneath the corrosion rate vs. time curve, and then dividing by the duration of the test. This corrosion rate is representative of the amount of damage the coupon experienced during the test and will be used as a realistic corrosion rate that may be applied to the tanks

The highest initial corrosion rates occurred on vertically oriented polished coupons at the highest temperatures. The highest corrosion rate reached 170 mpy on a Position 2 coupon during Test 2 at 75 °C.

The lowest initial corrosion rates occurred on the mill scale coupons at any position. The presence of the mill scale is protective, at least initially, until the oxalic acid removes this layer.

The initial corrosion rates demonstrate an effect of mixing. Test 3 with mixing and Test 6 without mixing occurred at 25 °C. The initial corrosion rate for the plate and Position 1 coupons are nearly identical for the two tests. During the initial stages of exposure for these coupons there was no mixing. However, the corrosion rates for the coupons in Positions 2 and 3 for the two tests are different by nearly two orders of magnitude. The higher corrosion rates during the mixing tests (Test 3) may be a result of increasing the availability of oxygen or ferric ion.

The corrosion rates passed through a maximum and then reach a steady state after greater than 100 hours of exposure. The highest steady state current density typically occurred on the Position 1 coupon. The lowest steady state current density typically occurred on the horizontal plate. These coupons are located next to each other and typically the values of E_{corr} were very similar. However, the top of the horizontal plate was typically covered with a thick layer of ferrous oxalate. The ferrous oxalate layer on the vertical coupon, in contrast, was typically disrupted resulting in areas with visible deep general corrosion and pitting.

In general, corrosion rates where E_{corr} was less than E_{H2} proved relatively low compared to the corrosion rates when E_{corr} was more positive. The highest observed corrosion rate for a situation with $E_{corr} < E_{H2}$ was 55 mpy on the Position 1 coupon during Test 3 at 25 °C. This rate occurred during the final few hours of the test when personnel increased the mixing speed in the vessel substantially. For the most part, corrosion rates when E_{corr} was less than E_{H2} remained less than 20 mpy.

The maximum instantaneous corrosion rates occurred typically between 50 and 100 hours of exposure on vertically oriented coupons, in the polished condition, while the solution was being mixed. The maximum rate observed was 170 mpy for the Position 2 coupon for Test 2 at 75 °C.

The corrosion rate for the horizontal plate during Test 2 at 75 °C decreased significantly after approximately 140 hours (see Figure 76). This decrease correlated with the increase in potential (-100 mV to +200 mV) observed on this coupon. This shift correlated with an active/passive transition observed in separate electrochemical tests. The ferrous film that forms becomes more stable (i.e., lower corrosion rates) at these higher potentials. The figure also shows why caution is needed when extrapolating time-averaged corrosion rates to longer times. For example, if the test stopped after 192 hours, the time averaged corrosion rate would be 18 mpy. Although this estimate is not much greater than that measured (15 mpy), if the low corrosion rates observed after 192 hours continued to longer times, the corrosion rate would be overestimated. In contrast, an increasing corrosion rate at the conclusion of the test would result in the time-averaged corrosion rate underestimating the corrosion rate.

Table 31 contains the instantaneous hydrogen generation rates and the cumulative hydrogen generated for each coupon based on calculations from the corrosion measurements. These results were calculated from equation 10. The instantaneous rates were obtained from the maximum corrosion rate, as measured by LPR, while E_{corr} was less than E_{H2}. The cumulative hydrogen evolved was calculated by integration of the instantaneous corrosion rate versus time plot. The time limits for the integration were defined by the time for which E_{corr} was less than E_{H2}. The predicted values exceed the values obtained from the GC measurements indicating a less than theoretical yield to hydrogen from the reactions.

The instantaneous generation rates from the coupons were similar for all the tests (typically 0.2-1 cm^3/hr) except for Test 4 (50 °C, unmixed), where the corrosion rate measured was extremely low. Hydrogen generation for the higher temperature tests tended to be during the initial stages when the coupon was first immersed. The mill-scale on the coupon may have provided initial protection and therefore a lower corrosion rate resulted.

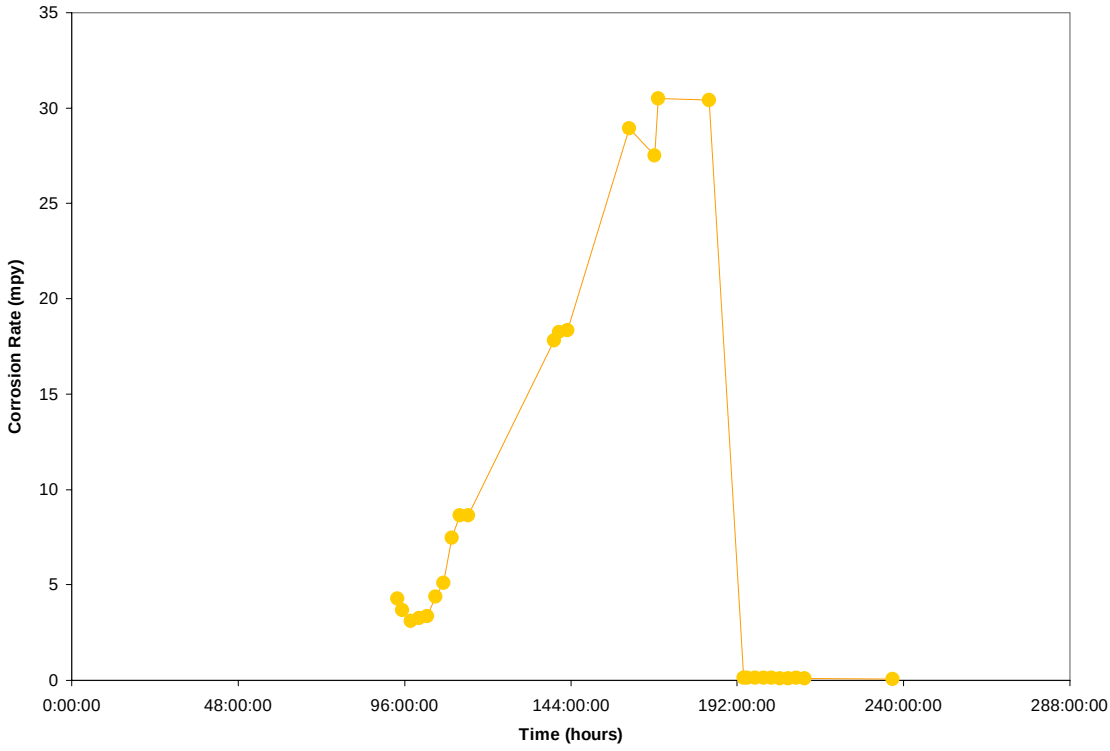

Figure 81. Corrosion rate as a function of time for the horizontal plate during Test 2 (75 °C, mixed).

Table 30. Corrosion results for coupons from Dissolution Vessel.

Test	Coupon Position	E_{corr} at time < 2 hours (mV)	Final Steady State E_{corr} (mV)	Time that E is less than E_{H2} (hours)	Corrosion Rate at time < 2 hours (mpy)	Final Steady State Corrosion Rate (mpy)	Corrosion Rate while E < E_{H2} (mpy)	Maximum Instantaneous Corrosion Rate (mpy)	Time Averaged Corrosion Rate (mpy)
1 (50°C, polished, mix)	Plate	-331	-135	< 10	3.4	9	3.4	10	5
	1	-395	-112	< 60	7.7	74	7.7	78	30
	2	-80	-125	0	3.5	52	NA	66	28
2 (75°C, polished, mix)	Plate	-359	+198	72	3.5	0.1	3.5	30	15
	1	-356	-78	< 2	24	85	24	128	67
	2	-147	-91	0	70	70	NA	170	86
3 (25°C, mill-scale, mix)	Plate	-264	-300	146	0.02	0.4	0.02-0.65	0.65	0.5
	1	-26	-287	237	6	55	1-55	55	15
	2	-211	-293	160	3	30	3-30	30	21
	3	-300	-310	78	20	50	20-50	50	40
4 (50°C, mill-scale, no mix)	Plate	-425	-40	82	0.32	0.2	0.22-0.32	0.32	0.23
	1	-471	-55	100	0.7	0.7	0.74-0.81	0.81	0.76
	2	139	-60	0	0.55	0.5	NA	1.25	0.34
	3	-116	-165	0	0.15	0.3	NA	0.36	0.28
5 (75°C, mill-scale, no mix)	Plate	1	-70	0	0.2	0.25	NA	1.3	0.45
	1	-407	-130	23	8	16	6.2-25.8	70	36
	2	6	40	0	0.45	0.6	NA	0.77	0.49
	3	217	240	0	0.07	0.08	NA	0.1	0.08
6 (25°C, mill-scale, no mix)	Plate	84	-315	197	0.05	0.44	0.05-1.9	1.9	0.87
	1	-369	-310	171	6	18	6.3-30.1	30.1	11
	2	-38	-180	0	0.02	0.02	NA	0.02	0.02
	3	-244	-204	< 7	0.002	0.003	0.0024	0.0024	0.002

Table 31. Estimated hydrogen generation rates based on the corrosion rate measurements during the process demonstrations.

Test	Coupon Position	Surface Area (ft^2)	Time $E_{corr} < E_{H2}$ (hours)	Maximum Corrosion Rate while $E_{corr} < E_{H2}$ (mpy)	Maximum Instantaneous Hydrogen Generation Rate (cm^3/hour)	Predicted Cumulative Hydrogen Generated (cm^3)
1	Plate	0.18	10	3.4	0.61	4.9
	1	0.02	60	7.7	0.16	6.6
2	Plate	0.18	72	3.5	0.69	20
	1	0.02	2	24	0.51	11
3	Plate	0.18	146	0.65	0.097	57.7
	1	0.02	237	55	1.03	59.7
	2	0.02	160	30	0.56	65.1
	3	0.02	78	50	0.93	12.2
4	Plate	0.18	82	0.32	0.053	4.4
	1	0.02	100	0.81	0.027	1.6
5	1	0.02	23	25.8	0.57	8.1
6	Plate	0.18	197	1.9	0.32	40
	1	0.02	171	30	0.56	31
	3	0.02	7	0.0024	< 0.0025	< 1

Post-test Visual Examination of Coupons

The coupons appeared visually similar for all tests. The horizontal plate coupon from Test 2 at 75 °C (see Figure 82) is typical of the top surface of all the horizontal plates. Thick deposits of blue-green to yellow-green ferrous oxalate covered the surface. X-ray diffraction identified this layer as humboldtine (α-$FeC_2O_4 \bullet 2H_2O$), which is monoclinic ferrous oxalate and sodium ferrous oxalate, which is the orthorhombic ferrous oxalate ($Na_2Fe(C_2O_4)_2$), the dehydrated form of humboldtine.[26] Beneath this layer the surface was rough and uniformly corroded.

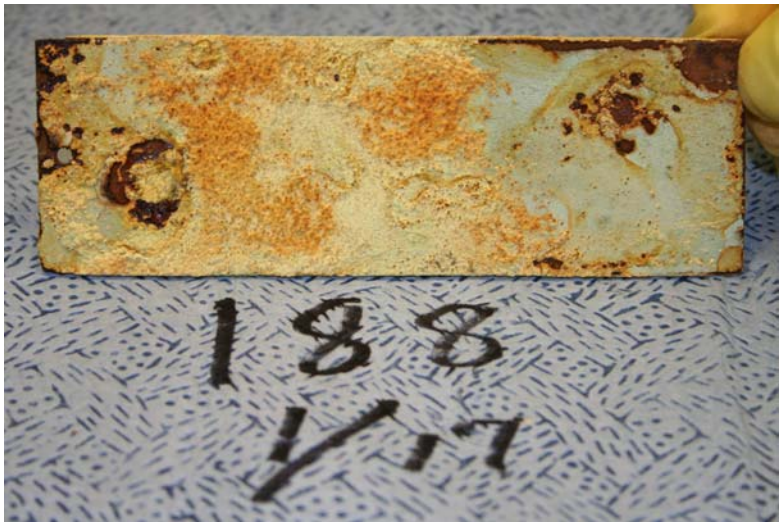

Figure 82. Post-test photo of horizontal plate from Test 2 (75°C, mixed).

In contrast, both phases of ferrous oxalate deposits occurred randomly on the vertical coupons and on the bottom of the horizontal plate (see Figure 83). Between the ferrous oxalate deposits were regions covered by iron oxides, typically goethite or lepidocrocite. Although, the attack appeared uniform in most cases, isolated cases of pitting occurred on the vertical surfaces.

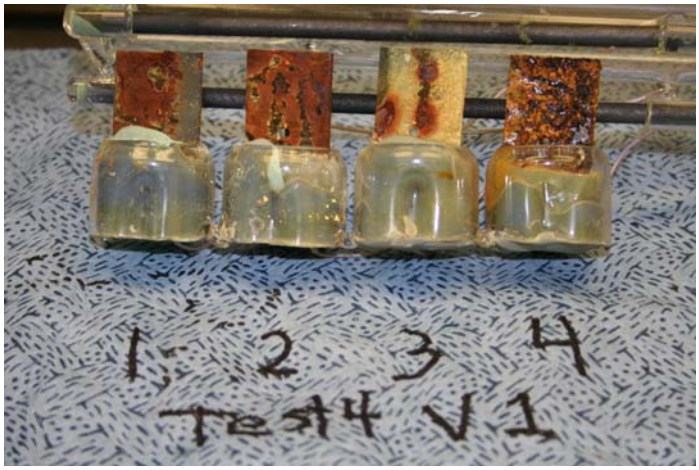

Figure 83. Post-test photo of vertical coupons from Test 4 (50 °C, unmixed).

Note goethite and humboldtine on first three coupons.

Coupons in Positions 4 and 5 on the "tree-like" holder were exposed to the vapor space during the test. Although we could not perform electrochemical measurements on these coupons, the corrosion behavior was visually monitored. During the test, condensate formed on the coupons and corrosion occurred. General area corrosion occurred for the polished coupons, while the mill-scale coupons show random corrosion regions (see Figure 84). These corrosion products were typically lepidocrocite, goethite, and magnetite. We found no evidence of humboldtine on any of the vapor space coupons

indicating that the oxalic acid does not accelerate corrosion in the vapor space during oxalic acid chemical cleaning.

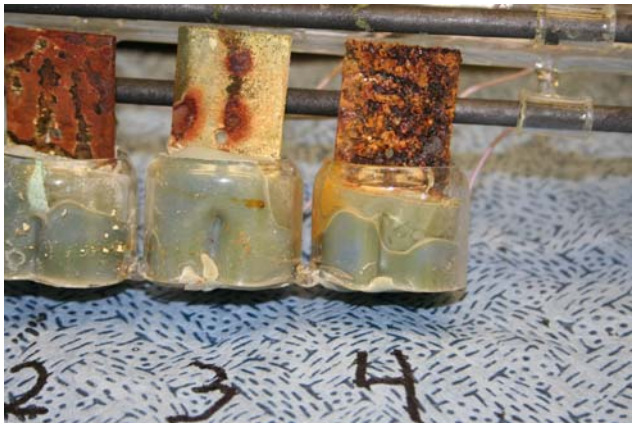

Figure 84. Post-test photo of vapor space coupon from Test 4 (50 °C, unmixed). Note lepidocrocite, goethite and magnetite on coupon 4.

Receipt Vessel Corrosion Results

Potential Monitoring and Corrosion Rate Measurements

The receipt vessel tests included three distinct stages: 1) initial holding period while the vessel contained only caustic supernate, 2) addition of the dissolved sludge solution, and 3) mixing of the vessel after transfer. Table 32 summarizes the E_{corr} potentials and corrosion rates observed during each of these stages.

During the initial stage, coupons in Positions 1 and 2 were typically exposed to the caustic supernate. As shown in Table 32 the E_{corr} values ranged between -114 mV to 122 mV. The -114 mV is typical for carbon steel exposed to concentrated caustic waste.[27] The E_{corr} for the mill-scale coupons proved slightly more positive than the polished samples, although the measurements were less consistent. The corrosion rates remained at expected low (< 0.1 mpy) values**.**

While the dissolved sludge solution was added to the Receipt Vessel, stratification occurred (see Figure 26). In most of the tests, the coupon in Position 1 remained in the clear supernate, the coupon in Position 2 was at the interface where the sludge precipitated, and the coupon in Position 3 was in a second clear layer that was initially acidic. During this stage the contents were relatively static. Initially, the coupons behaved as though they were each in their own separate environment. The potential and the corrosion rate for the Position 1 coupon did not change significantly from the initial stage values. The corrosion behavior of the Position 2 coupon changed significantly as E_{corr} decreased by as much as 500 mV over the 24 hour period. The potential difference between the coupons reached its maximum value during this time (i.e., as high as 430 mV between Position 1 and Position 2 coupons). The corrosion rate of the Position 2 coupon initially increased to about 10 mpy. This behavior was observed most dramatically during Test 1 (50 °C, mixed). The presence of mill-scale decreased the

initial corrosion rate suggesting the initial protection provided by the mill scale allows sufficient time for diffusion to occur and raise the pH of the solution thus limiting the amount of attack. The coupon in Position 3 underwent the most severe attack. This layer was slightly more acidic initially and therefore higher corrosion rates were anticipated. The highest corrosion rate observed was 90 mpy on a polished coupon during Test 1 (50 °C, mixed). The mill-scale also improved the resistance of the carbon steel to the acidic solution as well, as the corrosion rates measured 1.4 mpy or less.

Mixing the vessel contents made the environment more homogeneous and, as expected, the corrosion behavior proved more uniform for the three coupons. The final E_{corr} for the coupons increased to between -204 to -61 mV. The potential difference between the coupons also decreased to less than 100 mV. Corrosion rates on all three coupons typically reached less than 1 mpy.

Post-test visual examination of coupons

The appearance of the coupon depended upon its location and whether the initial surface was in the polished or mill-scale condition. For the polished coupons used in Test 1, the Position 1 and Position 2 coupons showed evidence of pitting attack and light general corrosion (see Figure 85). The pitting may be the result of a localized environment within the precipitate cloud that formed during neutralization of the dissolved sludge solution. The Position 3 coupon for neutralization Test 1 (50 °C, mixed) showed significant general corrosion and evidence of ferrous oxalate formation. This coupon had been exposed to the dissolved sludge solution that stratified at the top of the slurry. The vapor space coupons showed evidence of light staining, but overall no significant attack.

None of the mill-scale coupons showed any significant corrosion (see Figure 86). Some slight staining of the Position 2 coupon is seen at the interface where the precipitation occurred. Slight corrosion occurred on the vapor space coupon, although no accelerated attack is noted. These results provide evidence that the mill-scale is at least initially protective.

Table 32. Corrosion results for coupons from Receipt Tank.

Test	Coupon Position	E_{corr} in Supernate (mV)	Corrosion Rate in Supernate (mpy)	E_{corr} during sludge slurry transfer (mV)	Corrosion Rate during sludge slurry transfer (mpy)	E_{corr} during mixing (mV)	Corrosion Rate during (mpy)
1 (polished)	1	-102	0.013	-102 to -312	0.015 to 0.006	X	X
	2	-114	0.045	-531 to -492	23 to 0.35	X	X
	3	NA	NA	-298 to -132	91 to 61	X	X
2 (polished)	1	X	X	X	X	X	X
	2	X	X	X	X	X	X
	3	X	X	X	X	X	X
3 (mill-scale)	1	-71	X	159 to 230	< 0.43	-118	< 0.12
	2	NA	NA	-2 to -83	0.022	-175	0.009
	3	NA	NA	-116	0.62	X	X
4 (mill-scale)	1	-69	0.09	-82	0.12	170 to -117	0.56 to 4.47
	2	-81	< 1.43	-75 to 215	1.4 to 0.42	208 to -183	0.008
	3	NA	NA	X	X	-36 to -204	< 1.46
5 (mill-scale)	1	-84	< 0.72	-75 to -386	0.85 to 0.39	-347 to -104	0.43 to 1.03
	2	-51 to 122	0.004	137 to -385	0.006	-352 to -190	0.0014
	3	NA	NA	-59 to -381	0.46 to 0.11	-305 to -177	0.11
6 (mill-scale)	1	-103	0.023	-103 to -121	0.021	-85	0.021
	2	-87	0.028	-88 to -77	0.028	-61	0.029
	3	NA	NA	160 to 6	0.27 to 1.4	-68	0.39 to 0.83

Notes: NA signifies that the coupon was not immersed. An "X" means that a stable measurement could not be obtained. A "<" indicates that the LPR curve behavior indicated that the corrosion rate was lower than the value calculated by taking the slope of the line at $E=E_{corr}$.

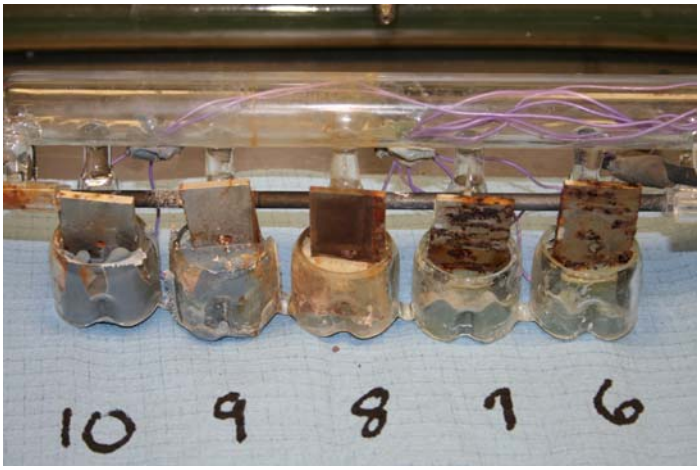

Figure 85. Post-test photo of coupons from Test 1 (50 °C, mixed) Receipt Tank.

Coupon 6 was in Position 1, Coupon 7 was in Position 2, and Coupon 8 was in Position 3. Coupons 9 and 10 were in the vapor space.

Figure 86. Post-test photo of coupons from Test 6 (50 °C, unmixed) Receipt Tank.

Coupon 1 was in Position 1, Coupon 2 was in Position 2, and Coupon 3 was in Position 3. Coupon 4 was in the vapor space.

Measurement of Hydrogen Generation during Corrosion Coupon Testing

These tests included direct measurement of the hydrogen generation rate during the corrosion experiment. The equipment monitored temporal pressure change in a closed vessel for a short period of time (i.e., 4 hours or less). The vessel was then vented to a gas chromatograph to measure the composition of the gas. The basic equation for determining hydrogen generation rate from these measurements is derived from the ideal gas law. The pressure, P, in the vessel is expressed as:

$$P = n R T/V \qquad \text{equation 11}$$

where n is the number of moles, R is the gas constant (of 0.0821 mole-l/atm-K), T is the temperature in degrees K, and V is the volume in liters of the vessel, tubing and pressure transducer. For this test, T and V are constant and therefore the first derivative of equation 11 with respect to time is:

$$\frac{dP}{dt} = \frac{RT}{V} * \frac{d\Delta n}{dt} \qquad \text{equation 12}$$

We assume that the primary gases generated from the corrosion process were hydrogen (designated as 1) and carbon dioxide (designated as 2). Therefore, the total moles of gas, n, is related to the mole fraction of gas that is measure by the gas chromatograph by:

$$\Delta n = n\,(x_1 + x_2) \qquad \text{equation 13}$$

where x_i is the mole fraction of the ith species. A constant, C, is defined as the ratio of x_2:x_1. Substitution of C into equation 13 gives:

$$\Delta n = n\,(1 + C)\,x_1 = (1 + C)\quad n_1 \qquad \text{equation 14}$$

Substitution of equation 14 into equation 12 and re-arrangement gives the following equation for the hydrogen generation rate:

$$\frac{dn_1}{dt} = (1+C)\,\frac{V}{RT}\,\frac{dP}{dt} \qquad \text{equation 15}$$

The equation for carbon dioxide generation can then be related to the hydrogen generation rate by:

$$\frac{dn_2}{dt} = C\,\frac{dn_1}{dt} \qquad \text{equation 16}$$

Thus by measuring the mole fraction of carbon dioxide and hydrogen, and the pressure change as a function of time, hydrogen generation and carbon dioxide rates can be calculated. The equation assumes that no other gases are generated. This assumption neglects the possibility of NO_x generation, which occurs due to the presence of nitrate in the supernate. Therefore, the hydrogen and carbon dioxide generation rates are likely overestimated initially. However, since there is a limited supply of nitrate in the supernate compared to the availability of the coupon and water, as the test proceeds this would become less of a factor.

Measurement of Pressure Change as a function of Time

The pressure as a function of time was recorded in an EXCEL™ spreadsheet. An example of the pressure vs. time curve for these tests is shown in Figure 87. The response was linear as a function of time in each vessel for nearly all the tests. The EXCEL™ program was used to determine the slope of the line, or dP/dt. In some cases, particularly at 75 °C, dP/dt was negligible yet both hydrogen and carbon dioxide gas were measured in the gas vented from the

vessel. The low dP/dt may be due to the difference in the temperature between the vessel and the pressure transducer. In these cases, the calculation for hydrogen generation was made assuming that the pressure in the vessel was atmospheric. The number of moles of hydrogen and carbon dioxide was then calculated. These values were divided by the time that the vessel was closed (e.g., typically 4 hours) to calculate the gas generation rates. These generation rates were compared to those calculated when dP/dt was significant and were in good agreement.

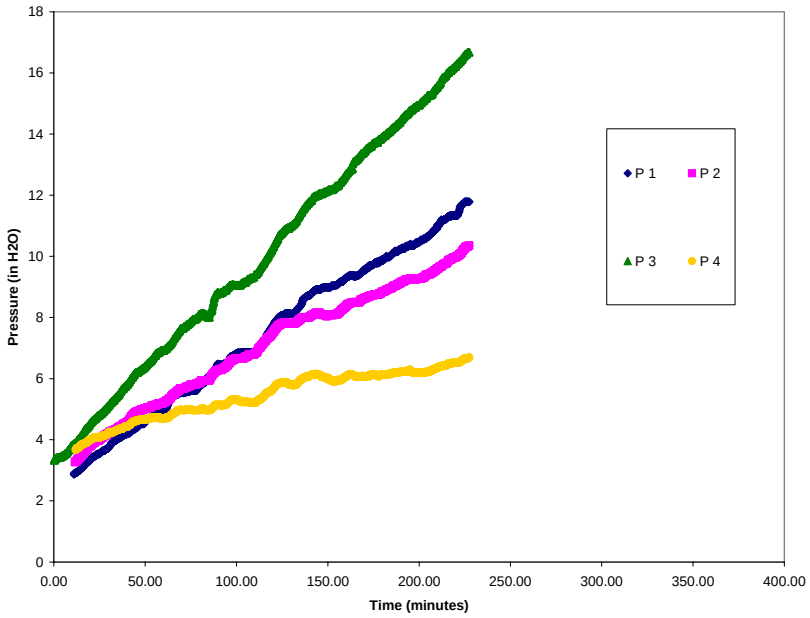

Figure 87. Plot of pressure vs. time for Test 1 (50 °C, mixed).

P1 to P4 are the pressure measurements in Containers 1 to 4, respectively.

Plots of dP/dt as a function of time for the three sets of tests are shown in Figure 88 through Figure 93. These results show that dP/dt for the initial 3 to 20 hours was very high in all cases (see Figure 88 through Figure 90). These high gas generation rates were independent of whether or not the vessel was exposed to the radiation source. The highest dP/dt was observed for the 75 °C test at nearly 600 inches of water/hour.

After this initial time, the gas generation rate decayed to a relatively constant value for the duration of the test (see Figure 91 through Figure 93). The exception occurred for Containers 1 and 3 in the 50 °C tests, where after approximately 100 hours of exposure, dP/dt increased linearly with time for the remainder of the tests (see Figure 91). The values of dP/dt were highest for the 50 °C tests (ranging from 3 to 8 inches H_2O/hr), while the lowest values occurred for the 25 °C and 75 °C tests (ranging from 1 to 3 inches H_2O/hour). In general, the values of dP/dt were slightly higher in the containers inside the radiation source.

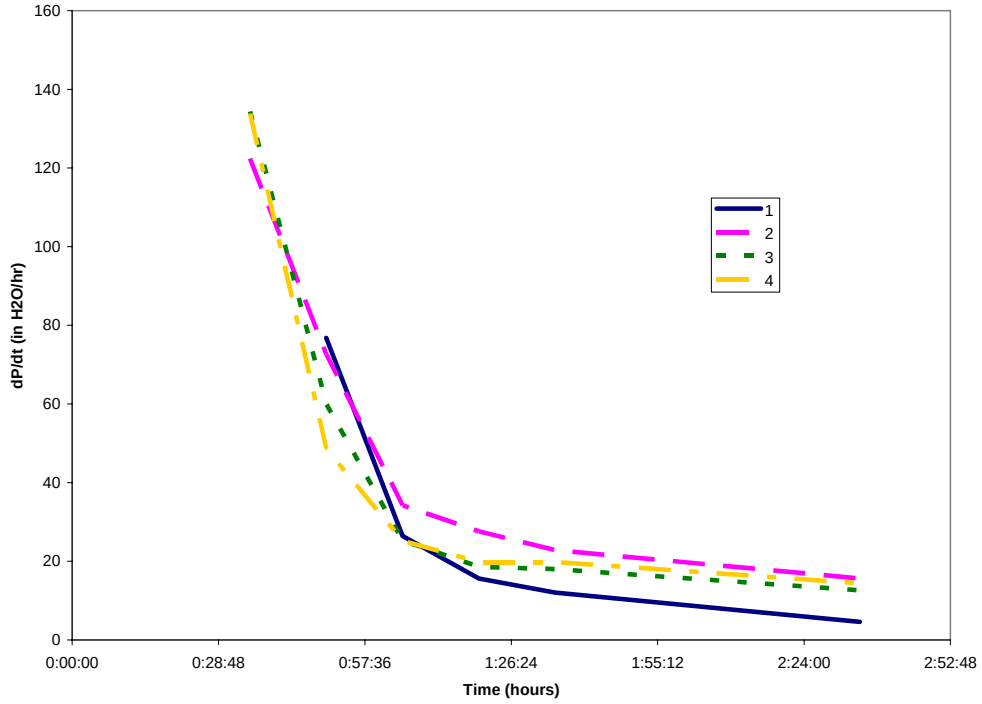

Figure 88. dP/dt for initial 3 h of radiation tests at 50 °C.

Containers 1 and 3 were in the radiation source and 2 and 4 were outside.

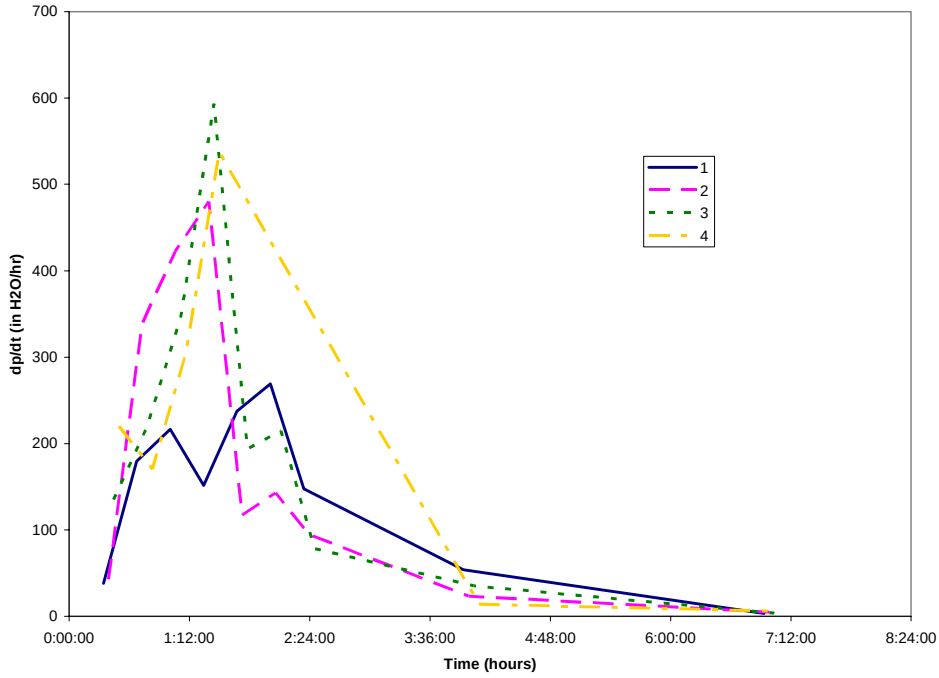

Figure 89. dP/dt for initial 7 h of radiation tests at 75 °C.

Containers 1 and 3 were in the radiation source and 2 and 4 were outside.

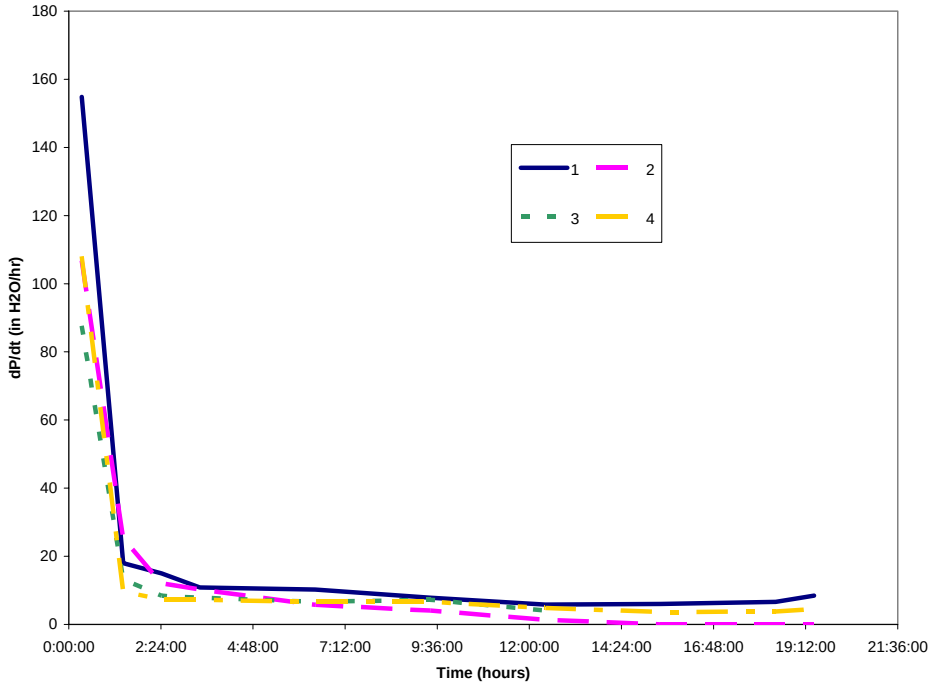

Figure 90. dP/dt for initial 20 h of radiation tests at 25 °C.

Containers 1 and 3 were in the radiation source and 2 and 4 were outside.

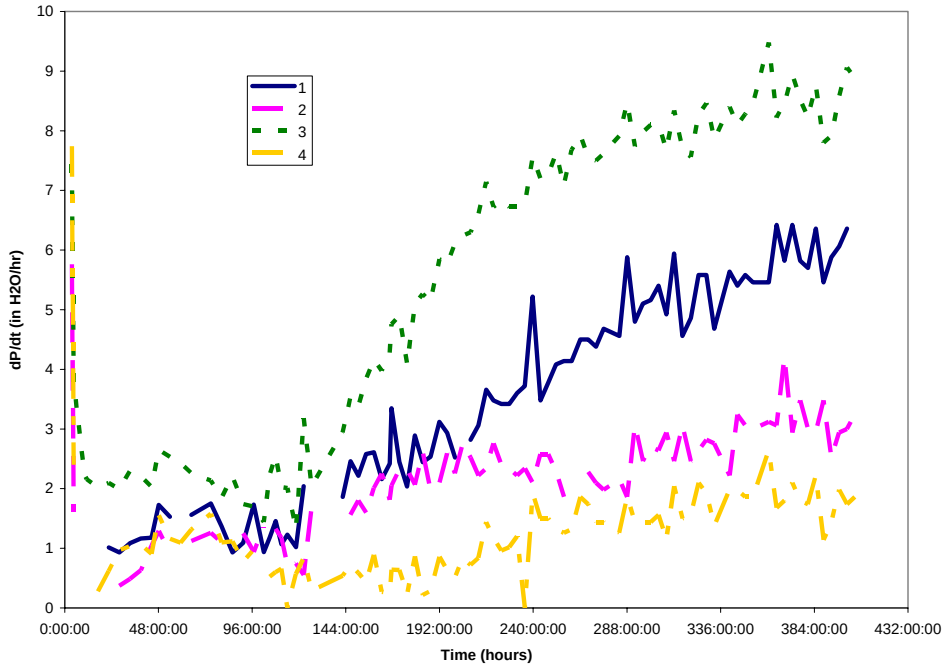

Figure 91. dP/dt after initial 3 h of radiation tests at 50 °C.

Containers 1 and 3 were in the radiation source and 2 and 4 were outside.

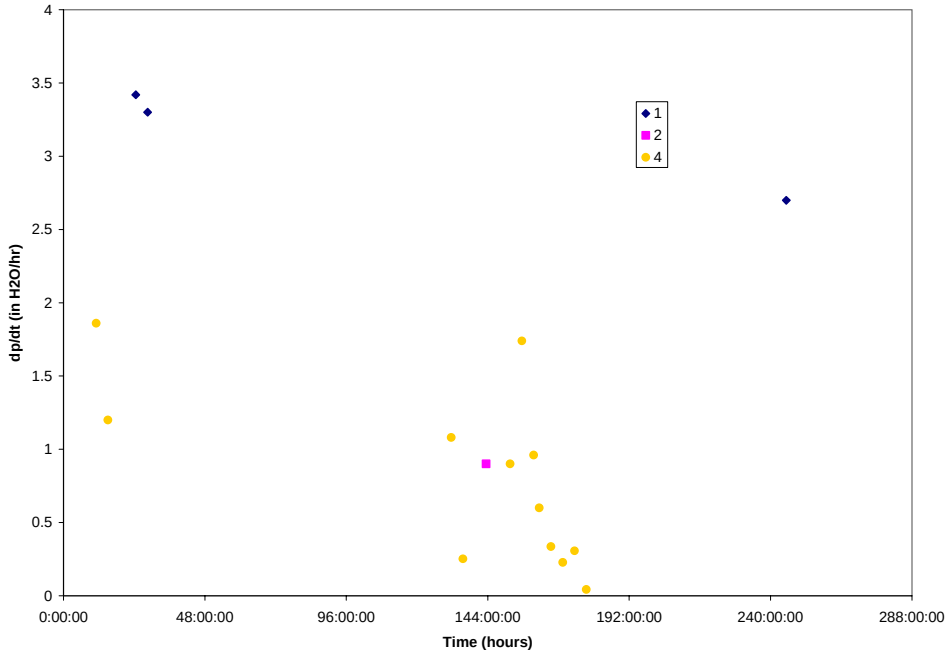

Figure 92. dP/dt after initial 7 h of radiation tests at 75 °C.

Containers 1 and 3 were in the radiation source and 2 and 4 were outside.

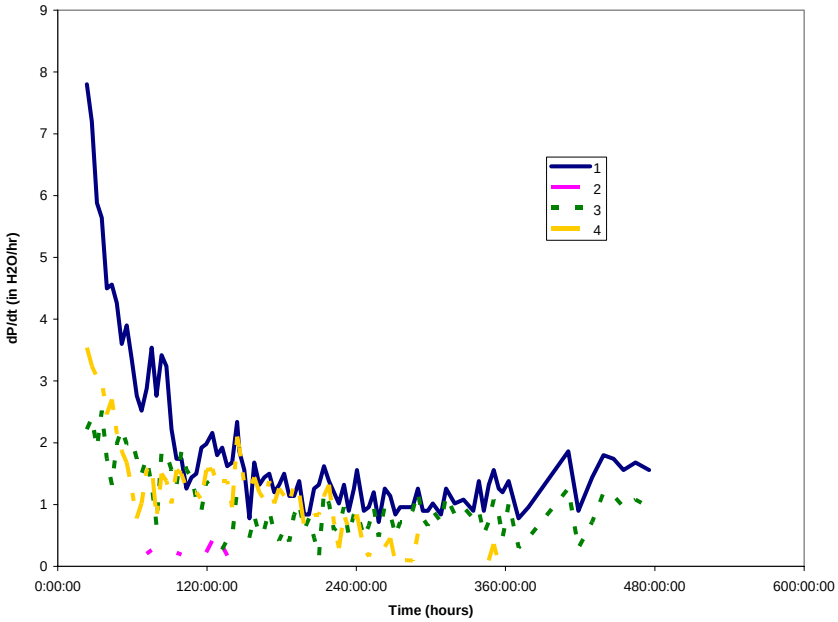

Figure 93. dP/dt after initial 20 h of radiation tests at 25 °C.

Containers 1 and 3 were in the radiation source and 2 and 4 were outside.

Hydrogen and carbon dioxide concentrations

The hydrogen and carbon dioxide gas concentrations for all the tests are shown in Figure 94 through Figure 102. The primary component generated during the first 3 to 20 hours of each test was carbon dioxide. The carbon dioxide concentration reached as high as 25 mole % for the tests at 75 °C (see Figure 100). Occasionally small amounts of hydrogen were detected at this time (see Figure 95); however, the concentrations were relatively small compared to the carbon dioxide concentrations.

After the initial stage of the test, hydrogen represented a greater fraction of the generated gas. The concentrations appear slightly higher for the non-irradiated tests than the irradiated tests. However, there is enough overlap in the data to suggest the differences are not statistically significant. The highest concentration of hydrogen gas was approximately 5 mole % for the tests performed at 50 °C (see Figure 94). In most cases, the concentrations of both hydrogen and carbon dioxide appeared to decay exponentially with time. The exception was Test 1 at 50 °C, where the hydrogen concentration increased with time, while the carbon dioxide concentration remained relatively constant (see Figure 99). In most cases, the carbon dioxide concentration was greater for the non-irradiated tests compared to the irradiated tests.

It should be noted that only a limited number of gas samples were obtained for the 25 °C tests as a result of the gas chromatograph malfunctioning. In the latter stages of the test, samples were collected by a syringe and then injected into an off-line gas chromatograph. At these later times, the hydrogen concentrations were relatively low for the radiation tests and negligible for the non-irradiated tests (see Figure 97).

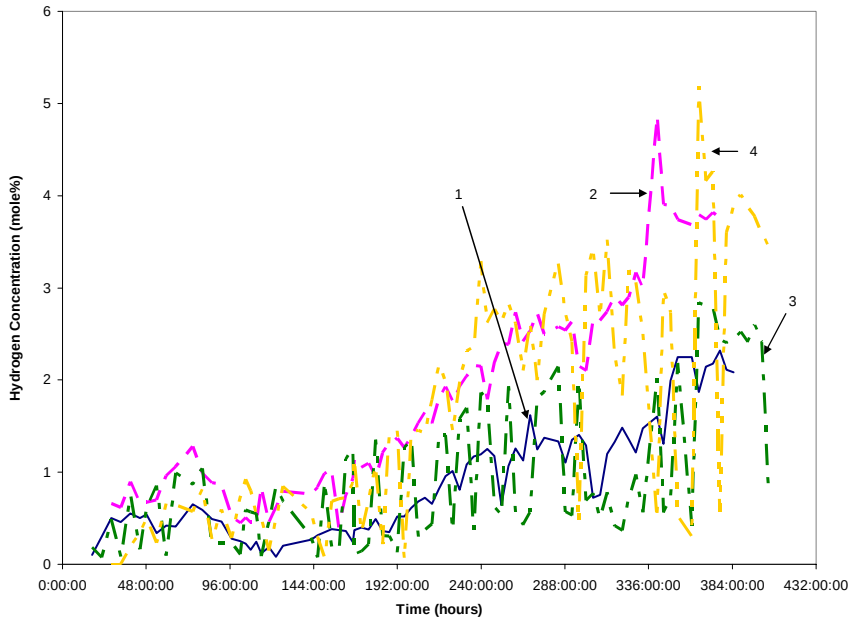

Figure 94. Hydrogen (mol %) vs. time for radiation test at 50 °C after initial 20 h. Containers 1 and 3 were in the radiation source and 2 and 4 were outside.

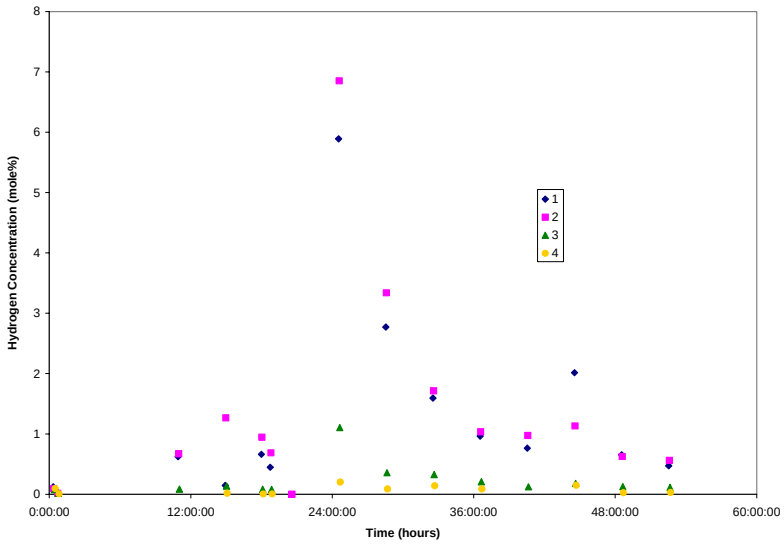

Figure 95. Hydrogen (mol %) vs. time for first 50 h of radiation test at 75 °C. Containers 1 and 3 were in the radiation source and 2 and 4 were outside.

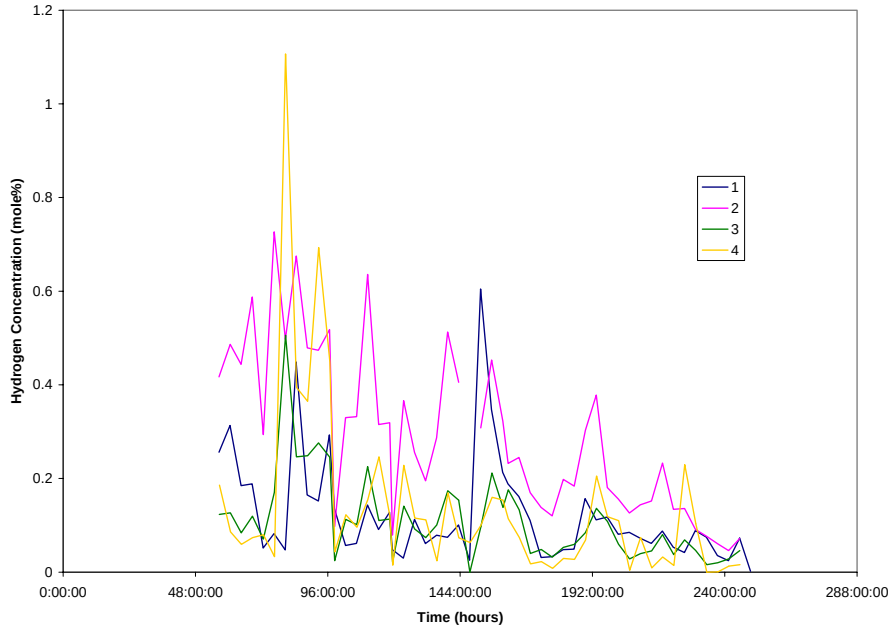

Figure 96. Hydrogen (mol %) vs. time for last 190 h of radiation test at 75 °C. Containers 1 and 3 were in the radiation source and 2 and 4 were outside.

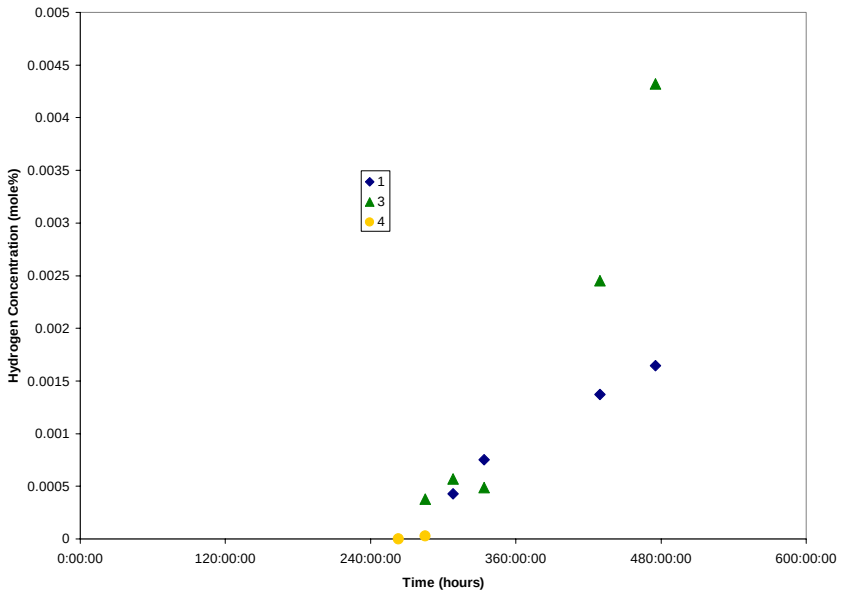

Figure 97. Hydrogen (mol %) vs. time for radiation tests at 25 °C. Containers 1 and 3 were in the radiation source and 2 and 4 were outside.

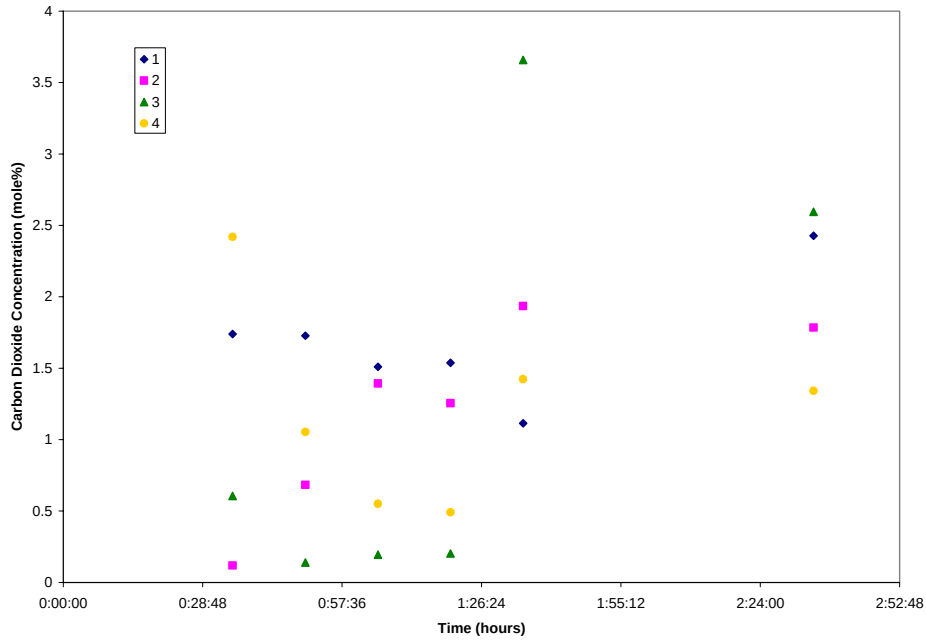

Figure 98. Carbon dioxide (mol %) vs. time for first 3 h of radiation tests at 50 °C. Containers 1 and 3 were in the radiation source and 2 and 4 were outside.

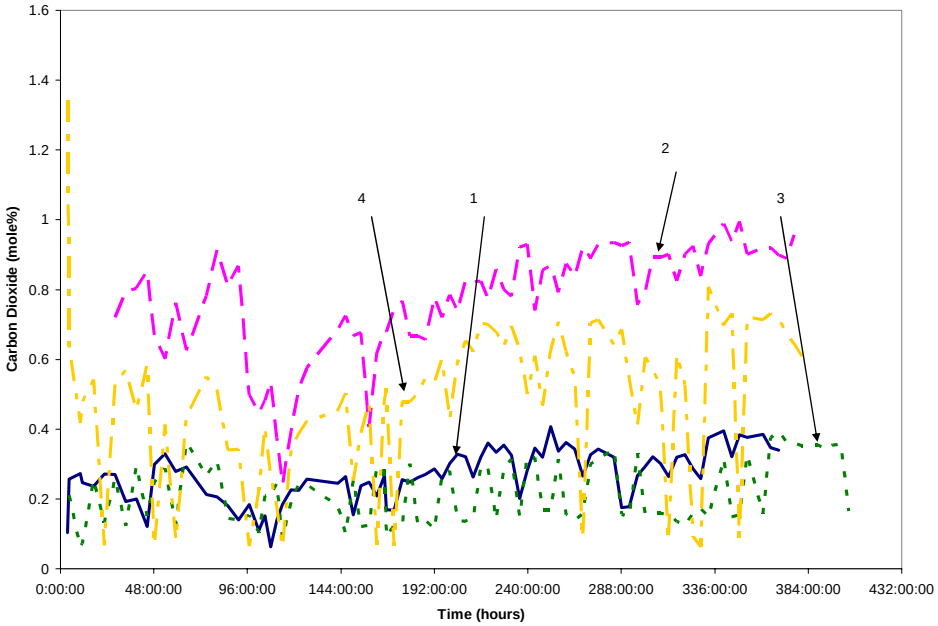

Figure 99. Carbon dioxide (mol %) vs. time after 3 h of radiation tests at 50 °C. Containers 1 and 3 were in the radiation source and 2 and 4 were outside.

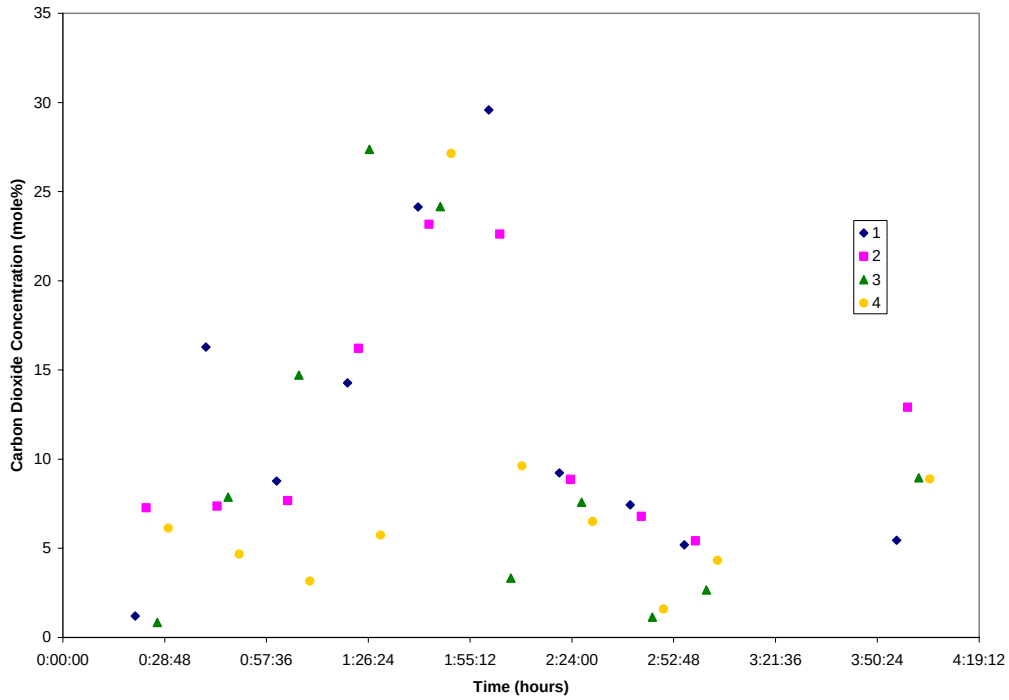

Figure 100. Carbon dioxide (mol %) vs. time for first 4 h of radiation tests at 75 °C. Containers 1 and 3 were in the radiation source and 2 and 4 were outside.

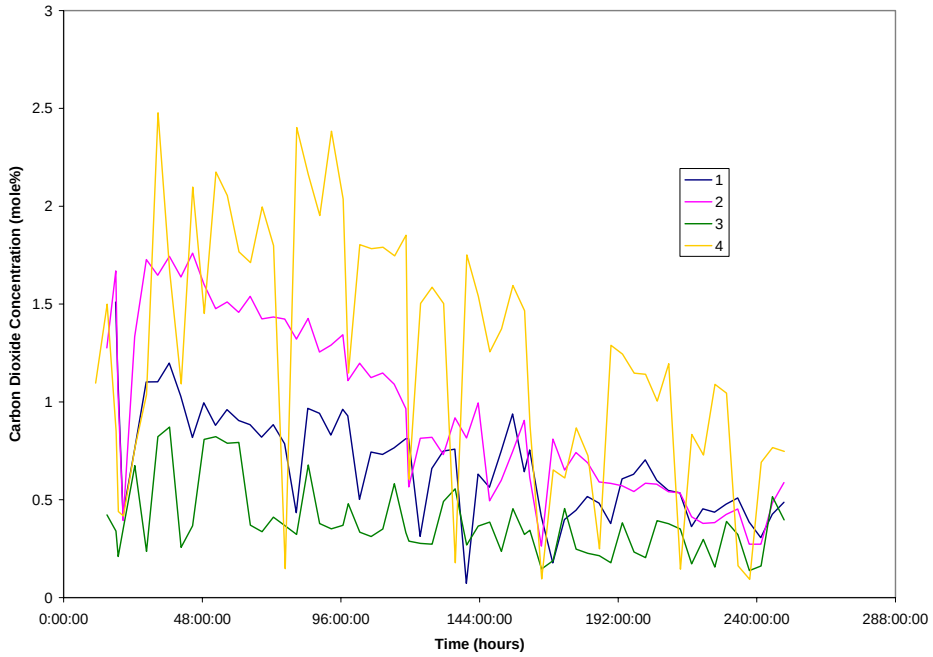

Figure 101. Carbon dioxide (mol %) vs. time for last 246 h of radiation tests at 75 °C. Containers 1 and 3 were in the radiation source and 2 and 4 were outside.

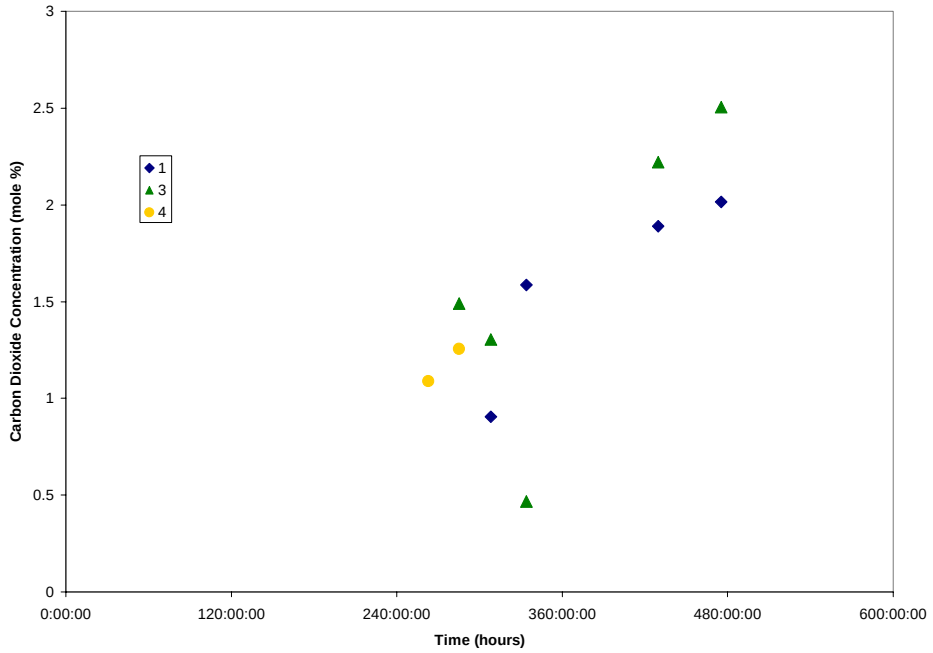

Figure 102. Carbon dioxide (mol %) vs. time for radiation tests at 25 °C. Containers 1 and 3 were in the radiation source and 2 and 4 were outside.

Calculation of Gas Generation Rates

The hydrogen and carbon dioxide gas generation rates were calculated from equations 15 and 16. The gas generation rates as a function of time are shown in Figure 103 through Figure 111. The trends of the plots, not surprisingly, were similar to those for dP/dt.

The maximum carbon dioxide generation rates during the initial stage ranged from 9×10^{-4} moles/hr to 3.5×10^{-3} moles/hour for the 50 °C and 75 °C tests, respectively (see Figure 107 and Figure 109). These rates were not impacted by exposure to the radiation source. Hydrogen generation rates during this time were negligible.

The highest hydrogen generation rates after this initial stage occurred in Container 3 for Test 1 at 50 °C (see Figure 103). In these tests, the hydrogen gas generation rate increased with time until the end of the test. The maximum gas generation rate was approximately 5×10^{-5} moles/hour. A time averaged value of the gas generation rate was approximately 2.5×10^{-5} moles/hour for the irradiated tests and 1×10^{-5} moles/hour for the non-irradiated tests. The maximum hydrogen generation rate for the 75 °C test was approximately 7×10^{-6} moles/hour. A time averaged value of the hydrogen generation rate was approximately 2×10^{-6} moles/hour. It is interesting to note that the hydrogen generation rate did not appear to be influenced by radiation in this case. This rate also decreased with time to approximately 1×10^{-6} moles/hour. The hydrogen generation rates for the latter stages of the 25 °C tests were on the order of 1×10^{-8} moles/hour.

Hydrogen is also generated by radiolysis.[28] Hydrogen generation by radiolysis may be estimated by:

$$D = G * D_{rad} * W * k \qquad \text{equation 17}$$

where D is the gas generation rate in mL/h, G is the G-value total gas yield in molecules/100 ev, D_{rad} is the radiation dose in rad/h, W is the mass of the sample in g, and k is a temperature dependent combination of physical constants in (eV/g)(mL)/(rad-molecules). The dose rate for these tests was 25, 000 rad/h. The G-value is assumed to be 0.43 molecules/100 eV.[29] The mass of the sample was approximately 20 g. The value for k ranged from 2.34×10^{-6} at 25 °C to 2.96×10^{-6} at 75 °C. The expected hydrogen generation rate due to radiolysis was calculated to be approximately 2.2×10^{-7} moles/hour at all the temperatures. This rate indicates that a relatively small fraction of the hydrogen that was generated during the 50 °C and 75 °C radiation tests (i.e., approximately 1% of the time averaged hydrogen generation rate for the 50 °C test and approximately 13% for the same at 75 °C). The hydrogen generation rate measured at the end of the 25 °C test is approximately one order of magnitude less than that expected from radiolysis. However, it is also recognized that the values for the gas generation rates were extremely low at this stage of the test and therefore might exaggerate experimental error.

The carbon dioxide generation rates in the latter stages of the tests remained relatively constant (see Figure 108, Figure 110 and Figure 111). The generation rates appeared to be a slight function of temperature. The highest rates occurred for the 75 C tests (~ 1.2×10^{-5} moles/hour), while for the 50 and 25 °C tests showed lower rates (~8×10^{-6} moles/hour).

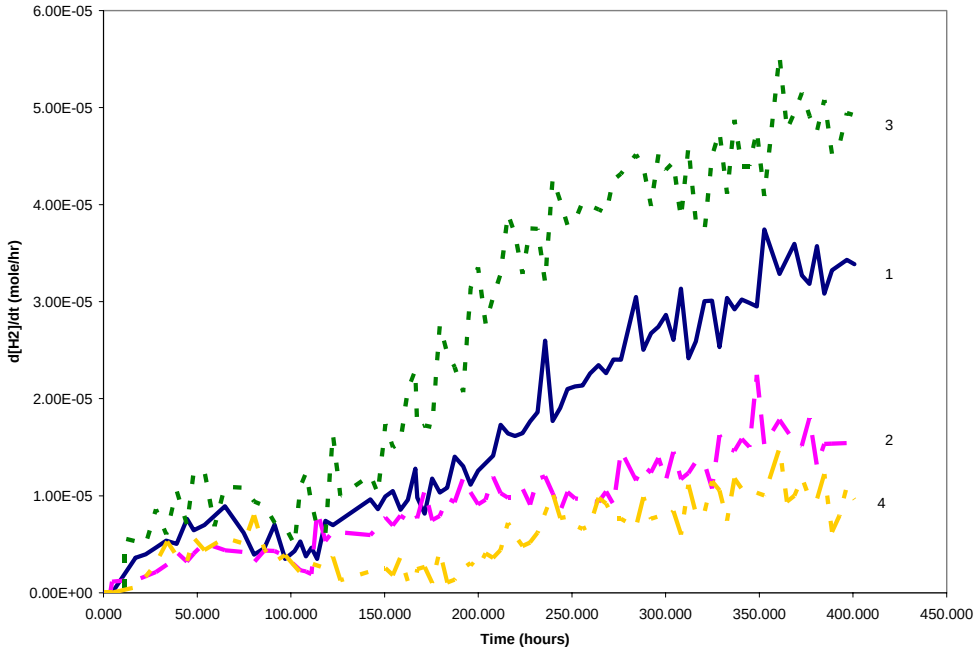

Figure 103. Hydrogen generation rate vs. times for radiation tests at 50 °C. Containers 1 and 3 were in the radiation source and 2 and 4 were outside.

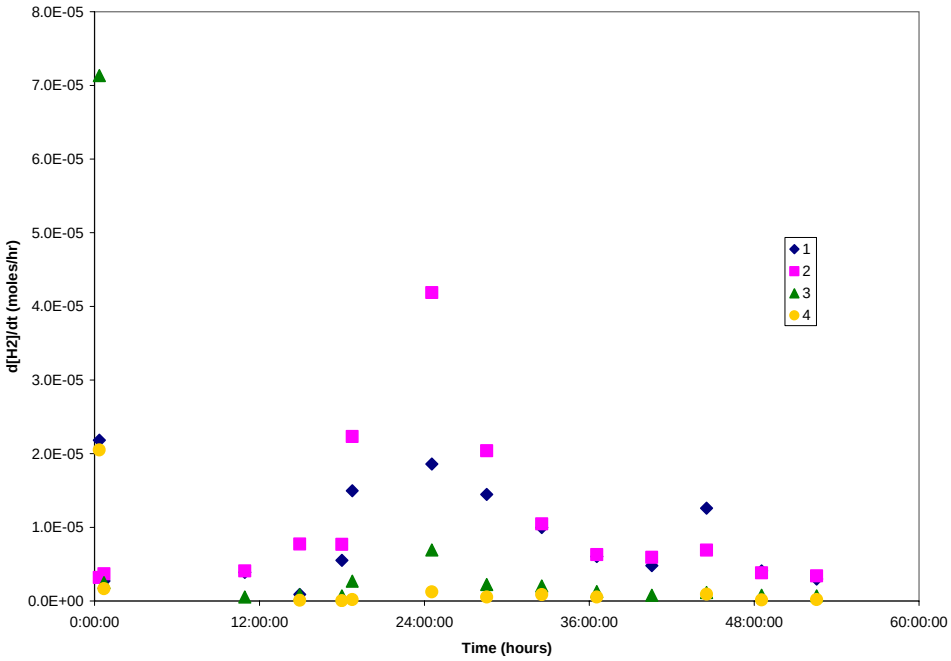

Figure 104. Hydrogen generation rate vs. time for first 50 h of radiation tests at 75 °C. Containers 1 and 3 were in the radiation source and 2 and 4 were outside.

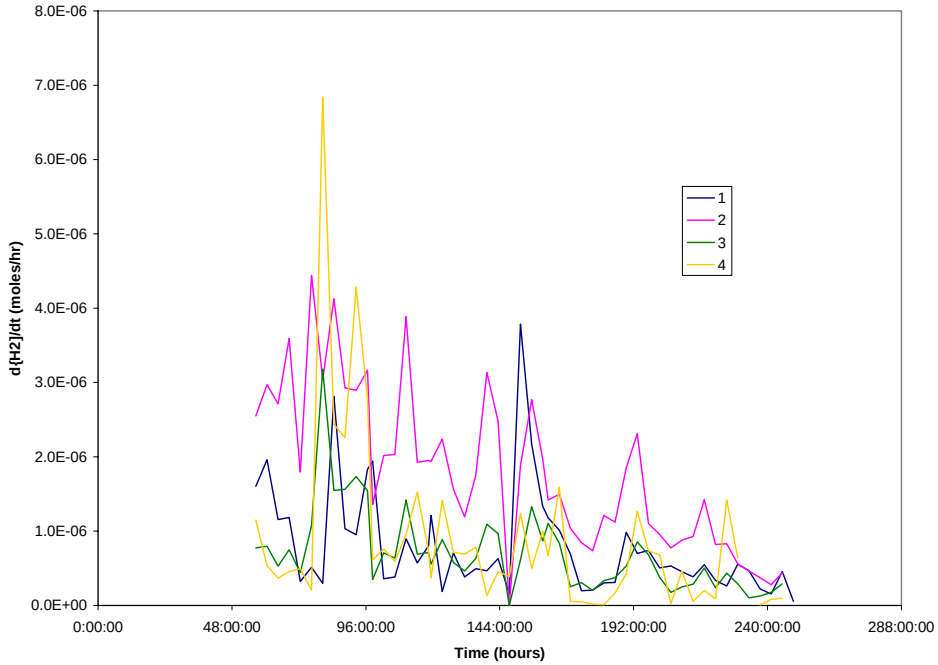

Figure 105. Hydrogen generation rate vs. time for last 190 h of radiation tests at 75 °C. Containers 1 and 3 were in the radiation source and 2 and 4 were outside.

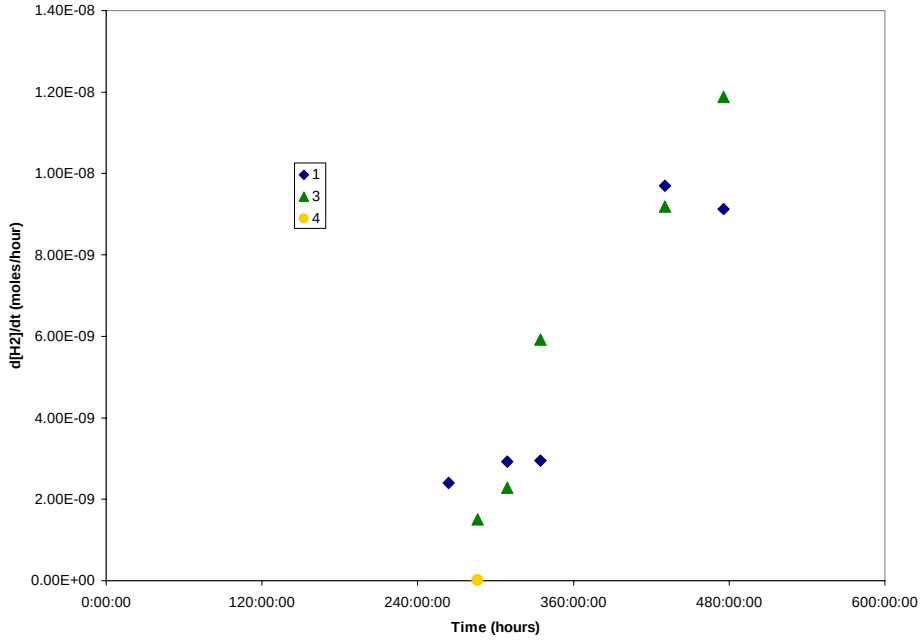

Figure 106. Hydrogen generation rate vs. time for radiation tests at 25 °C. Containers 1 and 3 were in the radiation source and 2 and 4 were outside.

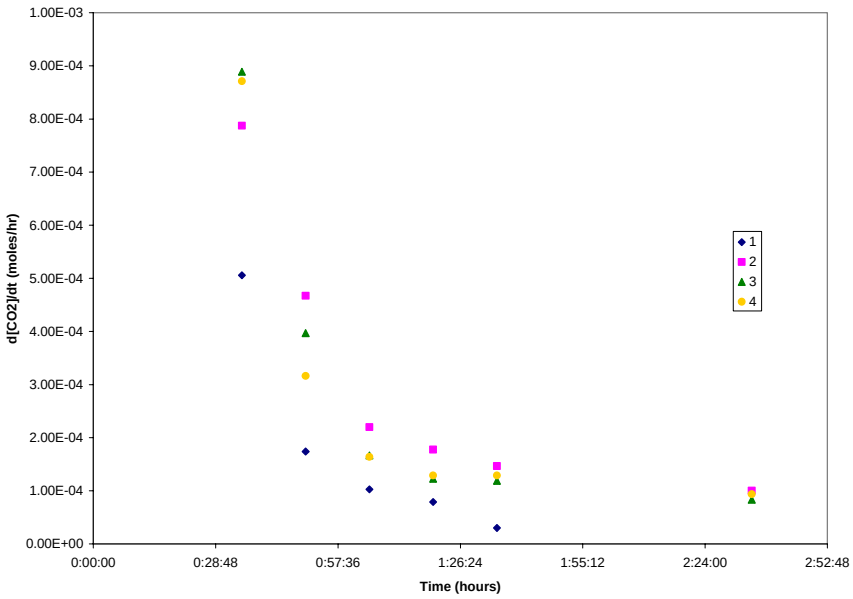

Figure 107. Carbon dioxide generation rate vs. time for the first 3 hours of Test 1 at 50 °C. Containers 1 and 3 were in the radiation source and 2 and 4 were outside.

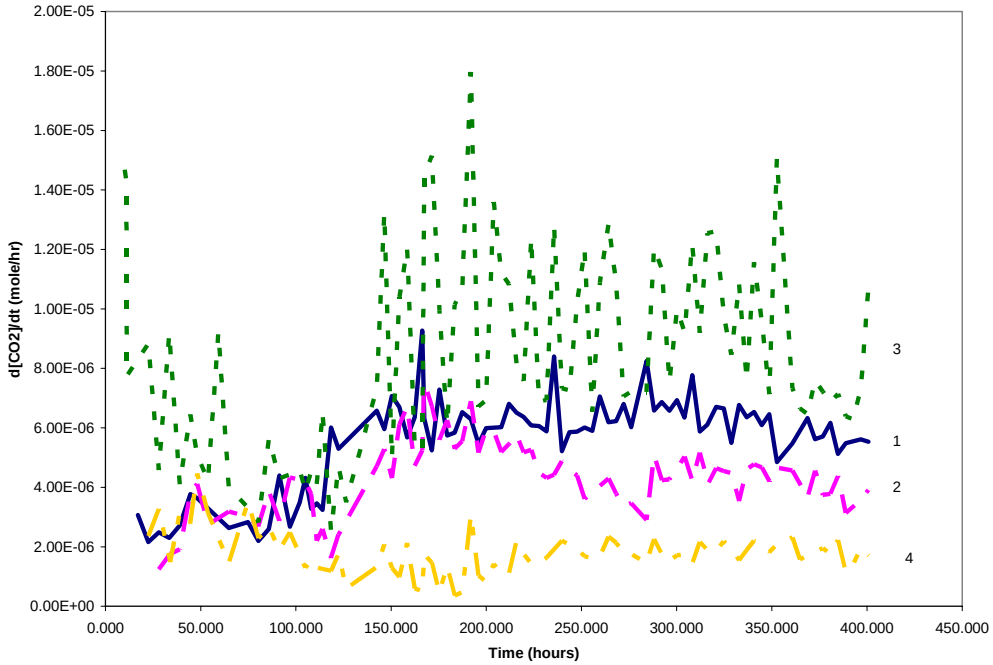

Figure 108. Carbon dioxide generation rate vs. time for radiation tests at 50 °C. Containers 1 and 3 were in the radiation source and 2 and 4 were outside.

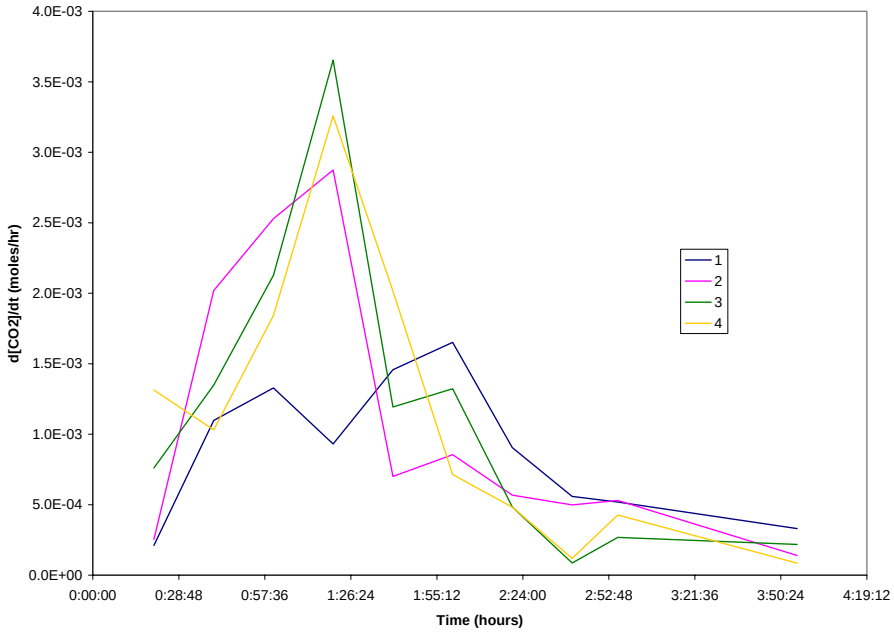

Figure 109. Carbon dioxide generation rate vs. time for first 4 h of radiation tests (75 °C).

Containers 1 and 3 were in the radiation source and 2 and 4 were outside.

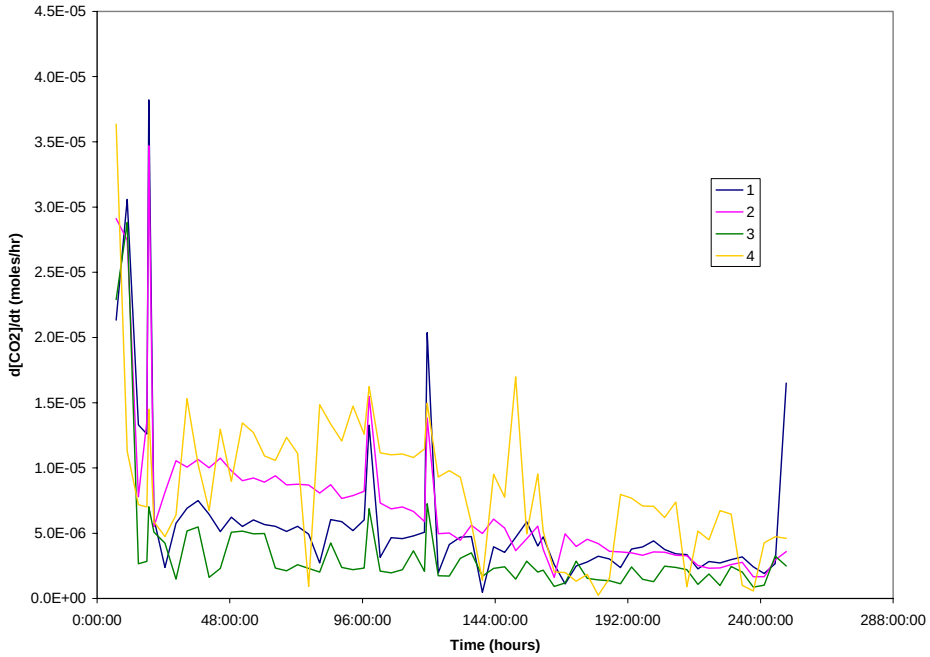

Figure 110. Carbon dioxide generation rate vs. time for last 246 h of radiation tests (75 °C).

Containers 1 and 3 were in the radiation source and 2 and 4 were outside.

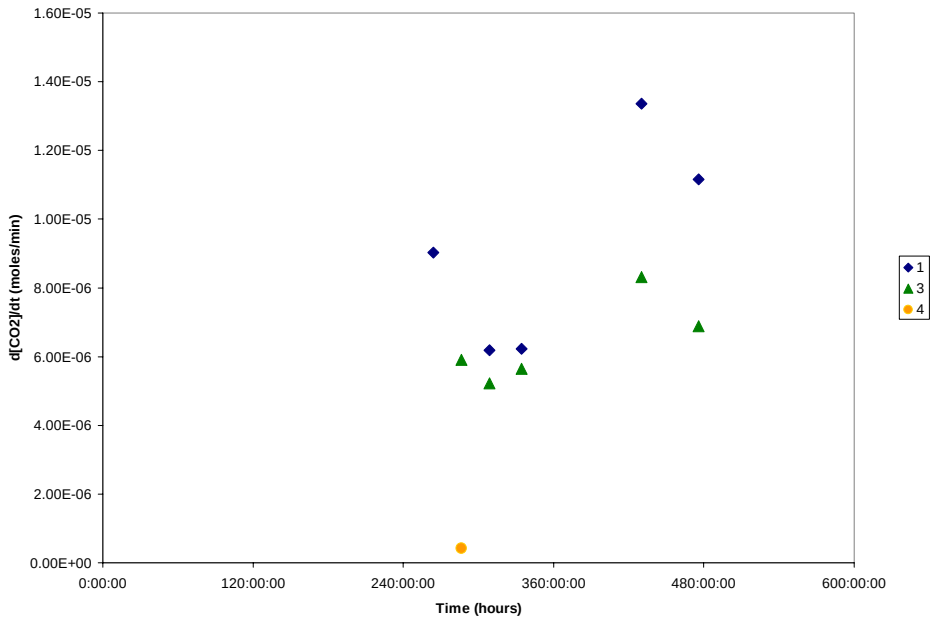

Figure 111. Carbon dioxide generation rate vs. time for radiation tests (25 °C). Containers 1 and 3 were in the radiation source and 2 and 4 were outside.

The observed generation rates indicate that corrosion plays a major role in the generation of hydrogen. Table 33 shows the estimated cumulative volume of hydrogen generated from corrosion assuming equation 10 is valid (i.e., hydrogen evolution is the cathodic reaction). The corrosion rates measured from weight loss measurements on the samples were utilized for this calculation. The table also shows the cumulative volume of hydrogen generated as calculated from the measurements of hydrogen generation rates (see equation 15). This value was calculated by integration of the instantaneous hydrogen generation rate curves. For the 50 °C test, the calculated cumulative volumes of hydrogen generated are in good agreement. This result indicates that corrosion was responsible for hydrogen evolution during this test. Thus it is likely that oxygen availability in the solution was limited and that an insignificant amount of ferric ion had dissolved into solution. The results from electrochemical tests with oxalic acid and Tank 8F sludge slurry suggest a similar interpretation.

For the 50 °C irradiated containers, the volume of hydrogen calculated from the hydrogen generation measurements is greater than that calculated from hydrogen evolution. The higher value is likely due to hydrogen evolved from radiolysis of the oxalic acid solution. Therefore, recombination of the hydrogen with oxygen in a gamma field does not appear to have occurred.[30]

The agreement between the values for cumulative volume is not as good for 50 °C and 75 °C. In this case the volume calculated from the corrosion rate is significantly higher than that calculated from the hydrogen generation measurements. This difference indicates that another cathodic reaction was part of the corrosion mechanism. Both tests used Tank 5F simulated sludge and hence chemical composition does not account for the variance. In parallel electrochemical tests, Wiersma observed that the presence of Tank 5F sludge simulant in solution provided sufficient ferric ion to participate in the cathodic reaction. Initially hydrogen may have evolved due to de-

aerated conditions in the container, however, once the sludge dissolved into the solution, ferric ion reduction became dominant.

Table 33. Estimation of hydrogen generation from corrosion rate measurements.

Test	Container	Surface Area (ft^2)	Corrosion Rate from weight loss measurements (mpy)	Cumulative Hydrogen Generated as Calculated by equation 2 (cc^3)	Cumulative Hydrogen Generated as Calculated from the Hydrogen Generation Rate Measurements (cc^3)
1	1 (irradiated)	0.0083	37.6	129	170
	2	0.0085	29.7	104	105
	3 (irradiated)	0.0081	59.6	193	252
	4	0.0084	21.4	73	60
2	1 (irradiated)	0.0084	10.7	32	14
	2	0.0083	12.9	39	25
	3 (irradiated)	0.0078	10.6	29	11
	4	0.0080	12.1	35	9
3	1 (irradiated)	0.0043	9.8	19	0.03
	2	0.0086	15.9	48	NA
	3 (irradiated)	0.0081	9.1	33	0.04
	4	0.0043	12.3	30	0.0002

Post-test Visual Examination of Coupons

The coupon and container contents were examined following the tests. Figure 112 is representative of the appearance of the coupons at all test conditions. The coupon was covered with a yellowish green precipitate. The amount of solids remaining on the specimen was approximately the same for each test. This precipitate could be removed by wire brush and subsequent cleaning with Clarke's solution. The precipitate was very difficult to remove from the coupons tested at 75 °C, which suggests a very tenacious film. A significant amount of yellowish green precipitate was suspended in the solution and observed at the bottom of the container. These solids were identified by x-ray diffraction as humboldtine. Interestingly, the solids contained no sodium ferrous oxalate, the orthorhombic structure. Given that the tests occurred in a dark environment, the photochemical reaction that forms this species was inactive. Therefore, carbon dioxide evolution during these tests was due to reactions within the sludge and radiolysis of the oxalic acid. No sludge solids were observed in the test container.

Once the precipitate was removed, the surface had a roughened appearance typical of general corrosion attack (see Figure 112). Some pitting of the surface was also observed.

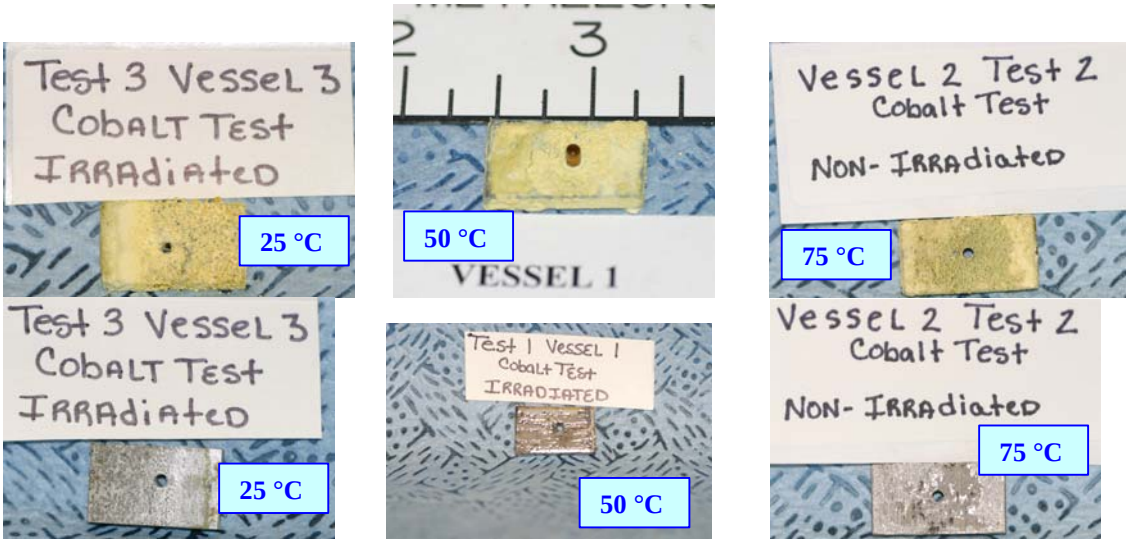

Figure 112. Representative coupons from irradiated corrosion tests.

Top row coupons were photographed at the completion of the test, while the bottom row coupons were photographed after the coupon was cleaned and prior to weighing.

Post-test analysis was also performed on the test solutions. Table 34 presents the results of these analyses. Significant differences in the compositions for Test 1 versus the other two tests were observed. These likely reflect the differences in the initial sludge slurry that was utilized (i.e., Tank 8F for Test 1 and Tank 5F for Tests 2 and 3). The difference in the iron concentrations are initially surprising given the higher corrosion rates observed for Test 1. However, the reaction that precipitates the ferrous oxalate involves the ferrous ion that was generated from corrosion and therefore these results may not be as incongruous as initially thought.

Comparison of Gas Generated from Simulant Demonstration, Actual Waste Test, and Radiation Tests

Table 35 shows the gas generation during each of the tests. Since CO_2 productions accounts for most of the gas generated, we normalized the gas generation by the oxalic acid volume in the given test. After performing this normalization, the results agree within an order of magnitude.

Table 34. Results of post-test solution analyses for irradiated tests (ppm).

	Test 1 Container 1	Test 1 Container 3	Test 2[a] Container 1	Test 2[a] Container 3	Test 3 Container 1	Test 3 Container 3
pH	1	1	1	1	0.845	0.835
Fluoride	14	12	51	44	57	53
Formate			512	501		
Chloride	51	18	251	75	48	66
Nitrate	79	32	153	283	442	608
Sulfate	123	< 50	701	905	460	397
Oxalate	47,200	29,100	99,100	103,000	56,600	60,500
Aluminum	277	295	945	1380	521	456
Calcium	31	16	108	262	55	55
Iron	306	248	3440	4950	1420	876
Manganese	13	11	141	298	6	19
Sodium	1190	1260	3870	4280	4070	3540
Sulfur	41	44	222	332	169	132
Silicon	66	101	113	152	11	15
Zirconium	< 0.07	0.07	97	117	41	39

[a] – Due to the limited amount of sample, Analytical Development reported these values as qualitative

Table 35. Gas generation during chemical cleaning tests.

Test	Purge Gas (cm^3)	Gas Generation He correction (cm^3)	Gas Generation N_2 correction (cm^3)	Gas Volume Generated per unit volume Oxalic Acid
Simulant: 50 °C, mixed	416,000	-36,000	55,000	7.2
Simulant: 75 °C, mixed	246,000	82,000	87,000	11.4
Simulant: 25 °C, mixed	339,000	21,000	26,000	3.4
Simulant: 50 °C, unmixed	345,000	115,000	109,000	14.2
Simulant: 75 °C, unmixed	229,000	119,000	79,000	10.3
Simulant: 25 °C, unmixed	248,000	13,000	26,000	3.4
Actual 50 °C	233,000	N/A	2,000	13.8
Actual 75 °C	114,000	N/A	300	2.1
Radiation 50 °C	N/A	N/A	218-288	14.5 – 19.2
Radiation 75 °C	N/A	N/A	170 - 192	9.4 – 10.7
Radiation 25 °C	N/A	N/A	103 - 189	5.7 – 10.5

Table 36 shows the hydrogen generation during each of the tests. Since the hydrogen is produced by a reaction between the oxalic acid and the sludge and by a reaction between the oxalic acid and the metal coupons, we normalized the hydrogen generation rates by each of these parameters. When normalizing by sludge mass, the actual waste and simulant tests results agree well. The radiation tests show larger volumes of gas being generated.

Table 36. Hydrogen generation during chemical cleaning tests.

Test	Purge Gas (cm^3)	H_2 Generation N_2 correction (cm^3)	H_2 Generation corrected for sludge (ft^3/kg)	H_2 Generation corrected for metal surface area (ft^3/ft^2)
Simulant – 50 °C mixed	216,000	1.2	0.00023	0.00018
Simulant – 75 °C mixed	246,000	1.8	0.00033	0.00028
Simulant – 25 °C mixed	339,000	1.5	0.00028	0.0.00023
Simulant – 50 °C unmixed	345,000	6.2	0.00120	0.00100
Simulant – 75 °C unmixed	229,000	2.7	0.00050	0.00040
Simulant – 25 °C unmixed	229,000	3.3	0.00061	0.00051
Actual 50 °C	233,000	0.067	0.00019	0.00007
Actual 75 °C	114,000	0.004	0.00005	0.00002
Radiation – 50 °C	N/A	170 - 253	40 - 60	0.72 – 1.07
Radiation – 75 °C	N/A	11 - 14	1.9 – 2.5	0.047 – 0.059
Radiation – 25 °C	N/A	0.03 – 0.04	0.0053 – 0.0071	0.00013 – 0.00017

Based on the test results and scaling the hydrogen generation with metal surface area (8940 ft^2), we calculated the expected hydrogen generation rates in Tank 5F as shown in Table 38. The hydrogen generation from the radiation tests does not agree well with that obtained from the other experiments, especially at 50 °C and 75 °C. The 50 °C radiation experiment used the Tank 8F washed sludge. Hence, the nitrate and nitrite scavengers are lower and one expects increased gas from radiolysis. However, this variance can not account for the marked increase in hydrogen observed. The most striking difference in test methodology for the radiation tests involved the use of a sealed system periodically purged with argon and then evacuated before backfilling with air. We speculate that the repeated evacuation led to thorough de-gassing of the liquid and removal of oxygen from the aqueous reaction. Under such anoxic conditions, passivating iron oxide films can not form and the reaction pathways change to enhance hydrogen generation. The post mortem analysis of the corrosion coupons for this experiment support this interpretation since iron oxides such as goethite ($HFeO_2$) and lepidocrocite (FeO(OH)) were not observed in these deposits. As such, we believe the radiation tests do not well mimic the planned operations and recommend not using this data for projecting to planned operations.

To assess this line of reasoning, we compared hydrogen generation rates measured previously in an anoxic environment compared to the tests performed in the cobalt source. The earlier tests exposed carbon steel in an 8 wt % oxalic acid solution at 50 °C that was de-aerated with argon. The tests used coupons covered with iron oxides. Table 37 compares the instantaneous corrosion rates after 1 week from the earlier tests with those measured from the present investigation. The table also shows the rate after two weeks from this study. After 1 week the

hydrogen generation rates are within the same order of magnitude. The rates from the present studies are lower as expected given that the vessels were vented to the atmosphere and therefore exposed to oxygen periodically. During the second week of these studies, however, the irradiated containers were vented to the atmosphere on a less frequent basis, thus adding less available oxygen. During the second week the hydrogen generation rate increased such that the difference between the two tests closed to within a factor of 2 to 6. This comparison suggests that conditions in the containers were approaching anoxic.

Table 37. Comparison of hydrogen generation rates in an anoxic environment with rates determined from the radiation tests.

Test	Hydrogen Generation Rate after 1 Week (moles/h)	Hydrogen Generation Rate after 1 Week (moles/h)
Average of two tests in an Anoxic Environment	7.7×10^{-5}	-
Average of Vessels 1 and 3 from this investigation.	1.6×10^{-5}	3.9×10^{-5}
Average of Vessels 2 an 4 from this investigation.	7.0×10^{-6}	1.2×10^{-5}

We recommend additional studies to confirm this interpretation and to better comprehend the role of oxygen in this system. Analysis of the corrosion coupons from the actual waste demonstration could provide additional confirmation of the presence of protective oxide films during the planned cleaning process and confirmation of similar analyses from the demonstrations with simulated waste. Also, additional experiments – simplified in nature – to explicitly study the role of oxygen on the reactions and to quantify the oxygen transfer rates in these slurries would enhance process understanding.

Since most of the gas generated in the process demonstrations and actual waste experiments was carbon dioxide and the carbon dioxide is produced in reactions with oxalate, we scaled the gas generation with oxalic acid. Based upon the test results and the expected operating conditions in Tank 5F (100,000 gallons oxalic acid), we calculate the gas generation during chemical cleaning shown in Table 39.

Table 40 shows the maximum hydrogen generation rate measured during each of the simulant demonstrations and actual waste tests. At 50 °C and 75 °C (mixed), no hydrogen was detected, so the corresponding generation rate is calculated based on the hydrogen in the gas being equal to the minimum concentration of hydrogen measured during the corresponding unmixed test. The table shows the maximum generation calculated with no correction, with the helium correction, and with the nitrogen correction. The table also shows the generation rate normalized by carbon steel coupon surface area, and the maximum hydrogen generation rate in Tank 5F based on the surface area of carbon steel (8940 ft^3).

Table 38. Projected hydrogen generation in Tank 5F based on experiments.

Temperature (°C)	Hydrogen generation (ft^3 ±100%)	
	Mixed	Unmixed
Process Demonstrations		
25	1.7	4.6
50	<1.6*	8.9
75	<2.5*	3.6
Actual Waste Experiments		
50	0.6	
75	0.15	
Radiation Tests		
25		1.5
50		9600
75		530

* based on detection limit for on-line gas analyses

Table 39. Projected total gas generation in Tank 5F based on experiments.

Temperature (°C)	Gas generation (ft^3 ±10%)	
	Mixed	Unmixed
Process Demonstrations		
25	45,000	45,000
50	96,000	189,000
75	152,000	138,000
Actual Waste Experiments		
50	184,000	
75	28,000	
Radiation Tests		
25		140,000
50		257,000
75		143,000

Table 40. Maximum hydrogen generation rates measured.

Test	Maximum Hydrogen without correction (cm^3/min)	Maximum Hydrogen – He correction (cm^3/min)	Maximum Hydrogen – N_2 correction (cm^3/min)	Maximum Hydrogen – N_2 correction (ft^3/min) per ft^2 metal	Maximum Hydrogen Tank 5 (ft^3/min)
Simulant Demonstrations					
50 °C mixed	0.00008	0.00021	0.00012	1.8×10^{-8}	0.00016
75 °C mixed	0.00009	0.0051	0.00022	3.4×10^{-8}	0.00030
25 °C mixed	0.0007	0.0007	0.0008	1.2×10^{-7}	0.0011
50 °C unmixed	0.0029	0.0037	0.0038	5.8×10^{-7}	0.0052
75 °C unmixed	0.0014	0.0015	0.0014	2.2×10^{-7}	0.0020
25 °C unmixed	0.0014	0.0085	0.0016	2.5×10^{-7}	0.0022
Actual Waste Tests					
50 °C	0.0008	N/A	0.0008	3.1×10^{-6}	0.028
75 °C	0.00005	N/A	0.00005	1.9×10^{-7}	0.0017

Table 41 shows the maximum gas generation rate measured during each of the simulant demonstrations and actual waste tests. The table shows the maximum generation calculated with the helium correction and the volume of oxalic acid added and the maximum hydrogen generation rate in Tank 5F based on the volume of oxalic acid to be added (13,400 ft^3).

Table 41. Maximum total gas generation rates measured.

Test	Maximum Gas – He correction (cm^3/min)	Maximum Gas – N_2 correction (cm^3/min)	Maximum Gas – N_2 correction (ft^3/min) per ft^3 Oxalic Acid	Maximum Gas generation Rate Tank 5F (ft^3/min)
Simulant Demonstrations				
50 °C mixed	17.8	18.3	0.0024	32
75 °C mixed	908	23.6	0.0031	41
25 °C mixed	6.2	5.1	0.0007	8.9
50 °C unmixed	14.4	13.2	0.0017	23
75 °C unmixed	695	26.9	0.0035	47
25 °C unmixed	119	3.6	0.0005	6.3
Actual Waste Experiments				
50 °C	N/A	7.1	0.049	655
75 °C	N/A	3.8	0.026	350

ACKNOWLEDGEMENTS

The authors thank Russ Eibling for developing the recipes for the simulated sludge. Holly Hall played a key role in coordinating the sludge synthesis work as well as monitoring the daily activities in the laboratory. Kofi Adu-Wusu assisted greatly in the original experimental design for the scaled-demonstrations and developed recipes for the simulated supernate. Gary Dobos did an excellent job in fabricating the glassware for the experiments on a timely schedule including adjustments in the designs as work progressed. Tim Steeper devised the automated data collection system for tests in the radiation environment and Vernon Bush developed the software. Chris Beam and Greg Creech supervised the installation and operation of the equipment. Zane Nelson, Thaddeus Reown, and Angela Bowser assisted in the post-test examination of the corrosion coupons. Tommy Sessions provided analysis for gas samples collected by syringe during the radiation tests. John Mickalonis assisted with the electrochemical measurements in the absence of one of the authors. Tracy Murphy performed many of the electrochemical measurements and helped prepare the corrosion coupons for testing. Chris Martino, David Hobbs, and Phil Zapp provided review of portions of the report and confirmed the many calculation spreadsheets.

The Analytical Development organization in SRNL provided exceptional support on an aggressive schedule. Mark Barnes, Frank Pennebaker and Leigh Brown monitored progress and overcame numerous obstacles to complete the work in a timely fashion. June Hart, Mike Summers, Mark Jones, Robert Ray and Curtis Johnson – as well as a host of others – performed the numerous analyses.

Sammie McDuffie and Kim Wyszinski provided the bulk of the technician support for the scaled-demonstrations over a period of about 5 months. The work required extensive weekend support as well as late hours each night. Mr. McDuffie proved essential through all stages of the program and we are indebted to his professional dedication.

APPENDIX

Dissolution Behavior during Process Demonstrations

The following figures show the concentration of major elements in the supernate during the oxalic acid cleaning demonstrations using simulated Tank 5F waste.

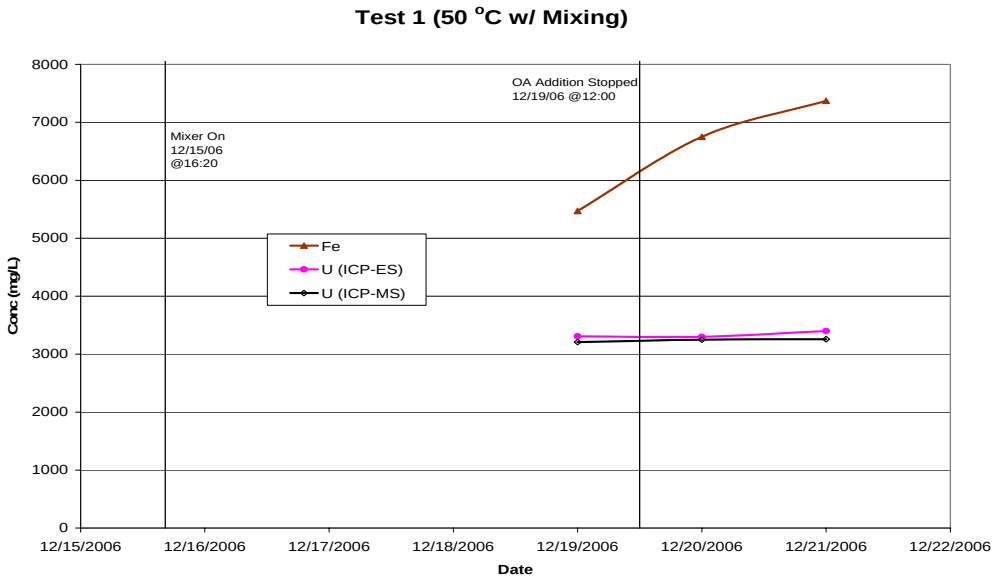

Figure 113. Dissolution kinetics for iron and uranium: 50 °C, mixed.

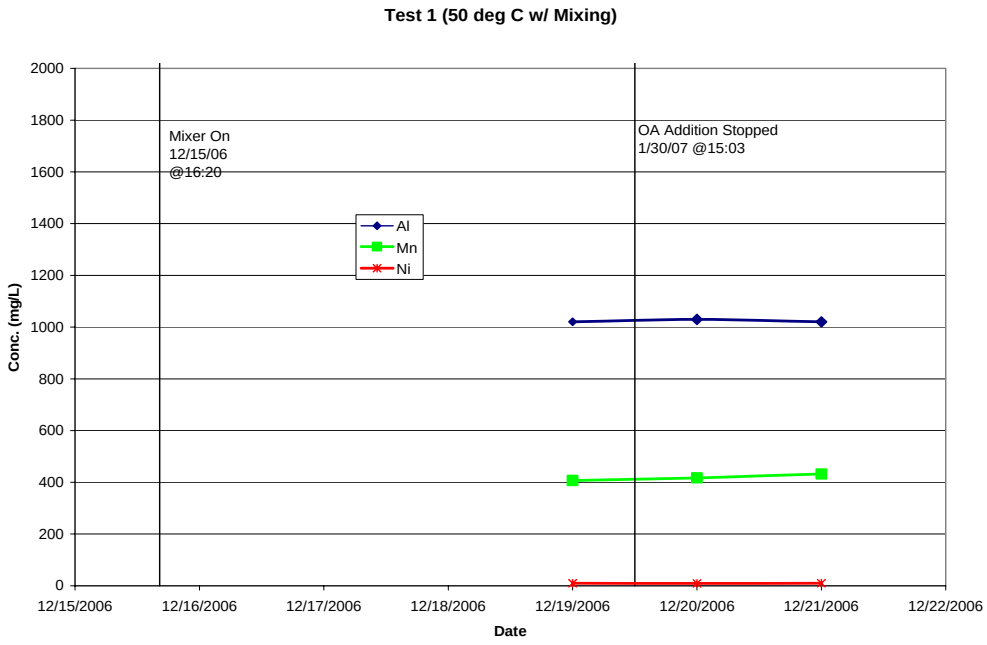

Figure 114. Dissolution kinetics for aluminum, manganese and nickel: 50 °C, mixed.

Figure 115. Dissolution kinetics for aluminum, manganese and nickel: 75 °C, mixed.

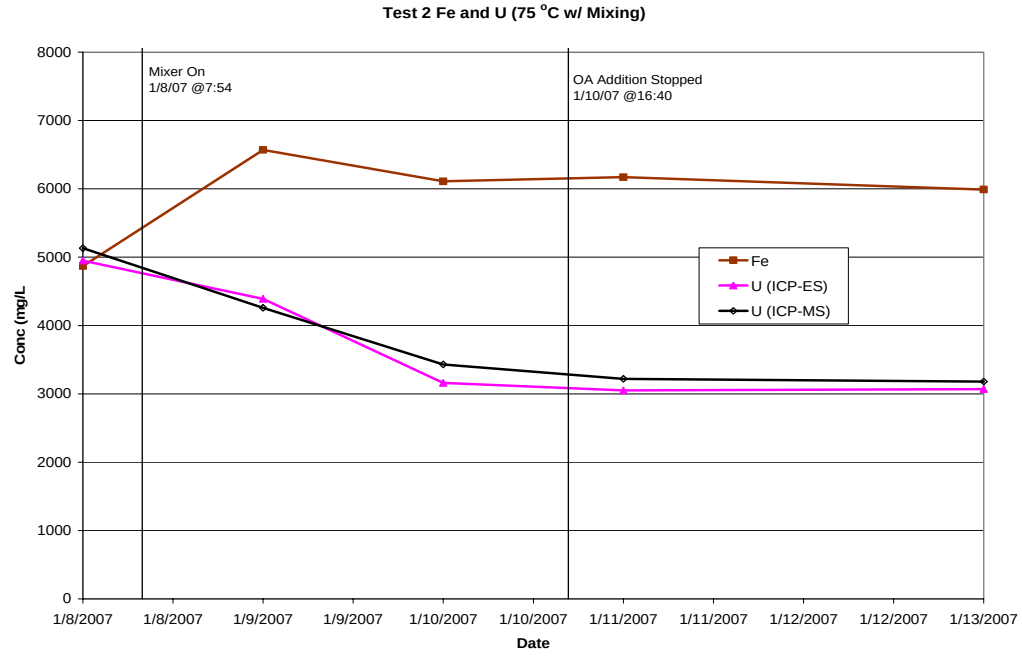

Figure 116. Dissolution kinetics for iron and uranium: 75 °C, mixed.

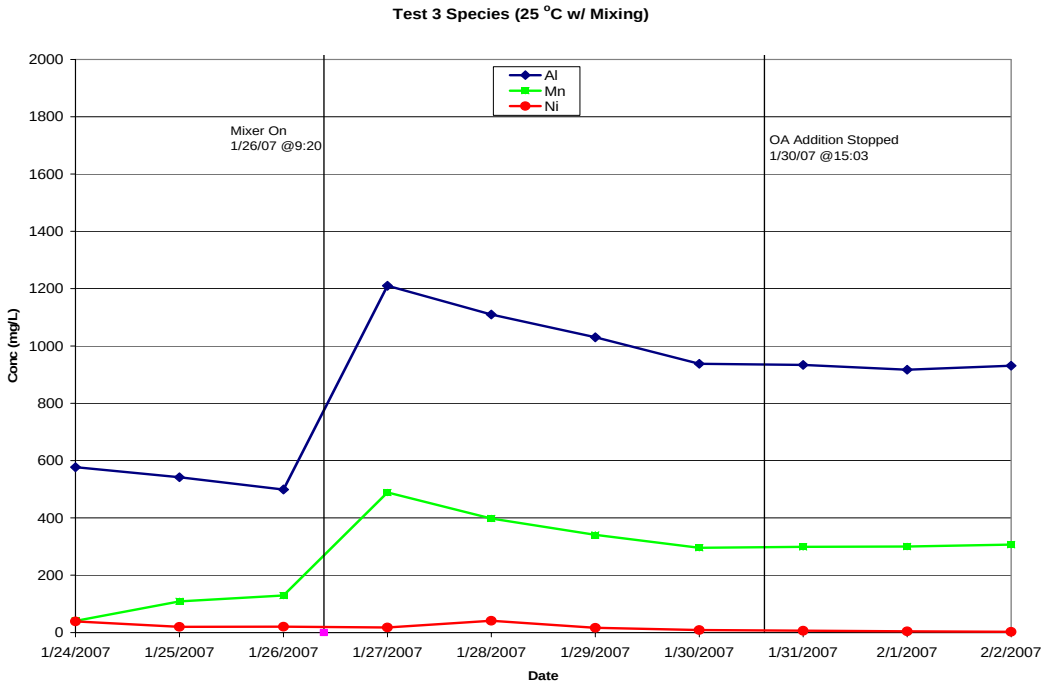

Figure 117. Dissolution kinetics for aluminum, manganese and nickel: 25 °C, mixed.

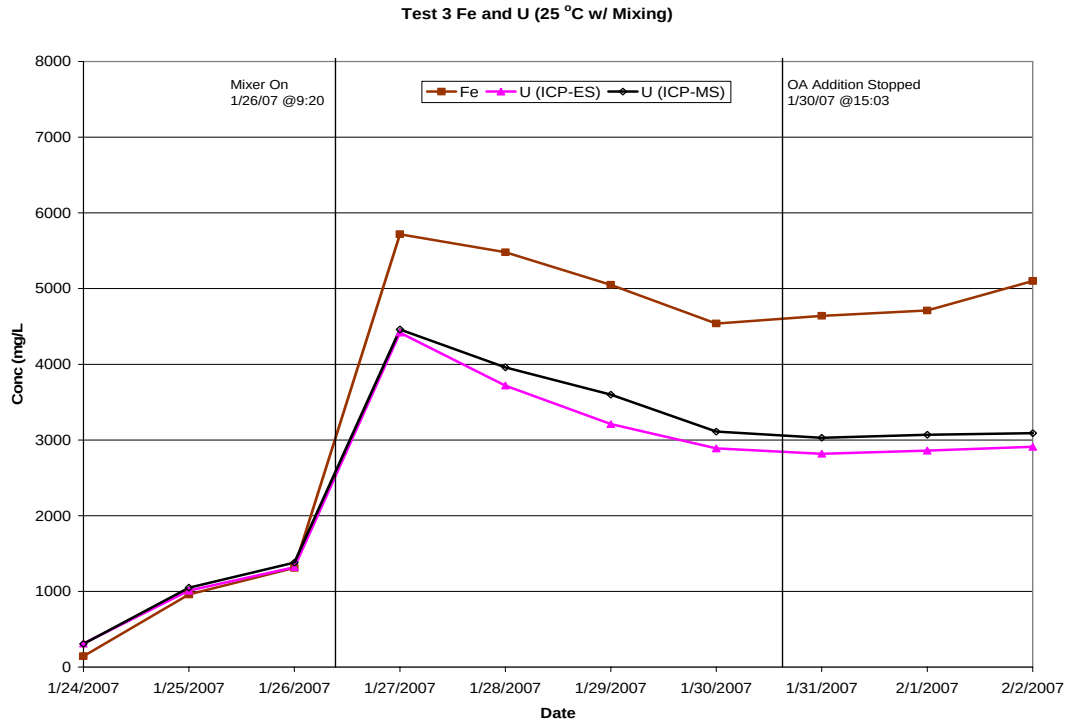

Figure 118. Dissolution kinetics for iron and uranium: 25 °C, mixed.

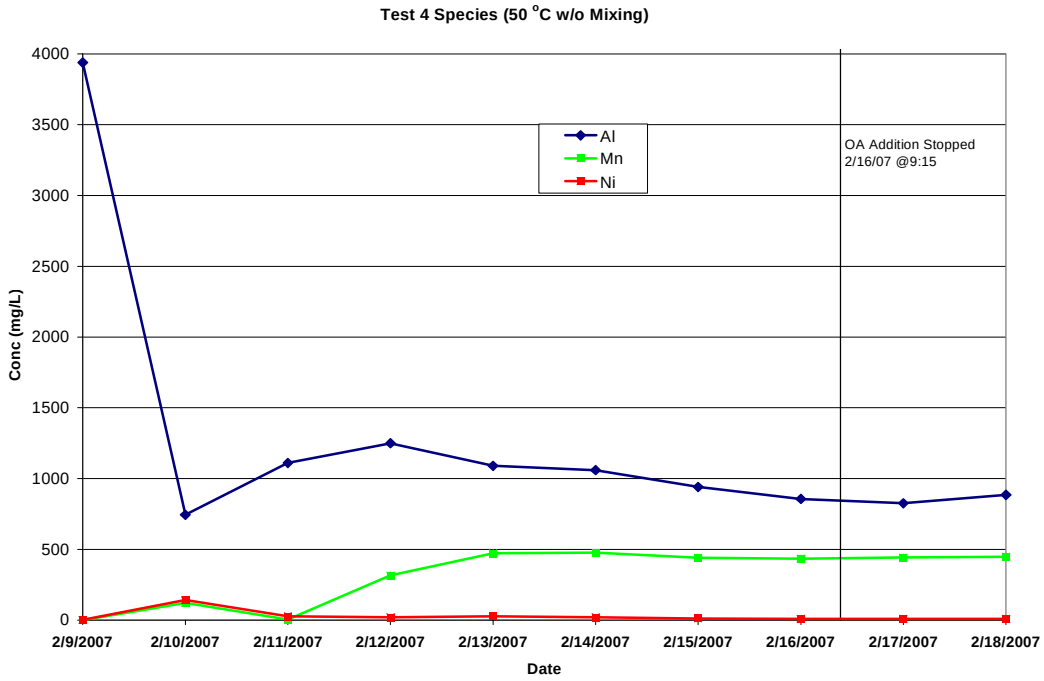

Figure 119. Dissolution kinetics for aluminum, manganese and nickel: 50 °C, unmixed.

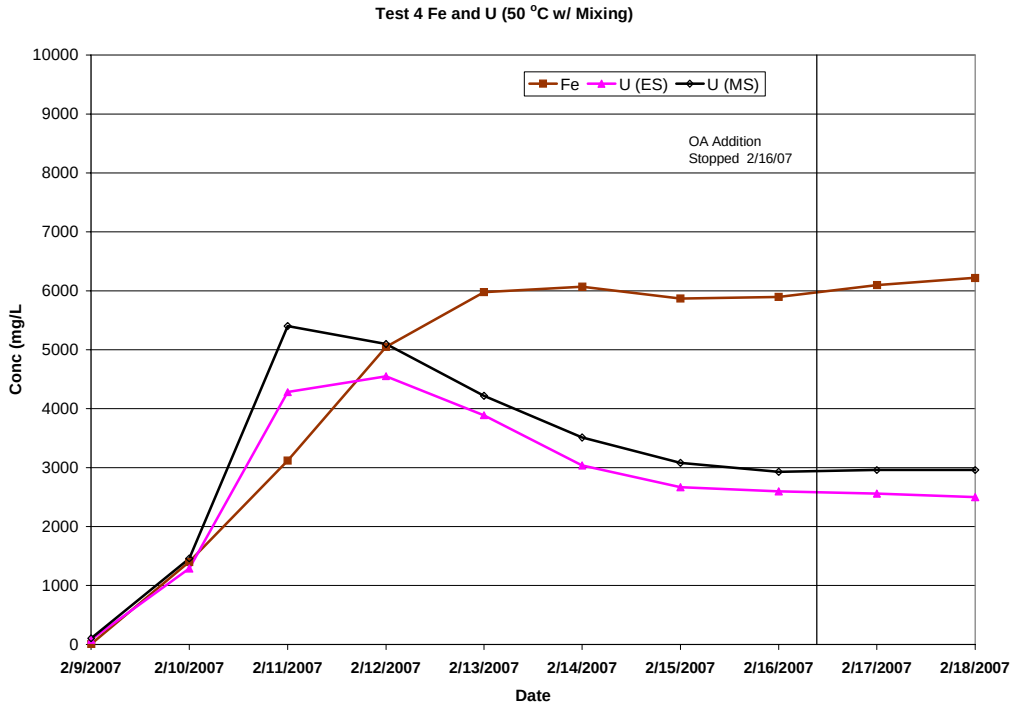

Figure 120. Dissolution kinetics for iron and uranium: 50 °C, mixed.

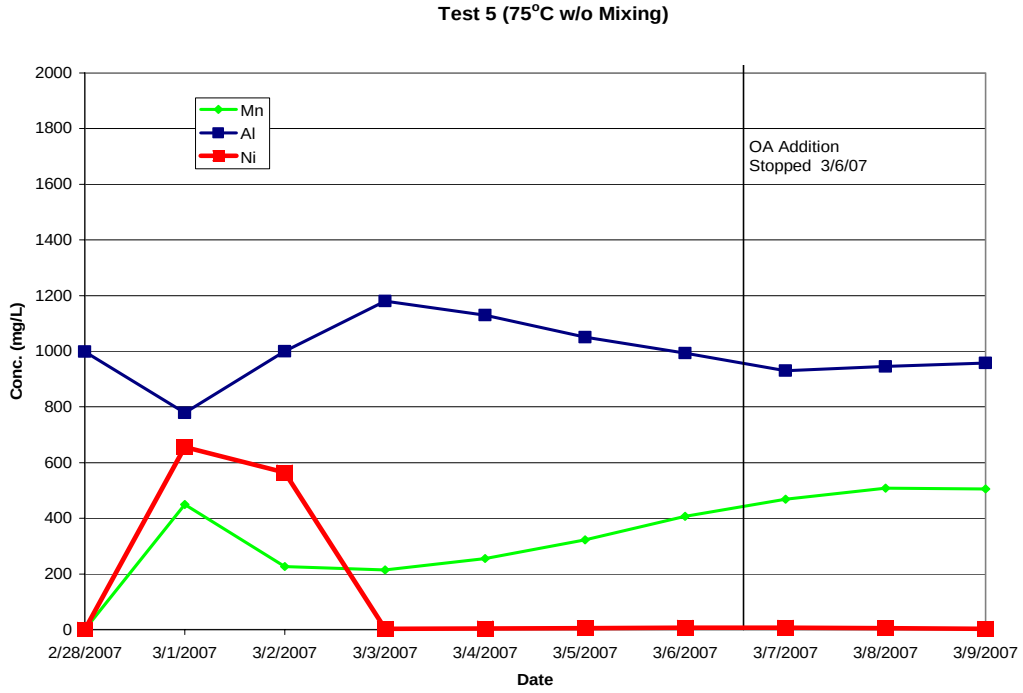

Figure 121. Dissolution kinetics for aluminum, manganese and nickel: 75 °C, unmixed.

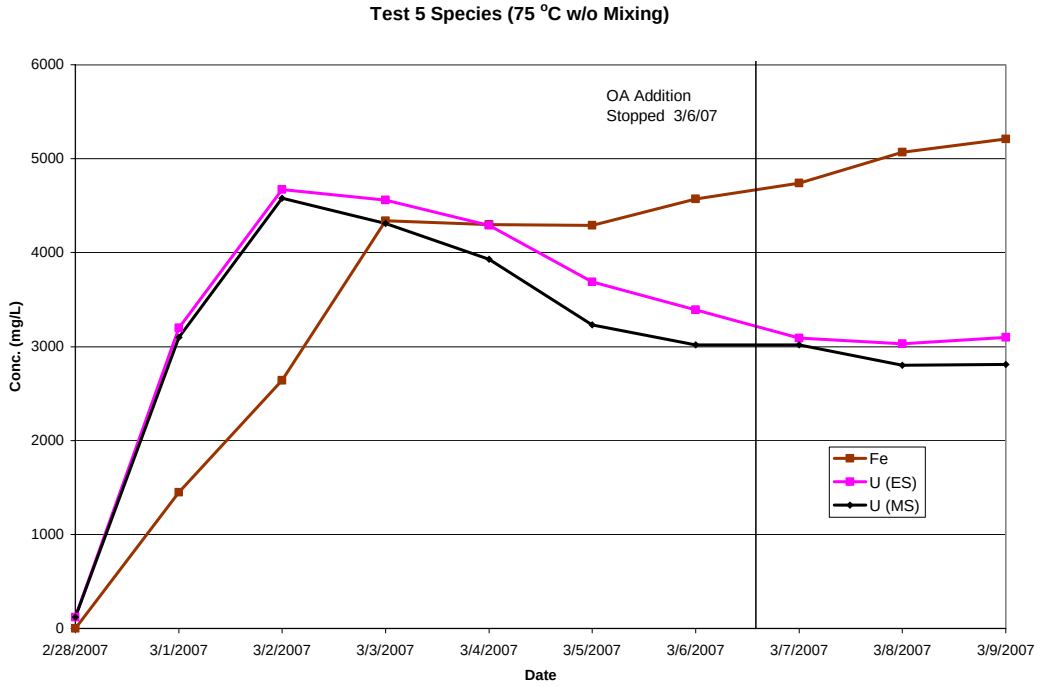

Figure 122. Dissolution kinetics for iron and uranium: 50 °C, unmixed.

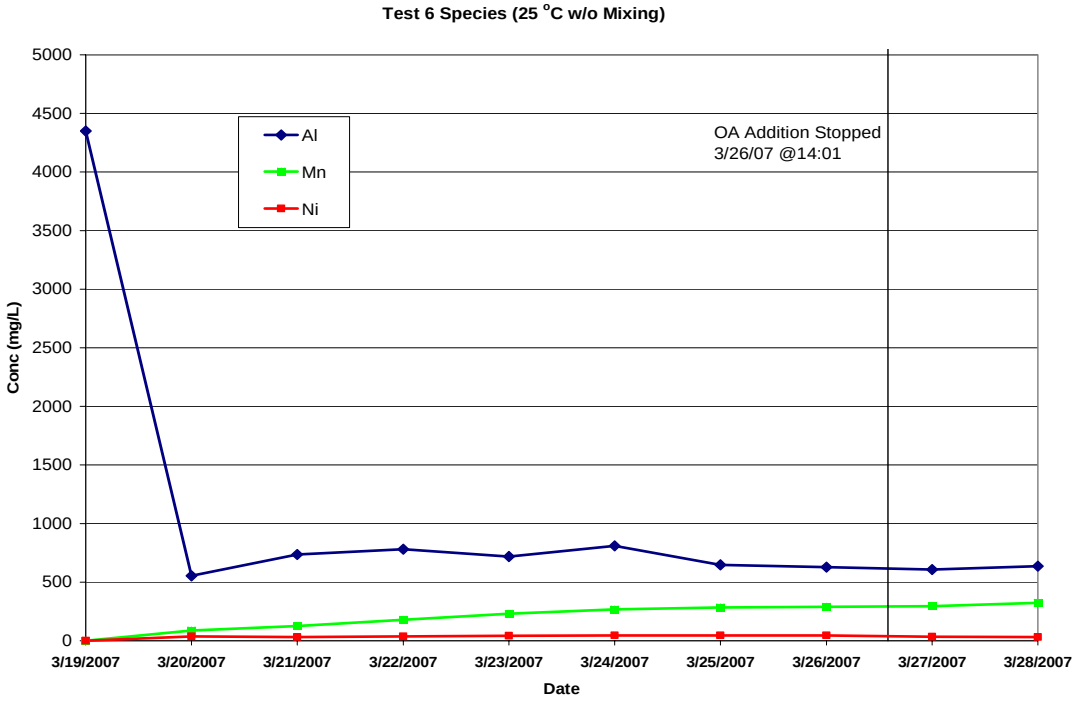

Figure 123. Dissolution kinetics for aluminum, manganese and nickel: 25 °C, unmixed.

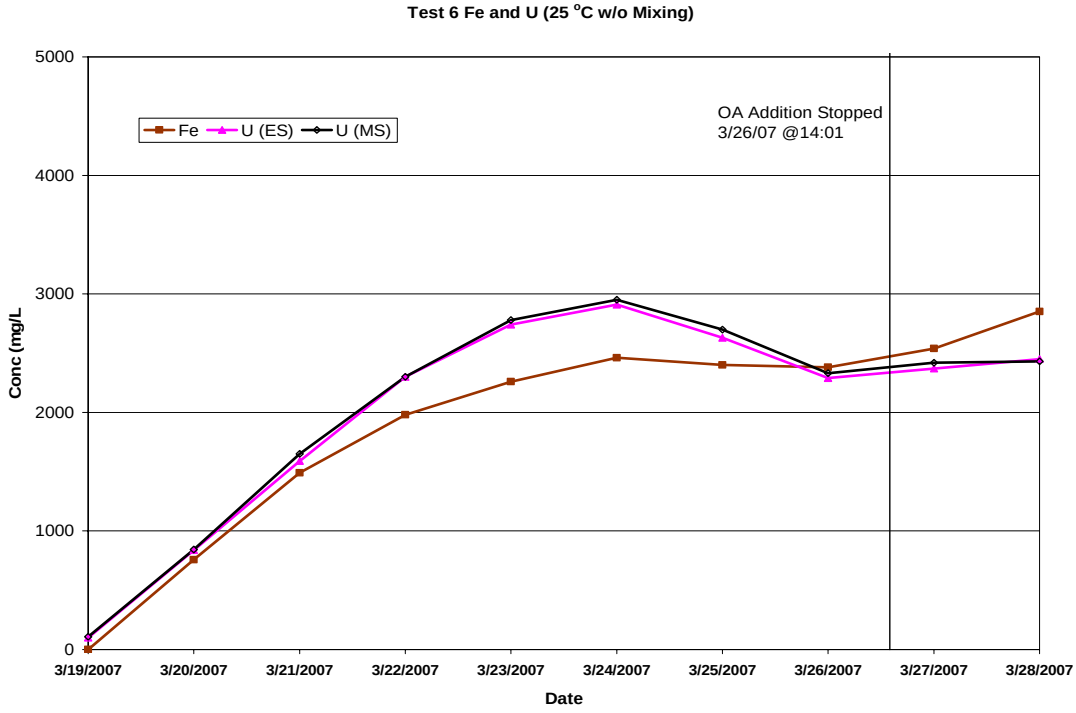

Figure 124. Dissolution kinetics for iron and uranium: 25 °C, unmixed.

REFERENCES

[1] K. Adu-Wusu, M. J. Barnes, N. E. Bibler, J. R. Cantrell, F. F. Fondeur, B. A. Hamm, C. C. Herman, D. T. Hobbs, E. T. Ketusky, M. J. Singleton, M. E. Stallings, W. E. Stevens, and B. J. Wiersma, "Waste Tank Heel Chemical Cleaning Summary," WSRC-TR-2003-00401, September 9, 2003.

[2] W. L. West, "Tank 16 Demonstration - Water Wash and Chemical Cleaning Results," DPSP-80-17-23, December 16, 1980.

[3] M. C. H. Fong, "Oxalic Acid Cleaning of Tank 24H," DSPT-85-782, September 9, 1985.

[4] P. E. Zapp, "Potential for Erosion Corrosion of SRS High Level Waste Tanks (U)," WSRC-TR-93-595, January, 1994

[5] B. J. Wiersma, "Corrosion Mechanisms and Rates for Carbon Steel and Stainless Steel Materials Exposed to Oxalic Acid Solutions," WSRC-TR-2004-00109, March 2004.

[6] N. F. Chapman, "Technical Task Request for Hydrogen Generation in Treatment Tank and Floating Layer in Receipt Tank," HLE-TTR 2005-032, Rev. 1, June 1, 2006.

[7] T. M. Punch, "Tank 5 Sample Analysis," HLE-TTR-2006-009, Rev. 1, December 4, 2006.

[8] K. Adu-Wusu, B. J. Wiersma and S. D. Fink, "Task Technical and Quality Assurance Plan to Investigate Hydrogen Generation and Corrosion in the Treatment Tank and the Potential Formation of a Floating Layer in Neutralization Tank During High Level Waste Tank Heel Chemical Cleaning," WSRC-STI-2006-00035, Rev. 1, November 20, 2006.

[9] M. S. Hay, "Task Technical and Quality Assurance Plan for Characterization of Samples from Tank 5F," WSRC-RP-2006-00717, August 20, 2006.

[10] K. Adu-Wusu, "Tank Heel Chemical Cleaning," WSRC-NB-2006-00143, 2006.

[11] V. Van Brunt, R. Haggard, T. Deal, C. Stork, M. R. Poirier, and S. D. Fink, "Cross-Flow Filtration of Simulated High-Level Waste Sludge (Tank 8F)", WSRC-TR-2001-00195, April 20, 2001.

[12] M. S. Hay, K. P. Crapse, S. D. Fink, and J. M. Pareizs, "Characterization and Actual Waste Tests with Tank 5F Samples," WSRC-STI-2007-00192, April 30, 2007.

[13] B. J. Wiersma and K. H. Subramanian, "Corrosion Testing of Carbon Steel in Acid Cleaning Solutions", WSRC-TR-2002-00427, September, 2002

[14] "Standard Test Method for Conducting Potentiodynamic Polarization Resistance Measurements," ASTM G59-97, Re-approved in 2003.

[15] "Standard Reference Test Method for Making Potentiostatic and Potentiodynamic Anodic Polarization Measurements," ASTM G5-94, Re-approved in 2004.

[16] M. Stern and A. L. Geary, J. Electrochemical Society, Vol. 104, No. 1, pp. 56-63, 1957.

[17] M. G. Fontana and N. D. Greene, Corrosion Engineering, McGraw-Hill, NY, NY, pp. 309ff, 1978.

[18] B. J. Wiersma, "Electrochemical Studies on the Corrosion of Carbon Steel in Oxalic Acid Cleaning Solutions", WSRC-STI-2007-00210, April 30, 2007.

[19] J. R. Scully, "Polarization Resistance Method for Determination of Instantaneous Corrosion Rates," *Corrosion*, Vol. 56, No. 2, February, 2000.

[20] H. D. Smith, R. L. Russell, and G. K. Patello, "Evaluation of Hydrogen Gas Generation from Oxalic Acid Contact with the Carbon Steel of a High Level Waste Storage Tank," In Environmental Issues and Waste Management Technologies in the Ceramic and Nuclear

Industries, Eds. J. C. Marra and G. T. Chandler, Ceramic Transactions, Vol. 93, pp. 221-227, 1999.
[21] SRS "Waste Characterization System (WCS1.5)," August 16, 2006.
[22] "Standard Practice for Laboratory Immersion Corrosion Testing of Metals," ASTM G31-72, Reapproved in 1999.
[23] Atlas of Electrochemical Equilibria in Aqueous Solutions, Ed. by M. Pourbaix, NACE International, Houston TX, p. 317, 1974.
[24] Corrosion: Understanding the Basics, Ed. by J. R. Davis, ASM International, Metals Park, OH, p. 63, 2000.
[25] B. J. Wiersma and H. B. Peacock, "Flammable Gas in Tank 43-H Leak Detection Boxes", WSRC-TR-2002-00142, March 31, 2002.
[26] R. M. Cornell and P. W. Schindler, Clays and Clay Minerals, Vol. 35, No. 5, 347-352, 1987.
[27] B. J. Wiersma and J. I. Mickalonis, "Galvanic Corrosion in Waste Tank Environments", WSRC-TR-2004-00580, December 13, 2004.
[28] D. D. Walker, "Irradiation Apparatus Pressure Build-up Rate Calculation", SRNL-WHM-2004-00011, October 11, 2004.
[29] N. E. Bibler, A. J. Hill, and G. W. Wilds, "Revised Data for Technical Summary Data DPSTD-241-TK-16H Removal of Sludge and Chemical Cleaning of Tank 16H", DPST-78-421, July 7, 1978.
[30] B. J. Wiersma, "Hydrogen Generation During the Corrosion of Carbon Steel in Oxalic Acid", WSRC-TR-2004-00441, August, 2004.